

A MINIATURIZED MULTI-MODALITY IMAGING SYSTEM FOR DIELECTRIC  
MATERIALS EVALUATION

By

Paul Probst

A THESIS

Submitted to  
Michigan State University  
in partial fulfillment of the requirements  
for the degree of

Electrical and Computer Engineering – Master of Science

2021

## **ABSTRACT**

### **A MINIATURIZED MULTI-MODALITY IMAGING SYSTEM FOR DIELECTRIC MATERIALS EVALUATION**

By

Paul Probst

With a rapidly decaying infrastructure, the need for improved and more efficient structural health monitoring and nondestructive evaluation (NDE) only grows with each passing day. Without comprehensive evaluation of structural issues, repairs tend to be temporary and haphazard. The quality of repairs utilizing composite materials cannot be adequately inspected, as there exists a gap within the material coverage in NDE methods caused by the unique anisotropic dielectric characteristics of composite materials. Due to the inherent relationship of dielectric permittivity to electromagnetic theory, and the lack of compact and accurate imaging systems that are not prohibitively expensive for the frequency range (10 KHz to 9 GHz), low frequency capacitive imaging and high frequency microwave imaging have been chosen as the modalities for the system presented in this thesis.

First, the governing theory behind low frequency imaging is detailed, with an emphasis on the capacitive imaging for dielectric characterization of composites. A miniaturized low frequency capacitive imaging system is designed to operate at a frequency range from 10 kHz to 200 MHz with a dynamic range of 113 dB. Additionally, high-Q capacitive resonance probes are designed to be used with the miniaturized imaging system and the results are compared with the preexisting table-top system. Second, general electromagnetic theory is explained and a miniaturized near-field microwave imaging system is designed for dielectric evaluation. The microwave system operates from 1 GHz to 9 GHz and has the ability to work with various probes. Third, both low and high frequency systems are integrated together to provide a wideband multi-modality imaging system. The system demonstrates comparatively accurate results for a fraction of the price of existing systems. The compact and practical nature of this system makes it an optimal tool that can be utilized not only in the lab, but implemented in field conditions as well.

## ACKNOWLEDGMENTS

I would first like to acknowledge my advisor, Dr Yiming Deng for his support, guidance and the level of freedom he provided me throughout my graduate studies. I would also like to thank Dr Prem Chahal and Dr Lalita Udpa from my committee for being available for technical guidance. In particular, Dr Prem Chahal allowed me to use his lab equipment when our lab equipment was out for repairs, and gave invaluable technical input when I was designing the probes. I am grateful for their guidance and support, and appreciate the opportunity to work with all three professors.

I would like to thank my coworkers at the Nondestructive Evaluation Laboratory (NDEL), for their guidance and input, and would especially like to thank Deepak Kumar for his mentorship throughout my graduate studies. I would like to thank all my professors and classmates over the years, for the opportunity to work with them, and for their help in shaping my understanding of numerous topics in electrical engineering. In particular I would like to thank Dr Tim Hogan, Dr Sunil Chakrapani, and Dr Edward Rothwell for their interesting classes, and Dr Chakrapani for allowing me to be a teaching assistant for him for a semester. I would like to thank the supporting staff at the Department of Electrical and Computer Engineering, especially Meagan and Laurene, for their assistance with anything and everything related to administrative requests. I would also like to thank Brian Wright for unquestioningly processing and fabricating every antenna, sensor, and 3D printing design I sent him, no matter how many times. I would also like to thank the funding sponsor for this project, Consolidated Edison, for allowing me the opportunity to work on it. Finally I would like to thank my parents, Pete and Vilija for their unwavering support and love. I would like to thank my grandfather, Viktor and brother Peter for the inspiration to be an engineer and continue my education. I guess my brother Jon paid for a vacation that one time and never lets me hear the end of it so. Thanks bud. Also, my girlfriend Maddy, who provided an untold amount of support and was always there for me at the end of a long day. Lastly I would like to thank anyone and everyone who isn't here to see the end of the journey, particularly Robby, rest in peace.

## TABLE OF CONTENTS

LIST OF TABLES . . . . .	vi
LIST OF FIGURES . . . . .	vii
CHAPTER 1 INTRODUCTION . . . . .	1
1.1 Traditional NDE methods . . . . .	1
1.2 System overview . . . . .	2
1.3 Thesis Objectives . . . . .	2
CHAPTER 2 LOW FREQUENCY CAPACITIVE IMAGING TECHNIQUE . . . . .	4
2.1 Low Frequency Physics Overview . . . . .	4
2.1.1 Capacitive Theory . . . . .	4
2.2 Dielectric Evaluation . . . . .	5
2.2.1 Review of State-of-the-art low frequency methods for dielectric properties measurement . . . . .	7
2.2.1.1 Probes . . . . .	7
2.2.1.2 Systems . . . . .	7
2.2.1.3 Applications . . . . .	8
2.2.1.4 Limitations . . . . .	9
CHAPTER 3 HIGH FREQUENCY MICROWAVE IMAGING TECHNIQUE . . . . .	10
3.1 Microwave Imaging Theory . . . . .	10
3.1.1 Near Field Microwave Theory . . . . .	12
3.1.2 Far Field Analysis . . . . .	16
3.1.3 Scattering Parameters . . . . .	16
3.1.3.1 Scattering Parameters and Power . . . . .	22
3.2 Dielectric Evaluation . . . . .	25
3.2.1 Review of State-of-the-art high frequency methods for dielectric properties measurement . . . . .	26
3.2.1.1 Probes . . . . .	26
3.2.1.2 Systems . . . . .	27
3.2.1.3 Applications . . . . .	28
3.2.1.4 Limitations . . . . .	28
CHAPTER 4 MINIATURIZED CAPACITIVE IMAGING SYSTEM . . . . .	30
4.1 Probe Design and Characterization . . . . .	30
4.2 Importance of High Q . . . . .	35
4.3 System Design and Characterization . . . . .	36
4.4 System Comparison, Lock-in and Mini . . . . .	37
4.5 Conclusion . . . . .	54
CHAPTER 5 MINIATURIZED MICROWAVE IMAGING SYSTEM . . . . .	57

5.1	Probe and System Description . . . . .	57
5.1.1	Wave-guide . . . . .	57
5.1.2	Coaxial probe . . . . .	57
5.2	System Comparison, Table top and Mini . . . . .	57
5.3	Conclusion . . . . .	71
5.4	Importance of System Integration . . . . .	71
5.4.1	Edge detection vs penetration . . . . .	72
5.5	Low and High frequency system comparisons . . . . .	72
CHAPTER 6 CONCLUSIONS AND FUTURE WORK . . . . .		73
6.1	Importance of System Integration . . . . .	73
6.1.1	Edge detection vs penetration . . . . .	73
6.1.2	Low and High frequency system comparisons . . . . .	74
6.2	Conclusions . . . . .	74
6.3	Future work . . . . .	75
APPENDICES . . . . .		76
APPENDIX A	DIELECTRIC LENS . . . . .	77
APPENDIX B	MICROWAVE NETWORK ANALYSIS . . . . .	81
BIBLIOGRAPHY . . . . .		95

## LIST OF TABLES

Table 2.1: Dielectric properties of various materials [25] [26] . . . . .	6
Table 2.2: Common low frequency system relative comparison . . . . .	9
Table 3.1: Common High frequency system comparison . . . . .	29
Table 4.1: Capacitive probe dimensions . . . . .	31
Table 4.2: Frequency Shift of probes, at varying permittivities . . . . .	35
Table 4.3: Plate 1 size and scan dimension table . . . . .	42
Table 4.4: Plate 2 size, scan, and defect dimension table . . . . .	44
Table 4.5: Plate 4 size, scan, and defect dimension table . . . . .	46
Table 4.6: Plate 5 size, scan, and defect dimension table . . . . .	48
Table 4.7: Plate 6 size, scan, and defect dimension table . . . . .	50
Table 4.8: Plate 7 size, scan, and defect dimension table . . . . .	52
Table B.1: Split ring resonator dimension table . . . . .	94

## LIST OF FIGURES

Figure 2.1: Capacitive probe imaging setup used for imaging within this thesis . . . . .	6
Figure 4.1: LC tank resonance probe design . . . . .	30
Figure 4.2: Low Frequency Probes designed for the system . . . . .	31
Figure 4.3: Measured reflection coefficient for Probe 2 (1 mm Plate separation) . . . . .	32
Figure 4.4: Measured reflection coefficient for Probe 4 (1.5 mm Plate separation) . . . . .	32
Figure 4.5: Measured reflection coefficient for Probe 6 (2 mm Plate separation) . . . . .	33
Figure 4.6: Measured reflection coefficient for Probe 1 (1 mm Plate separation) . . . . .	33
Figure 4.7: Measured reflection coefficient for Probe 3 (1.5 mm Plate separation) . . . . .	34
Figure 4.8: Measured reflection coefficient for Probe 5 (2 mm Plate separation) . . . . .	34
Figure 4.9: Frequency shift comparison between probes 1 through 6 . . . . .	35
Figure 4.10: Block Diagram of Low Frequency system . . . . .	37
Figure 4.11: Aluminum calibration sample results comparison (a) table top system, (b) mini system . . . . .	39
Figure 4.13: GFRP impact damage sample results comparison (a) table top system, (b) mini system . . . . .	40
Figure 4.15: PE sample subsurface defect results comparison (a) table top system, (b) mini system . . . . .	41
Figure 4.17: Plate 1 Defect Map . . . . .	42
Figure 4.18: Plate 1 results comparison (a) table top system, (b) mini system . . . . .	43
Figure 4.20: Plate 2 Defect Map . . . . .	44
Figure 4.21: Plate 2 results comparison (a) table top system, (b) mini system . . . . .	45
Figure 4.23: Plate 4 Defect Map . . . . .	46

Figure 4.24: Plate 4 results comparison (a) table top system, (b) mini system . . . . .	47
Figure 4.26: Plate 5 Defect Map . . . . .	48
Figure 4.27: Plate 5 results comparison (a) table top system, (b) mini system . . . . .	49
Figure 4.29: Plate 6 Defect Map . . . . .	50
Figure 4.30: Plate 6 results comparison (a) table top system, (b) mini system . . . . .	51
Figure 4.32: Plate 7 Defect Map . . . . .	52
Figure 4.33: Plate 7 results comparison (a) table top system, (b) mini system . . . . .	53
Figure 4.35: PE Sample Probe setup . . . . .	54
Figure 4.36: Probe equivalent circuit . . . . .	55
Figure 5.1: Aluminum Calibration sample, table top system (Coax) . . . . .	59
Figure 5.2: Aluminum Calibration sample, mini system scan (Coax) . . . . .	60
Figure 5.3: Aluminum Calibration sample, table top system (Wave-guide) . . . . .	61
Figure 5.4: Aluminum Calibration sample, first square, mini system (Coax) . . . . .	62
Figure 5.5: Aluminum Calibration sample, first square, mini system (Wave-guide) . . . . .	63
Figure 5.6: Polyethylene, table top system (Wave-guide) . . . . .	64
Figure 5.7: CFRP Plate 1, Wave-guide, mini system . . . . .	65
Figure 5.8: CFRP Plate 2, Wave-guide, mini system . . . . .	66
Figure 5.9: CFRP Plate 4, Wave-guide, mini system . . . . .	67
Figure 5.10: CFRP Plate 5, Wave-guide, mini system . . . . .	68
Figure 5.11: CFRP Plate 6, Wave-guide, mini system . . . . .	69
Figure 5.12: CFRP Plate 7, Wave-guide, mini system . . . . .	70
Figure A.1: Focusing of RF waves radiated from patch antenna using dielectric lens . . . . .	78
Figure A.2: Designed and fabricated lens with the dimensions . . . . .	78

Figure A.3: Simulated and Measured gain of the patch antenna at 5.3 GHz without lens . . . 79

Figure A.4: Simulated and Measured gain of the patch antenna at 5.3 GHz with lens . . . . 80

Figure B.1: Simulated split ring resonator with dimension parameters . . . . . 93

Figure B.2: Simulated split ring resonator response . . . . . 94

# CHAPTER 1

## INTRODUCTION

### 1.1 Traditional NDE methods

The market currently contains standalone systems for eddy current probes, but as of the writing of this, there are no off the shelf systems that explicitly offer capacitive imaging capability, nor are there any systems for microwave imaging. Multi-modality systems exist, but none of them incorporate both microwave and capacitive imaging systems. The systems that exist in the market are also prohibitively expensive, with the price of a standalone eddy current system reaching over fifty-thousand USD, whereas the system that will be presented in this paper was designed, built, and implemented for a fraction of the price. Traditional, off the shelf NDE methods for composite materials include but are not limited to ultrasound, [1,2] X-ray/CT, [3] and eddy-current systems. [4] Within research though, high frequency microwave and low frequency capacitive modalities have been tested numerous times [5–8] and proven to characterize defects as reliably as the traditional methods, with the added caveat of being much cheaper to produce and upkeep. Microwave systems utilizing RF waves have been used to image and monitor infrastructure like oil and gas lines [9], and specifically used for composite scanning [10] as well as been used experimentally to excite thermoacoustic waves to detect defects acoustically [11]. Higher frequency scanning of plastics alone have been proven to reliably image defects utilizing RFID tags. [12] Microwave scans of composite CF-metal samples have shown to accurately image steel corrosion. [13] Systems similar to this wherein NDE has been performed utilizing portable systems have been shown to reliably image carbon fiber samples as well, [14] besides the use of more traditional research systems used for imaging carbon-fiber shown to reliably image defects utilizing ion beams [15] and using magnetic induction tomography [16]. CT scans have been utilized for composite CF-metal defect detection. [17] Other reliable results have been obtained for electromagnetically imaging glass-fiber reinforced composites [18] and through ultrasonic scanning via nonlinear harmonic

generation [19]; far-field microwave scanning, which isn't strictly utilized but will be briefly discussed later, has proven reliable for imaging GFRP-composite materials. [20] Outside of NDE, microwave analysis has been reliably utilized to perform quality control on packaged food [21] with system improvements occurring regularly [22] [23] or to perform quality control on increased or decreased acidity when the situation calls for it. [24]

## **1.2 System overview**

The system presented in this thesis was built for specific composite scanning and will be utilized in the field, though it is not limited to this application specifically, and can be improved further as will be detailed below. Typical scanning systems will include hardware and software elements, but due to the possibility of untrained personnel utilizing the system in the field, the hardware side has been emphasized for this system so that all the debugging can be done before any field operations take place. The software created for this system is minimal, and mostly serves the purpose of visualization of the data collected. The system has been designed so that results can be acquired quickly and economically.

## **1.3 Thesis Objectives**

The scope of this thesis is to demonstrate a compact, standalone, economical multi-modality NDE system, while also establishing an explanation and justification of the utilized methods. The thesis organization is as follows: Chapter 2 gives an overview of low frequency imaging theory, and details the design process and compares cost, sensitivity, and size of commonly used low frequency systems. In chapter 3, a detailed overview of microwave theory is presented within the scope of NDE with the majority of the details serving as explanation for how the DAQ method for microwave was utilized within the system, how the probes work physically, why certain theories are so important, and goes on to perform a similar analysis of relative size, cost, and sensitivity of commonly used microwave imaging systems. Chapter 4 details the low frequency probes designed for the system, and shows a direct comparison of the results obtained from a table top system

utilizing a lock-in amplifier to the results acquired from the designed low frequency mini system. In chapter 5, the probes used with the minituarized microwave system are briefly discussed, along with a comparison of results obtained from the microwave system that validate results acquired from the capacitive imaging system. In chapter 6, the capability of integration of both systems for the purpose of a multi modality imaging system is discussed, and the strengths and weaknesses of both imaging systems is covered. The ultimate conclusion of the thesis is also presented, and a brief road map for improvements to the system moving forward is proposed. In appendix A, work performed fabricating a dielectric lens for implementation within the same frequency band as the high frequency system presented in this thesis is discussed, though that work was not explicitly done for this thesis. In appendix B, a more detailed background of microwave network analysis is covered, and a simulated split ring resonator design, its dimensions, and response, is shown.

## CHAPTER 2

### LOW FREQUENCY CAPACITIVE IMAGING TECHNIQUE

#### 2.1 Low Frequency Physics Overview

##### 2.1.1 Capacitive Theory

Shortwave capacitive probes were chosen due to their lower frequency allowing deeper penetration of the carbon fiber layers. This allows for defects present deeper than the microwave penetration depth to be identified. The design of shortwave capacitive probes follows the same logic as microwave probes, as the prevailing design theory is relatively similar: the capacitive probe detects a change in dielectric coefficient that allows for contrast images to be developed, leading to defect identification. Many of the equations, however can be simplified due to lower frequencies involved. Shortwave probes have been proven to reliably image defects in composites due to the innate ability to sense changes in dielectric permittivity with one of the most frequently utilized probes being a parallel plate capacitor in some degree, where the governing equations of these probes is defined as

$$Z_{cap} = \frac{1}{j\omega C} \quad (2.1)$$

where  $C$ , the capacitance, is defined as

$$C = \frac{\epsilon A}{d} \quad (2.2)$$

Where  $A$  is the area of the probe, and  $d$  is the distance between the excitation and ground. For the probe utilized in the system an LC tank architecture is used due to the ability for much higher Q factor, and thus, a much more sensitive probe, or much larger change to the resultant impedance imposed from a dielectric permittivity change. The impedance is defined as

$$Z = \sqrt{R^2 + (X_L - X_C)^2} \quad (2.3)$$

while the Q factor for an LC tank is defined as

$$Q = \frac{1}{R} \sqrt{\frac{L}{C}} \quad (2.4)$$

and can be simplified to

$$Q = R\sqrt{\frac{L^2}{LC}} \quad (2.5)$$

and even further simplified to

$$Q = \frac{\omega_0 L}{R} \quad (2.6)$$

where

$$\omega_0 = \frac{1}{\sqrt{LC}} \quad (2.7)$$

Due to this, the resonant frequency of the probe can be inferred as

$$f_0 = \frac{1}{2\pi\sqrt{LC}} \quad (2.8)$$

The probe is read in reflection mode, as at the resonant frequency, when the  $Q$  is highest, the reflective coefficient of the probe is near maximum, allowing for total reflection. The introduction of materials will shift the resonant frequency much more sharply based on the  $Q$  value, and will have specific responses for common defect dielectric values, such as air. The sharp change in the resultant values of the reflection coefficient that arise from the introduction of defects in contrast to the consistent values acquired when the uniform material is scanned allow for defects to be viewed when the data is input to an imaging software like MATLAB.

## 2.2 Dielectric Evaluation

The resonance frequency of a capacitive probe is inherently related to the capacitance and inductance values, as seen in equation 2.8, with the equation for capacitance shown in equation 2.2. By using a fixed inductance value and a capacitor utilizing parallel plates or concentric circles that contain a fixed area, and a fixed distance between the two, the only variable in the equation becomes  $\epsilon$ , the relative permittivity. By printing a capacitive plate onto a board with a known dielectric constant, the only way to induce a change in relative permittivity is by interacting with the capacitive fields by bringing a sample within the field range. This interaction allows for imaging and characterization of samples with defects in them, due to the nature of defects frequently having specific relative permittivities associated with them. A crudely drawn example of this can be seen

in the figure below. Dielectric defects in samples can be easily scanned when reading a resonance

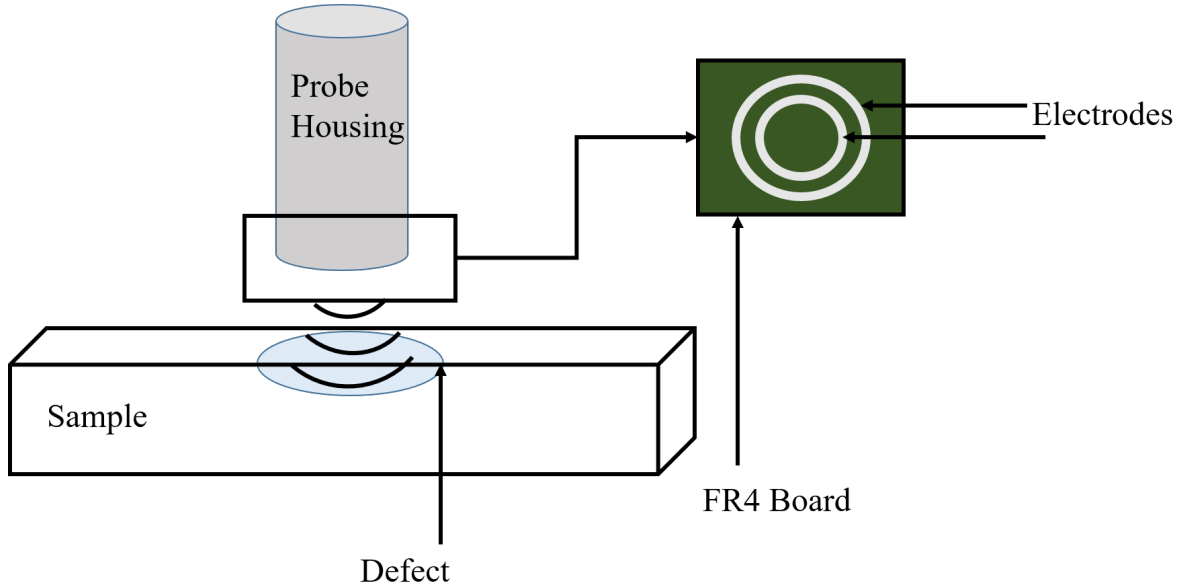


Figure 2.1: Capacitive probe imaging setup used for imaging within this thesis

probe in reflection mode due to the frequency shift that will be induced by a sudden change in permittivity. The reflected power and phase can be back-calculated from values read out in the form of in phase (I) and quadrature phase (Q). The approximate location, and size of the defect can be inferred and a sample can be characterized. Various dielectric characteristics of defects present in samples scanned are shown in the table below, with results shown later in the paper.

Material	$\epsilon_r$
Air	$\approx 1.0006$
Water	80
Sand	3-5
Clay (soil)	5-40
Humid Soil	30
Polyethylene	2.2-2.4
GFRP	$\approx 2-4$
Mold (fungus)	1.15-1.6 [27]
Resins	2.4-4.1

Table 2.1: Dielectric properties of various materials [25] [26]

## **2.2.1 Review of State-of-the-art low frequency methods for dielectric properties measurement**

### **2.2.1.1 Probes**

The most common capacitive probe is any variation of a capacitive plate where the signal is fed into one plate, with the other plate being grounded for reflection mode, or with a signal being fed into one plate and read on the other plate in transmission mode. The probe can be viewed as a 1 or 2 port network depending on the read method utilized. Probes that do not utilize an LC resonance architecture have a relatively low Q value, leading to a loss in sensitivity. The probe itself is important as plates with wider separation will have greater penetration depth, though they will be less sensitive to dielectric change, ie the resonance frequency will not shift as much. Probes with smaller separation between the plates will be extremely sensitive, or the resonance frequency will shift by much more, but the field penetration depth and overall distance of field output will be much lesser.

### **2.2.1.2 Systems**

Current common methods of capacitive imaging include the use of a lock-in amplifier, a direct read-out of change in capacitance in farads using a microcontroller and voltage excitation, using an impedance analyzer to detect a change in capacitance. Ectane is an off the shelf product capable of performing capacitive scans do to its relatively low frequency excitation. These methods can provide accurate data, and a SR844 lock-in amplifier was used for calibration and as a benchmark when debugging and prototyping the created mini system, but a lock-in amplifier is a bulky piece of equipment, and can cost several thousand dollars<sup>1</sup>; moreover a separate signal generator to excite the probe is required, adding another few thousand to the total price tag. Direct readout utilizing a micro controller is very compact, and is very cheap, but the level of accuracy is low due to the inability for this method to read resonance probes efficiently. Impedance analyzers are arguably as accurate as lock-in amplifiers, though again, impedance analyzers are relatively bulky pieces of

---

<sup>1</sup>SR844, thinksrs.com

equipment, and can run tens of thousands of dollars in price<sup>2</sup>. From this there seems to be a trade off between accuracy, size, and price. Ectane is relatively compact, as far as standalone systems go, though it is roughly the same volume as the lock-in amplifier and signal generator, and can produce accurate scans. This option seems optimal until price is taken into account, as Ectane's sticker price is over eight thousand dollars a month to rent<sup>3</sup>. To buy used, the system can cost thirty thousand dollars <sup>4</sup> while the price for a new system can easily run over fifty thousand dollars <sup>5</sup>. So is a compact, accurate, and relatively cheap system an impossibility? Not at all. The low frequency system presented in this paper performs at least as well as a lock-in amplifier, was prototyped and built for less than a thousand dollars, and can take up a volume of 252 inches<sup>3</sup>.

### **2.2.1.3 Applications**

Capacitive imaging systems can be utilized to scan dielectric materials for defects, and in a modern world with more complex materials, more and more infrastructure components and industries in general are using composite materials that have dielectric properties. Composite plastics currently are widely used in pipelines, and in industries including aerospace, defense, and energy. The ability for complex materials to fail catastrophically means there needs to be some sort of quality control and capacitive imaging is broadly used for this purpose. [8, 28] An additional application specific problem unrelated to price, size, but tangentially related to sensitivity, is the ability for a system to be used in field conditions, and not solely research lab conditions. The lock-in amplifier, signal generator, and impedance analyzer are too delicate and too bulky for field conditions, and are not designed for such ventures. The direct read system can be adapted for field use, but it needs heavy modification to achieve this capability. The Ectane system is specifically built for field use, but again, at the price of  $\approx$ fifty times the price of the designed mini system.

---

<sup>2</sup>Keysight E4990A

<sup>3</sup>kwipped.com (Ectane 2)

<sup>4</sup>eBay

<sup>5</sup>bullseye calibration

#### 2.2.1.4 Limitations

A comparison of the aforementioned systems and the designed mini system in regards to sensitivity, price, overall size, and field use capability summarizing the above section can be seen in the table below.

System	Relative Sensitivity	Price	Relative Size	Field use?
Lock-in Amplifier	High	\$10,000+	Bulky	X
Impedance Analyzer	Medium-High	\$25,000+	Bulky	X
Direct read	Low	\$30+	Very Compact	✓
Ectane	High	\$50,000+	Compact	✓
Mini system	High	≈\$1,000	Very Compact	✓

Table 2.2: Common low frequency system relative comparison

## CHAPTER 3

### HIGH FREQUENCY MICROWAVE IMAGING TECHNIQUE

The most important general form equations utilized within the following sections are modifications and variations of the generalized three dimensional wave equation, which takes the form

$$\frac{1}{v^2} \frac{\partial^2 \vec{q}}{\partial t^2} = \frac{\partial^2 \vec{q}}{\partial z^2} + \frac{\partial^2 \vec{q}}{\partial y^2} + \frac{\partial^2 \vec{q}}{\partial x^2} \quad (3.1)$$

where  $q(\vec{r}, t)$  is the displacement and is a function of the medium at a point  $\vec{r} = (x, y, z)$  at a time  $t$ .

A more useful form of the equation is utilized in the form,

$$\left(\nabla^2 + \frac{\omega^2}{c^2}\right)\Psi(\vec{r}, \omega) = 0 \quad (3.2)$$

which incorporates the Fourier-transform of the wave equation

$$\Psi(\vec{r}, t) = \int_{-\infty}^{\infty} \Psi(\vec{r}, \omega) e^{-j\omega t} d\omega \quad (3.3)$$

for evaluation of the wave equation in the frequency domain. Expansion of the above equations will be touched on in the proceeding sections.

### 3.1 Microwave Imaging Theory

Low-power high Q factor microwave probes are commonly chosen as an imaging method due to their ability to detect and characterize defects within dielectric materials. The probes needed to be designed using the following characteristic equations due to their governing of the response of the probes. When powered, the probes radiate high frequency electromagnetic waves that penetrate the carbon fiber layers to, at most, the steel. The waves are reflected back to the probe, and the defects are characterized utilizing changes in the reflection coefficient. The reflection coefficient from a sample would remain consistent with a consistent height of probe, frequency, and power, so steps were made in the system design to ensure that both frequency and power delivered remained as stable as possible. Without defects, the reflection coefficient would return one value, while with defects, the value would be different enough that a contrast image could be obtained using the

magnitude and phase of the reflection coefficient. Depending on the nature of the defect and its size, certain characterizations can be made about the signal response, though if defect types have a cross over in dielectric constant, this characterization cannot be guaranteed to be entirely accurate, E.g. if an epoxy delamination and a soil contamination dielectric coefficient range from  $\epsilon = 3 - 15$  and  $\epsilon = 8 - 20$  then a measured response indicating a dielectric coefficient of  $\epsilon = 8 - 12$  would not be able to differentiate between the two, unless other information is reliably known, if either has a consistent size. The returned results would indicate that a defect was present though, and repairs would have to be made regardless. The design of microwave probes for this project took place utilizing ANSYS HFSS, as well as MATLAB, to solve the following equations. The most important relations of electromagnetic theory are as follows: The electromagnetic wave equation describing the electric and magnetic fields is defined as

$$(v_{ph}^2 \nabla^2 - \frac{\partial^2}{\partial t^2}) \vec{E} = 0 \quad (3.4)$$

for the electric field and

$$(v_{ph}^2 \nabla^2 - \frac{\partial^2}{\partial t^2}) \vec{B} = 0 \quad (3.5)$$

for the magnetic field, where

$$v_{ph} = \frac{1}{\sqrt{\mu\epsilon}} \quad (3.6)$$

is the speed of light. Following this, the most important relations, and arguably some of the most important mathematical equations derived in all of human history, is the collection of equations known as Maxwell's equations, presented here in differential equation form, and take the forms

$$\nabla \cdot \vec{D} = \rho \quad (3.7a)$$

$$\nabla \cdot \vec{B} = 0 \quad (3.7b)$$

$$\nabla \times \vec{E} = \frac{-\partial \vec{B}}{\partial t} \quad (3.7c)$$

$$\nabla \times \vec{H} = \vec{J} + \frac{\partial \vec{D}}{\partial t} \quad (3.7d)$$

where 3.7a is Gauss's law, relating the electric field to charge and dielectric constant and fundamentally proves the existence of electric dipoles. Conversely, 3.7b is Gauss's law for magnetism which

shows the divergence of a magnetic field is zero, or that a magnetic monopole does not exist. 3.7c is the Maxwell-Faraday equation or Faraday's law of induction, and predicts how a magnetic field will interact with an electric circuit to produce electromotive force. This equation was touched on earlier for an in depth explanation of eddy current system performance. Finally, 3.7d is known as Ampère's circuital law, which relates the electric field and induced current charge on a closed loop to the intrinsic magnetic field of the circuit.

### 3.1.1 Near Field Microwave Theory

There are different regions within microwave fields dependent on distance, the near field, and the far field. In far field analysis, the waves can be treated like planar waves, and the power dissipates extremely rapidly after exiting the near field region. The waves within the near field act very differently, and the relationship between the electric and magnetic fields is very complicated, as will be explained shortly. The electromagnetic fields are much more powerful in the near field, and allows for imaging due to the high intensity of the fields. The boundary between near and far field can be found using the Fraunhofer distance equation

$$d = \frac{2D^2}{\lambda} \quad (3.8)$$

where  $D$  is the largest dimension of the device that is radiating (eg. a loop antenna's diameter) and  $\lambda$  is the wavelength of the signal. The near field is split into the non-radiative or reactive near field, the nearest part of the near field, and the radiative near field or Fresnel region, the farthest part of the near field. The reactive near field covers up to the distance  $\frac{\lambda}{2\pi}$  while the Fresnel region covers between this distance and the Fraunhofer distance. The reactive region can also be characterized by any location less than or equal to  $0.62\sqrt{\frac{D^3}{\lambda}}$  while the Fresnel region covers between this distance and  $d$  from the above equation. Near field scanning modalities utilize oscillating fields that do not allow for the propagation of EM waves by scattering them due to the geometry of the probe. [29] The oscillation of the fields allows for a net energy flow of zero, due to the Poynting vector averaged over an oscillation equaling zero. [29] These fields are referred to as evanescent and create waves

with imaginary wavenumbers that store reactive energy. This reactive energy can be either electric, or magnetic, or both. A sample interacting with the near field of the probe will change the energy, altering the EM response of the probe. The creation of an evanescent field in a sample relies on the size of the probe tip  $D$  and must be small enough to satisfy  $|k_d|D \ll 1$ , where  $k_d$  is the complex wave number of the device under test given by:

$$k_d = \omega \sqrt{\epsilon_0 \epsilon_d \mu_0 \mu_d} \quad (3.9)$$

The evanescent fields from the probe interact with the DUT and allow for characterization through the change in EM waves. The size of the field(s) is roughly equivalent to the probe size  $D$ , which dictates the resolution of the scan more so than any properties of the DUT. This type of imaging is called NF microwave microscopy and is a very exciting topic in the imaging world due to the use of microwave frequencies to image samples with resolutions of orders of magnitude smaller than a wavelength. The energy contained in the reactive field goes through a type of feedback loop and can load the system 'more' than it already is, allowing for the energy that is 'returning' from the DUT/scanned sample be isolated from the input signal, and evidently this allows for accurate imaging to take place due to perturbations in the signal signifying defects/characterizing features in the sample. To effectively create a NF microwave probe, one must be able to calculate the impedance and reflection coefficients. And to make it worthwhile, we would want to do it using transmission lines because lumped components are extremely passé. The impedance of a probe tip can be found using

$$Z_p = R_p + jX_p \quad (3.10)$$

where a NF tip reactance can be found using

$$X_p = \frac{4\omega}{|I_i|^2} \int_V (w_m - w_e) d^3x \quad (3.11)$$

where  $w_m$  is magnetic energy density,

$$w_m = \frac{BH^*}{4} \quad (3.12)$$

and  $w_e$  is electric energy density,

$$w_e = \frac{ED^*}{4} \quad (3.13)$$

and  $I_i$  is the harmonic input current at the tip terminal. [30]  $R_p$  can be found using

$$R_p = \frac{\omega}{|I_i|^2} \int V \left( \frac{\sigma}{\omega} |E|^2 + \epsilon_0 \epsilon'' |E|^2 + \mu_0 \mu'' |H|^2 \right) d^3x \quad (3.14)$$

The impedance of an electric tip can be expressed in relation to the coupling capacitance between the probe tip and sample where

$$\frac{1}{C_c} = \frac{1}{C_{c1}} + \frac{1}{C_{c2}} \quad (3.15)$$

and  $C_{str}$  represents the stray capacitance from the probe tip, as

$$\frac{1}{Z_{tE}} = \left( \frac{1}{j\omega C_c} + Z_s \right)^{-1} + j\omega C_{str} \quad (3.16)$$

where  $Z_s$  is the NF sample impedance. [30] The impedance of magnetic tip, when  $|k_d|D \gg 1$  can be found using

$$Z_{tM} = j\omega L_0 + \frac{\omega^2 M^2}{Z_s + j\omega L_1} \quad (3.17)$$

where  $L_0$  is the loop self inductance,  $L_1$  is the sample inductance, and  $M$  is the probe tip-sample inductance. [30] The impedance of an electric tip should satisfy  $|Z_{tE}| \gg Z_0$  while a magnetic tip should satisfy  $|Z_{tM}| \ll Z_0$  thus the complex reflection coefficient from the tips can be found using

$$\Gamma_E = \exp -\frac{2Z_0 R_{pE}}{R_{pE}^2 + X_{pE}^2} \exp j \frac{2Z_0 X_{pE}}{R_{pE}^2 + X_{pE}^2} \quad (3.18)$$

where  $\Gamma_E$  can also be expressed as

$$\Gamma_E = |\Gamma_E| \exp j\theta_E = \frac{Z_{pE} - Z_0}{Z_{pE} + Z_0} \quad (3.19)$$

and

$$\Gamma_M = |\Gamma_M| \exp j\theta_M = \frac{Z_{pM} - Z_0}{Z_{pM} + Z_0} \quad (3.20)$$

can also be expressed as

$$\Gamma_M = \exp -\frac{2R_{pM}}{Z_0} \exp -j \frac{2X_{pM}}{Z_0} \quad (3.21)$$

These equations, however, deal primarily with phase, and when the phase measurement/calculation is not accurate enough resonant frequency and Q factor for the probe tip would also need to be

calculated. The equations for resonant frequency and (un-loaded) Q factor of an electric field probe are as follows

$$F = \frac{\pi n}{2\pi L \sqrt{\epsilon_0 \mu_0 \epsilon_{eff}}} \left[ 1 + \frac{Z_0 X_{pE}}{\pi n (R_{pE}^2 + X_{pE}^2)} \right] \quad (3.22)$$

$$Q = \frac{\omega'}{2\omega''} = \frac{(\pi n + \frac{Z_0 X_{pE}}{R_{pE}^2 + X_{pE}^2})}{2h'' L + \frac{2Z_0 R_{pE}}{R_{pE}^2 + X_{pE}^2}} \quad (3.23)$$

where L is the length of the probe and

$$h = h' - jh'' = \omega \sqrt{(\epsilon_0 \epsilon_{eff} \mu_0)} - jh'' \quad (3.24)$$

is the complex propagation constant of the transmission line. [30] If instead of a probe, the design was to be a cavity (eg. a waveguide) there is cavity perturbation theory which shows that for a low loss dielectric film of unknown (complex) permittivity the frequency associated can be found using

$$\frac{\Delta F}{F} \cong -(\epsilon'_{film} - 1) \frac{\epsilon_0}{4W} \int_{V_s} E_1 E_2 dV \quad (3.25)$$

along with associated Q factor

$$\Delta \frac{1}{Q} = -\tan \delta \frac{2\epsilon'_{film}}{\epsilon'_{film} - 1} \frac{\Delta F}{F} \quad (3.26)$$

with the desired solutions being the electric fields  $E_1$  and  $E_2$ . [30] Near field power applications can be utilized using an equation for power received,  $P_{Rx}$  vs power transmitted,  $P_{Tx}$  for antennas that are either both magnetic or electric, or mis-matched which are respectively as follows

$$\frac{P_{Rx}}{P_{Tx}} = \frac{G_{Tx} G_{Rx}}{4} \left( \frac{1}{(kr)^2} \frac{1}{(kr)^4} \frac{1}{(kr)^6} \right) \quad (3.27)$$

$$\frac{P_{Rx}}{P_{Tx}} = \frac{G_{Tx} G_{Rx}}{4} \left( \frac{1}{(kr)^2} \frac{1}{(kr)^4} \right) \quad (3.28)$$

with  $G_{Tx}$  and  $G_{Rx}$  representing the gain of the transmitting and receiving antennas respectively, while  $r$  is the range between the antennas and  $k = \frac{2\pi}{\lambda}$ . [31]

### 3.1.2 Far Field Analysis

Analysis of microwave networks in the far field differs from near-field analysis in that many of the equations become simplified. The main point of interest for far field analysis is arguably the Friis transmission equation,

$$P_R = P_T + G_T + G_R + 20\log_{10}\left(\frac{\lambda}{4\pi d}\right) \quad (3.29)$$

where  $P_R$  is the power received,  $P_T$  is the power transmitted,  $G_T$  is the gain of the transmitting antenna,  $G_R$  is the gain of the receiving antenna, all in dBm;  $\lambda$  is the wavelength in meters, and  $d$  is the distance between the antennas in meters. In terms of far field scanning of samples, the sample would be viewed as the receiving antenna and the gain would be minimum, or very low, dependent on composition of the sample. The other important relation is

$$\lambda = \frac{c}{f\sqrt{\epsilon_r}}$$

where  $c$  is the speed of light in  $\frac{m}{s}$ ,  $f$  is the frequency in Hz, and  $\epsilon_r$  is the relative permittivity. Since the near entirety of the sample scans were performed within the near field, this section will remain brief.

### 3.1.3 Scattering Parameters

When designing a microwave system, it must be treated like a network to adequately simulate the possible results. When analyzing the network, the important components to monitor include the propagation of the system, or the power of the electromagnetic fields that will be interacting with the samples being imaged. The propagation is also important for knowing the response of the probe by knowing the locations of the near and far field. Another important component is the transmission lines involved in the system. Transmission lines dictate the intrinsic impedance of the system at a specific frequency and the effectiveness of the designed probe and system responses. Transmission lines are a very fundamental part of microwave network analysis and electromagnetic theory as a whole, and are further explored in B.1.1. One of the most important, if not the most important, components of microwave network analysis and system design are the scattering parameters. These

parameters are intrinsically linked with the frequency of the system. They give information about the reflection and transmission coefficients, and the overall responses of the reflection and transmission of the system as a whole. The resultant reflection and transmission coefficients in a well designed system are inversely related: when transmission is maximum, reflection is minimum, and vice versa. This is very important for dictating how data will be acquired, and which read mode to use, either reflection on one port, or reflection on two ports. With single port reflection the probe injects electromagnetic waves into the sample and "listens" for the reflected wave. The time difference in sent and received signals can dictate the depth of a defect, and the power reflected will indicate the composition of the defect. The scattering parameter response of the both the microwave and capacitive probes were used to tune the operating frequency for both. A brief explanation of scattering parameters is included below: From [32] the scattering matrix is defined as:

$$\begin{bmatrix} V_1^- \\ V_2^- \\ \vdots \\ V_N^- \end{bmatrix} = \begin{bmatrix} S_{11} & S_{12} & \dots & S_{1N} \\ S_{21} & & & \vdots \\ \vdots & & \ddots & \\ S_{N1} & \dots & & S_{NN} \end{bmatrix} \begin{bmatrix} V_1^+ \\ V_2^+ \\ \vdots \\ V_N^+ \end{bmatrix}$$

Where  $V_N^+$  is defined as the forward voltage, and  $V_N^-$  is the reverse voltage. The  $[S]$  matrix is comprised of scattering parameters, and is defined in relation to the incident and reflected voltage waves:

$$[V^-] = [S][V^+] \quad (3.30)$$

where a specific matrix element is defined as

$$S_{ij} = \left. \frac{V_i^-}{V_j^+} \right|_{V_k^+ = 0 \text{ for } k \neq j} \quad (3.31)$$

So by driving port  $j$  with an incident voltage  $V_j^+$  and measuring the reflected amplitude  $V_i^-$  on port  $i$  the element  $S_{ij}$  can be found. These measurements can be made using a Virtual Network Analyzer (VNA) to determine very important properties. When measuring, the incident waves on all ports except the  $j^{th}$  port are terminated with matched loads to avoid reflections. The reflection coefficient on any port  $i$  is determined by matching all ports and defined as  $S_{ii}$  whereas

the transmission coefficient from port  $j$  to port  $i$ , when all other ports are matched, is  $S_{ij}$ . These properties are intrinsically related to the impedance and admittance matrices, which are defined as

$$\begin{bmatrix} V_1 \\ V_2 \\ \vdots \\ V_N \end{bmatrix} = \begin{bmatrix} Z_{11} & Z_{12} & \dots & Z_{1N} \\ Z_{21} & & & \vdots \\ \vdots & & \ddots & \\ Z_{N1} & \dots & & Z_{NN} \end{bmatrix} \begin{bmatrix} I_1 \\ I_2 \\ \vdots \\ I_N \end{bmatrix}$$

or

$$[V] = [Z][I] \quad (3.32)$$

where  $Z_{ij}$  is the impedance seen when driving port  $j$  with current  $I_j$  and open circuiting all other ports. The current and voltage are related to the impedance by the equation

$$Z_{ij} = \left. \frac{V_i}{I_j} \right|_{I_k=0 \text{ for } k \neq j} \quad (3.33)$$

The admittance matrix  $[Y]$  is the inverse of the  $[Z]$  matrix, that is

$$[Y] = [Z]^{-1} \quad (3.34)$$

and has the form

$$\begin{bmatrix} I_1 \\ I_2 \\ \vdots \\ I_N \end{bmatrix} = \begin{bmatrix} Y_{11} & Y_{12} & \dots & Y_{1N} \\ Y_{21} & & & \vdots \\ \vdots & & \ddots & \\ Y_{N1} & \dots & & Y_{NN} \end{bmatrix} \begin{bmatrix} V_1 \\ V_2 \\ \vdots \\ V_N \end{bmatrix}$$

where  $Y_{ij}$  can be found as

$$Y_{ij} = \left. \frac{I_i}{V_j} \right|_{V_k=0 \text{ for } k \neq j} \quad (3.35)$$

The  $[Z]$  and  $[Y]$  matrices have special properties when carried through the reciprocity theorem,

$$\oint_S \vec{E}_a \times \vec{H}_b = \oint_S \vec{E}_b \times \vec{H}_a \cdot d\vec{s} \quad (3.36)$$

where  $\vec{E}_a$ ,  $\vec{H}_a$ ,  $\vec{E}_b$  and  $\vec{H}_b$  are the electric and magnetic fields anywhere in the network from independent sources  $a$  and  $b$ , and  $S$  in this case is the closed surface following the boundaries of the network. The fields due to the sources can be evaluated as

$$\begin{aligned}
\bar{E}_{1a} &= V_{1a}\bar{e}_1, \bar{H}_{1a} = I_{1a}\bar{h}_1 \\
\bar{E}_{1b} &= V_{1b}\bar{e}_1, \bar{H}_{1b} = I_{1b}\bar{h}_1 \\
\bar{E}_{2a} &= V_{2a}\bar{e}_2, \bar{H}_{2a} = I_{2a}\bar{h}_2 \\
\bar{E}_{2b} &= V_{2b}\bar{e}_2, \bar{H}_{2b} = I_{2b}\bar{h}_2
\end{aligned} \tag{3.37}$$

where the transverse modal fields of ports 1 and 2 are  $\bar{e}_1, \bar{h}_1$  and  $\bar{e}_2, \bar{h}_2$  respectively, and  $\bar{E}_{1a}$  is the transverse electric field at plane  $t_1$  of port 1 due to source  $a$ . Upon substitution of 3.37 into 3.36 the resultant equation is

$$(V_{1a}I_{1b} - V_{1b}I_{1a}) \int_{S_1} \bar{e}_1 \times \bar{h}_1 \cdot d\bar{s} + (V_{2a}I_{2b} - V_{2b}I_{2a}) \int_{S_2} \bar{e}_2 \times \bar{h}_2 \cdot d\bar{s} = 0 \tag{3.38}$$

where  $S_1$  and  $S_2$  are cross sectional areas at the planes of ports 1 and 2. This can be rewritten when taking into account the power formula

$$P = \frac{VI^*}{2} \tag{3.39}$$

where  $I^*$  is the conjugate  $[I]$  matrix and implies that  $C_1 = C_2 = 1$  so that Eqn. 3.38 can be rewritten as

$$\int_{S_1} \bar{e}_1 \times \bar{h}_1 \cdot d\bar{s} = \int_{S_2} \bar{e}_2 \times \bar{h}_2 \cdot d\bar{s} = 1 \tag{3.40}$$

and reduces Eqn. 3.38 to

$$V_{1a}I_{1b} - V_{1b}I_{1a} + V_{2a}I_{2b} - V_{2b}I_{2a} = 0 \tag{3.41}$$

When applying the above to a 2 port network and respective  $2 \times 2$  admittance matrix to eliminate the currents gives

$$\begin{aligned}
I_1 &= Y_{11}V_1 + Y_{12}V_2 \\
I_2 &= Y_{21}V_1 + Y_{22}V_2
\end{aligned}$$

which can be substituted into Eqn. 3.41 to give

$$(V_{1a}V_{2b} - V_{1b}V_{2a})(Y_{12} - Y_{21}) = 0 \tag{3.42}$$

where the independent sources  $a$  and  $b$  allow the voltages  $V_{1a}$ ,  $V_{1b}$ ,  $V_{2a}$ , and  $V_{2b}$  to take on arbitrary values, and thus to satisfy 3.42 for any and all sources,  $Y_{ij} = Y_{ji}$ . Because the admittance and impedance matrices are inverses, if  $[Y]$  is symmetric, then so too is  $[Z]$ .

The admittance and impedance matrices are often filled with complex values, which makes their analysis arduous and complex: this is why the scattering matrix as the measure can be expressed in terms of input and output power. The terms within the impedance and admittance matrices can be written as

$$\begin{aligned} V_n &= V_n^+ + V_n^- \\ I_n &= I_n^+ - I_n^- = V_n^+ - V_n^- \end{aligned} \quad (3.43)$$

so the definition from Eqn. 3.32 can be used with the above equations to give the relations

$$[Z][I] = [Z][V^+] - [Z][V^-] = [V] = [V^+] + [V^-] \quad (3.44)$$

or

$$([Z] + [U])[V^-] = ([Z] - [U])[V^+] \quad (3.45)$$

where  $[U]$  is the unitary or identity matrix and is defined as

$$[U] = \begin{bmatrix} 1 & 0 & \dots & 0 \\ 0 & 1 & & \vdots \\ \vdots & & \ddots & \\ 0 & \dots & & 1 \end{bmatrix}$$

comparing equations 3.30 and 3.44 leads to the equivalency

$$[S] = ([Z] + [U])^{-1}([Z] - [U]) \quad (3.46)$$

or in terms of  $[S]$

$$[Z] = ([U] + [S])([U] - [S])^{-1} \quad (3.47)$$

and results in writing the scattering matrix in terms of values of the impedance matrix, and for a single port network this can be reduced to

$$S_{11} = \frac{z_{11} - 1}{z_{11} + 1} \quad (3.48)$$

The scattering parameters thus relate the magnitude and phase of incident and reflected waves traveling on and from a microwave network respectively, and change based on their reference points. The  $[S]$  matrix can be written in terms of the incident and reflected voltages,

$$\begin{aligned} [V^-] &= [S][V^+] \\ [V'^-] &= [S'][V'^+] \end{aligned} \quad (3.49)$$

where the first equation in Eqn. 3.49 refers to the original planes, and the second equation refer to new planes. With

$$\begin{aligned} V(z) &= V_0^+ e^{-j\beta z} + V_0^- e^{j\beta z} \\ I(z) &= \frac{V_0^+}{Z_0} e^{-j\beta z} - \frac{V_0^-}{Z_0} e^{j\beta z} \end{aligned} \quad (3.50)$$

where  $Z_0$  is the characteristic impedance, the new wave amplitudes can be related to the original amplitudes by

$$\begin{aligned} V_n'^+ &= V_n^+ e^{j\theta_n} \\ V_n'^- &= V_n^- e^{-j\theta_n} \end{aligned} \quad (3.51)$$

where the subscript is in reference to the new reference plane located at  $z_n = l_n$  with the original plane arbitrarily placed at  $z_n = 0$ . and

$$\theta_n = \beta_n l_n$$

is the electric length of the reference plane shift of port  $n$ , or in matrix form for an  $N$  port network

$$\begin{bmatrix} e^{j\theta_1} & \dots & 0 \\ \dots & e^{j\theta_2} & \vdots \\ & \ddots & \\ 0 & \dots & e^{j\theta_N} \end{bmatrix} [V'^-] = [S] \begin{bmatrix} e^{-j\theta_1} & \dots & 0 \\ \dots & e^{-j\theta_2} & \vdots \\ & \ddots & \\ 0 & \dots & e^{-j\theta_N} \end{bmatrix} [V'^+] \quad (3.52)$$

Multiplying the RHS by the inverse matrix on the LHS results in

$$[V'^-] = \begin{bmatrix} e^{-j\theta_1} & \dots & 0 \\ \dots & e^{-j\theta_2} & \vdots \\ & \ddots & \\ 0 & \dots & e^{-j\theta_N} \end{bmatrix} [S] \begin{bmatrix} e^{-j\theta_1} & \dots & 0 \\ \dots & e^{-j\theta_2} & \vdots \\ & \ddots & \\ 0 & \dots & e^{-j\theta_N} \end{bmatrix} [V'^+]$$

which when compared to Eqn. 3.49 shows

$$[S'] = \begin{bmatrix} e^{-j\theta_1} & \dots & 0 \\ \dots & e^{-j\theta_2} & \vdots \\ & \ddots & \\ 0 & \dots & e^{-j\theta_N} \end{bmatrix} [S] \begin{bmatrix} e^{-j\theta_1} & \dots & 0 \\ \dots & e^{-j\theta_2} & \vdots \\ & \ddots & \\ 0 & \dots & e^{-j\theta_N} \end{bmatrix} \quad (3.53)$$

Where  $S'_{mn} = e^{-2j\theta_n} S_{mn}$  meaning the phase is shifted by twice the electrical length, because the wave travels the length twice, upon incident and reflection. The mathematical relationship between the  $S$ , and  $Z$  matrices is as follows

$$\begin{bmatrix} S_{11} & S_{12} \\ S_{21} & S_{22} \end{bmatrix} = \begin{bmatrix} \frac{(Z_{11}-Z_0)(Z_{22}+Z_0)-Z_{12}Z_{21}}{\Delta Z} & \frac{2Z_{12}Z_0}{\Delta Z} \\ \frac{2Z_{21}Z_0}{\Delta Z} & \frac{(Z_{11}+Z_0)(Z_{22}-Z_0)-Z_{12}Z_{21}}{\Delta Z} \end{bmatrix} \quad (3.54)$$

where

$$\Delta Z = (Z_{11} + Z_0)(Z_{22} + Z_0) - Z_{12}Z_{21} \quad (3.55)$$

And is important for converting Impedance matrices to Scattering parameter matrices.

### 3.1.3.1 Scattering Parameters and Power

In regards to Eqn. 3.43, the total voltage and current seen in network analysis can be rewritten as

$$\begin{aligned} V &= V_0^+ + V_0^- \\ I &= \frac{V_0^+ - V_0^-}{Z_0} \end{aligned} \quad (3.56)$$

To find the incident and reflected wave amplitudes in terms of total voltage and current, Eqn. 3.56 must be inverted resulting in

$$\begin{aligned} V_0^+ &= \frac{V + Z_0 I}{2} \\ V_0^- &= \frac{V - Z_0 I}{2} \end{aligned} \quad (3.57)$$

so that the average load power can be written as

$$\begin{aligned}
 P_L &= \frac{\text{Re}(VI^*)}{2} \\
 &= \frac{1}{2Z_0} \text{Re}(|V_0^+|^2 - V_0^+ V_0^{-*} + V_0^{+*} V_0^- - |V_0^-|^2) \\
 &= \frac{1}{2Z_0} (|V_0^+|^2 - |V_0^-|^2)
 \end{aligned} \tag{3.58}$$

as the quantities  $V_0^+ V_0^{-*}$  and  $V_0^{+*} V_0^-$  are purely imaginary. This result though, is only valid when the characteristic impedance is real and does not apply when  $Z_0$  is complex. The reflection coefficient  $\Gamma_p$  for the power can be defined as

$$\Gamma_p = \frac{V - Z_R^* I}{V + Z_R I} = \frac{Z_L - Z_R^*}{Z_L + Z_R^*} \tag{3.59}$$

where  $Z_L$  and  $Z_R$  are the load and reference impedance respectively, and when  $Z_R = Z_0$  and is real, reduces to

$$\Gamma = \frac{Z_L - Z_0}{Z_L + Z_0} \tag{3.60}$$

For a basic circuit system consisting of an input voltage  $V_0$  from a generator with impedance  $Z_g$  through a load of impedance  $Z_L$  along with the voltage and current equations from 3.50 the voltage, current, and power equations can be written as

$$\begin{aligned}
 V &= V_0 \frac{Z_L}{Z_L + Z_g} \\
 I &= \frac{V_0}{Z_L + Z_g} \\
 P_L &= \frac{V_0^2}{2} \frac{R_L}{|Z_L + Z_g|^2}
 \end{aligned} \tag{3.61}$$

where

$$Z_L = R_L + jX_L$$

These equations are very important, as when designing a microwave probe, the power delivered to the load needs to be maximum as the load in this case is the probe itself. The power is maximum when  $Z_g = Z_L^*$ , and when maximum power is delivered to the probe, the reflection from a sample  $\Gamma_{DUT}$  must be maximum to ensure maximum power is detected from from a material

being scanned. For probes read in reflection mode, a maximum  $\Gamma_L$  allows for an extremely sharp  $Q$  and very sensitive changes in  $Z_0$  allowing for defects to be detected in the sample. When probes are in read mode, the  $S_{11}$  parameter is equivalent to  $\Gamma_{DUT}$ , and this is why the scattering parameters are so important when designing microwave probes. This proof can be found by utilizing the  $ABCD$ -parameters, also called the transmission matrix. These parameters are used when the networks being analyzed are cascaded, or there is more than one network being analyzed so that the networks can be combined. This is the case in this system as the probe, DAQ and excitation hardware are independent network, but can be cascaded to achieve the overall output via the  $ABCD$ -parameters. For two two-port networks, the  $ABCD$ -matrix is defined as

$$\begin{aligned} V_1 &= AV_2 + BI_2 \\ I_1 &= CV_2 + DI_2 \end{aligned} \quad (3.62)$$

or,

$$\begin{bmatrix} V_1 \\ I_1 \end{bmatrix} = \begin{bmatrix} A & B \\ C & D \end{bmatrix} \begin{bmatrix} V_2 \\ I_2 \end{bmatrix} \quad (3.63)$$

When cascaded, the equations are

$$\begin{bmatrix} V_1 \\ I_1 \end{bmatrix} = \begin{bmatrix} A_1 & B_1 \\ C_1 & D_1 \end{bmatrix} \begin{bmatrix} V_2 \\ I_2 \end{bmatrix} \quad (3.64a)$$

$$\begin{bmatrix} V_2 \\ I_2 \end{bmatrix} = \begin{bmatrix} A_2 & B_2 \\ C_2 & D_2 \end{bmatrix} \begin{bmatrix} V_3 \\ I_3 \end{bmatrix} \quad (3.64b)$$

So that when Eqn. 3.64b is substituted into Eqn. 3.64a the resultant equation becomes

$$\begin{bmatrix} V_1 \\ I_1 \end{bmatrix} = \begin{bmatrix} A_1 & B_1 \\ C_1 & D_1 \end{bmatrix} \begin{bmatrix} A_2 & B_2 \\ C_2 & D_2 \end{bmatrix} \begin{bmatrix} V_3 \\ I_3 \end{bmatrix} \quad (3.65)$$

The relation between the  $S$ -matrix and  $ABCD$ - matrix is as follows,

$$\begin{bmatrix} S_{11} & S_{12} \\ S_{21} & S_{22} \end{bmatrix} = \begin{bmatrix} \frac{A+B/Z_0-CZ_0-D}{A+B/Z_0+CZ_0+D} & \frac{2(AD-BC)}{A+B/Z_0+CZ_0+D} \\ \frac{2}{A+B/Z_0+CZ_0+D} & \frac{-A+B/Z_0-CZ_0+D}{A+B/Z_0+CZ_0+D} \end{bmatrix} \quad (3.66)$$

To see how the reflection coefficient,  $\Gamma$  is related to the  $S_{11}$  parameter, the equation B.21 is used for  $\gamma$  and the identities

$$\cosh(x) = \frac{e^x + e^{-x}}{2} \quad (3.67a)$$

$$\sinh(x) = \frac{e^x - e^{-x}}{2} \quad (3.67b)$$

are used when regarding the  $ABCD$  and  $Z$  parameters vs the  $S$  parameters. When the limits of a line of length  $l$ , with characteristic impedance  $Z_0$  and input impedance  $Z_L$  are taken to  $\infty$ , the relation is

$$|S_{11}| = \lim_{l \rightarrow \infty} \left| \frac{(Z_0^2 - Z_L^2)\sinh(\gamma l)}{2Z_L Z_0 \cosh(\gamma l) + (Z_L^2 + Z_0^2)\sinh(\gamma l)} \right| \quad (3.68a)$$

$$\approx \left| \frac{(Z_0^2 - Z_L^2)e^{\gamma l}}{2Z_L Z_0 e^{\gamma l} + (Z_L^2 + Z_0^2)e^{\gamma l}} \right| \quad (3.68b)$$

$$= \left| \frac{(Z_0 - Z_L)(Z_L + Z_0)}{2Z_L Z_0 + Z_L^2 + Z_0^2} \right| \quad (3.68c)$$

$$= \left| \frac{Z_0 - Z_L}{Z_0 + Z_L} \right| \quad (3.68d)$$

$$= |\Gamma| \quad (3.68e)$$

with Eqn. 3.68d equivalent to Eqn. 3.60 This mathematical proof and the preceding relations are what allow the microwave system to operate in read mode. The power is put through port 1, and the reflected power is read on port 1, and due to the amplitude and phase of the reflected signal, a defect is able to be identified by the precise loss of power seen in the amplitude, and the area is able to be generalized by the phase loss.

## 3.2 Dielectric Evaluation

As shown in the theory section, dielectric permittivity  $\epsilon$  is an extremely important value for the response of a microwave probe. The method of action, simplified, is relatively the same as the low frequency capacitive method. A probe with fixed values will react a known way in air, with a resonant frequency  $F_0$  and when a material with a different permittivity is introduced, the response

will change. Microwave probes are read in either reflection mode, treating the probe as a single port network, with the  $S_{11}$  value equivalent to reflection coefficient read out using the voltage value to back calculate the power and phase of the reflected signal. Probes are also commonly read in two port network configuration, exciting one port and reading on the other. In this configuration, the  $S_{21}$  or  $S_{12}$  value is used, dependent on the port of excitation and reading, as the transmission coefficient to perform the same power and phase calculations. Due to the higher frequency utilized in microwave scanning, the resonance shift seen from varying permittivity is much greater than capacitive scanning. This greater sensitivity, however comes with a loss of penetration depth. Another drawback to microwave dielectric evaluation is the inability to utilize lumped components, which are easier to debug and spontaneously alter for a different response.

### **3.2.1 Review of State-of-the-art high frequency methods for dielectric properties measurement**

#### **3.2.1.1 Probes**

Commonly utilized probes for microwave scanning include waveguides, coaxial cables, split ring resonators, and patch antennas. Waveguides have high penetration depth, but can suffer from decreased sensitivity. Coaxial cables are inverse to this, and can be highly sensitive, but suffer from low penetration depth. Split ring resonators can have relatively good sensitivity and penetration depth, but can perform inadequately on thicker samples. Patch antennas can be utilized for microwave imaging of surface defects, but may not be able to penetrate very far, or if they can, may not be sensitive to small defects. The quality factor associated with split ring resonators make them an attractive choice for microwave imaging, but another downside to their use is the inability to spontaneously alter their response if the fabrication process did not create a resonator matching simulation results, or if the simulation itself was flawed making the results inconsistent. For this reason, a coaxial probe and waveguide were used to calibrate the mini microwave system due to their reliability for the samples imaged.

### 3.2.1.2 Systems

A common method of near and far field microwave imaging is by using a Vector Network Analyzer (VNA), or Phasor Network Analyzer (PNA) as the excitation and read component of a scanning system, with a computer connection for interfacing. [33] [34] [35] This is because the VNA/PNA has the capability of showing the *S*-parameter network response of a microwave probe over a wide frequency band, and allows for the recording of several different resonance frequency shifts, allowing for accurate amplitude and phase readings, a crucial element to microwave imaging. [36] The main drawback is again, the relative size and price of the system, as VNA/PNA equipment size is larger than any system mentioned in the low frequency section, and a price tag for a relatively low frequency VNA system (26.5GHz) is well over a hundred thousand dollars<sup>1</sup>. The microwave frequencies utilized by the mini systems were limited well below this, with the coax probe operating around  $\approx 4$ GHz, and the waveguide operating around  $\approx 7.8$ GHz. If this limit is met with VNA choice, the price is still in excess of eighty three thousand dollars<sup>2</sup>. This price obviously comes with high sensitivity, but the VNA/PNA itself is a general use equipment and is not strictly limited to imaging. The whole point of using it is for port matching and network evaluation. Besides that, the time it takes to perform a scan using it is highly excessive, with scans taking as long as eighteen hours when a scan using the same dimension can be run using a different table top system or the mini system taking as little as thirty minutes. Specific miniaturized microwave systems are common within literature [37] but these systems still utilize a table top RF source, that still is as bulky as a lock-in amplifier volumetrically, and can run over eight thousand dollars refurbished. With the above price tags associated with microwave imaging, an off the shelf system on par with the Ectane system would be astronomically expensive, if it even existed; consumer market microwave imaging systems have yet to be mass produced or sold due to the prohibitively expensive cost of general use equipment like the VNA. The microwave system designed for this paper utilizes relatively the same miniaturized back-end read circuit as is referenced in [37] but is excited by a source the size

---

<sup>1</sup>Keysight website, N5222B PNA

<sup>2</sup>Keysight N5221B

of a cellular phone, and in addition implements an equally small I/Q demodulator allowing for the acquisition of I and Q data simultaneously, thus allowing for direct calculation of power and phase data at half the scan time.

### **3.2.1.3 Applications**

Microwave imaging systems, like capacitive imaging systems have been, and still are frequently utilized for characterization and imaging of defects in composite materials. [13] [38] [37] With long standing reliability and consistency of composite results obtained using microwave scanning systems, recent research has even tested the capabilities on carbon-fibre-reinforced polymer composites (CFRP) to promising results. [14] This imaging can easily be undertaken in a research setting, but again, one of largest drawbacks is the inability to test probes and the system as a whole in field conditions. VNA and PNA systems are well known for their relative delicacy, and their need for repeated calibration in the event that the VNA is compromised in any way, i.e. heavy breathing in some cases; a calibration kit for one of the quoted systems earlier starts at three thousand. This is without mentioning that the cables which are interconnected between the VNA and probe are astoundingly delicate, and should under no circumstance be bent too much or moved excessively as a single cable can cost more than two thousand dollars. Even when using previously mentioned miniaturized reading circuits, the system source is still only capable of operating under lab conditions.

### **3.2.1.4 Limitations**

A comparison of the aforementioned systems and the designed mini system in regards to sensitivity, price, overall size, and field use capability summarizing the above section can be seen in the table below.

System	Relative Sensitivity	Price	Relative Size	Field use?
VNA/PNA	Very High	\$80,000+	Very Bulky	<b>X</b>
High Frequency Source	High	\$10,000+	Bulky	X
Off the Shelf System	∅	∅	∅	∅
Mini system	High	≈\$600	Very Compact	✓

Table 3.1: Common High frequency system comparison

## CHAPTER 4

### MINIATURIZED CAPACITIVE IMAGING SYSTEM

#### 4.1 Probe Design and Characterization

Inductor-capacitor circuits forming resonant tanks one of the commonly used dielectric probes, wherein one of the component variables in equation 2.8, either inductance or capacitance, are fixed allowing for a shift in resonance frequency to rely solely on the unfixed variable. Based on the capacitive theory equations shown in 2.1.1, specifically, equations 2.2 and 2.8, resonance probes were designed with the idea of fixing the inductance value, allowing for any change in center frequency to come from a change in the relative dielectric permittivity. A diagram of the resonant probes is included below in figure 4.1. Six unique high-Q resonance probes were designed for use

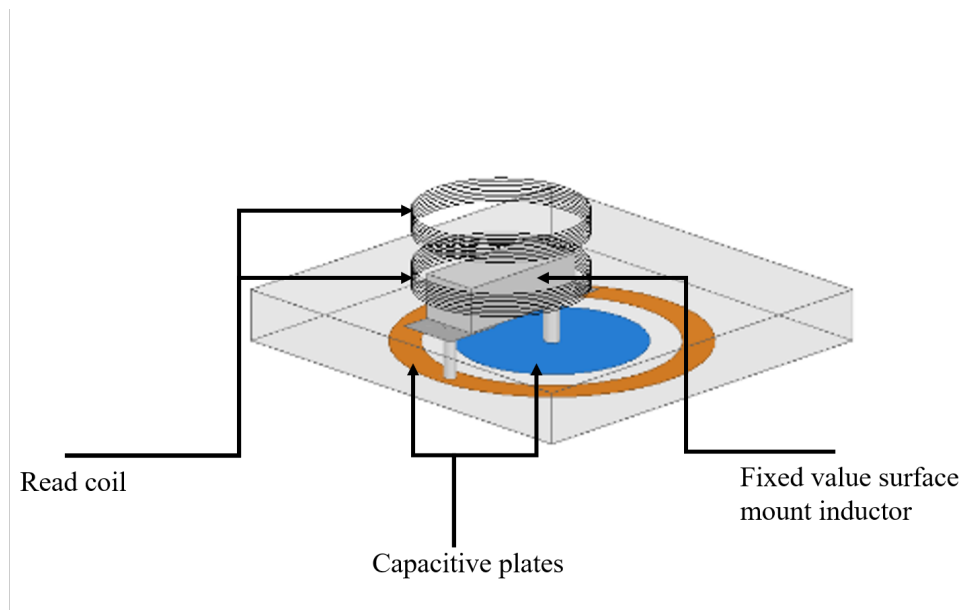


Figure 4.1: LC tank resonance probe design

in combination with the system and are shown below in figure 4.2. The capacitors on for  $C_1$  and  $C_2$  are identical, though the inductors within the LC tank architecture differ. The same pattern follows for  $C_3$  and  $C_4$ , as well as  $C_5$  and  $C_6$ . Probes 1, 3, and 5, are designed for approximately

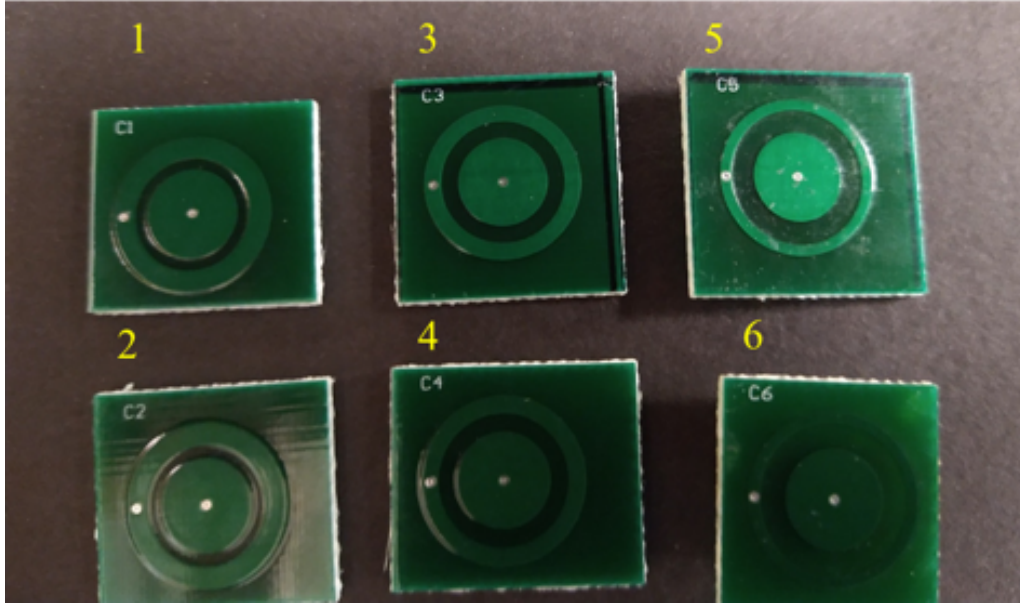


Figure 4.2: Low Frequency Probes designed for the system

Probe	Outer ring diameter	Inner ring diameter	Ring separation	Total diameter
1	2 mm	8 mm	1 mm	14 mm
2	2 mm	8 mm	1 mm	14 mm
3	1.5 mm	8 mm	1.5 mm	14 mm
4	1.5 mm	8 mm	1.5 mm	14 mm
5	1 mm	8 mm	2 mm	14 mm
6	1 mm	8 mm	2 mm	14 mm

Table 4.1: Capacitive probe dimensions

12 MHz and utilize a fixed inductance value of  $56 \mu\text{H}$ , while probes 2, 4, and 6 are designed for approximately 5 MHz and utilize a fixed inductance value of  $75 \mu\text{H}$ . The probes were measured using a Virtual network analyzer, and their sensitivities were initially tested using samples with known dielectric permittivities, such that a comparison in the frequency shift could be obtained upon full measurement of all probes. Initial measurements were obtained in air ( $\epsilon_r \approx 1$ ) and Rogers boards with  $\epsilon_r = 3.66, 6$ , and  $10$ . The resultant measurements for the probes are as follows from low to high frequency, and least to greatest plate separation:

The resultant frequency shift can be seen as a comparison between all six probes following the probe responses, in figure 4.9.

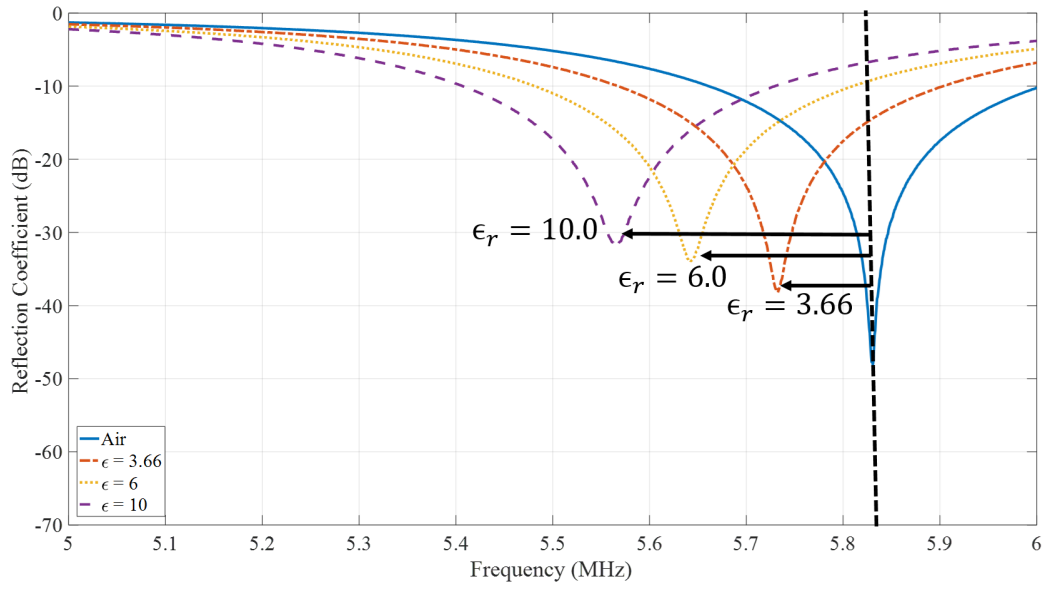


Figure 4.3: Measured reflection coefficient for Probe 2 (1 mm Plate separation)

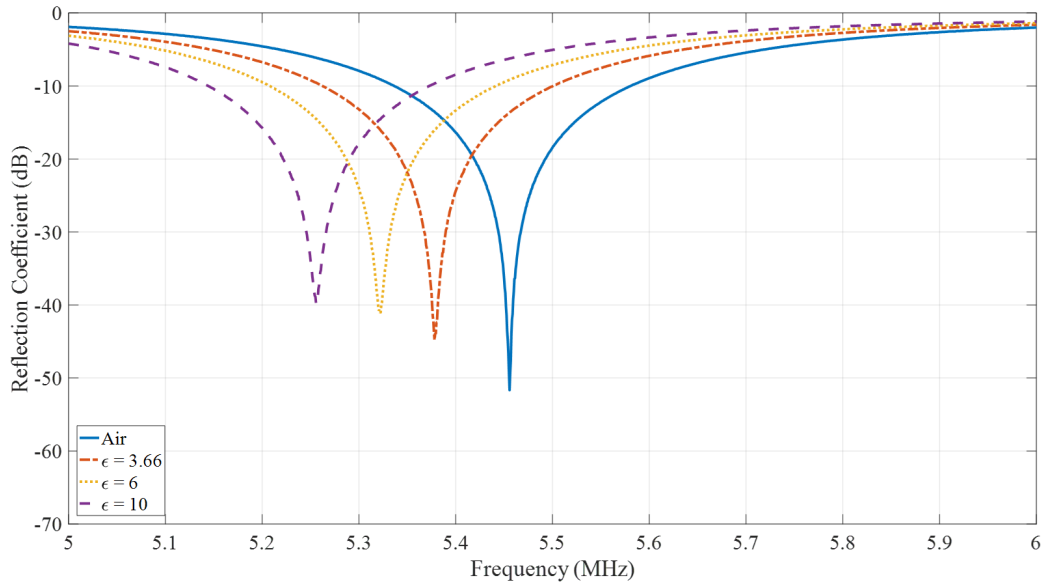


Figure 4.4: Measured reflection coefficient for Probe 4 (1.5 mm Plate separation)

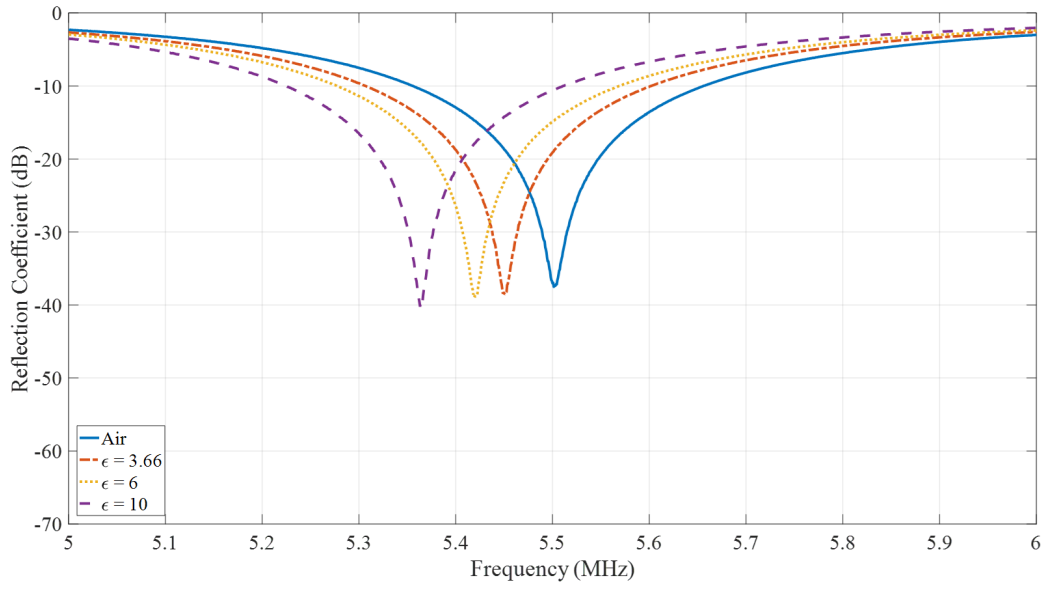


Figure 4.5: Measured reflection coefficient for Probe 6 (2 mm Plate separation)

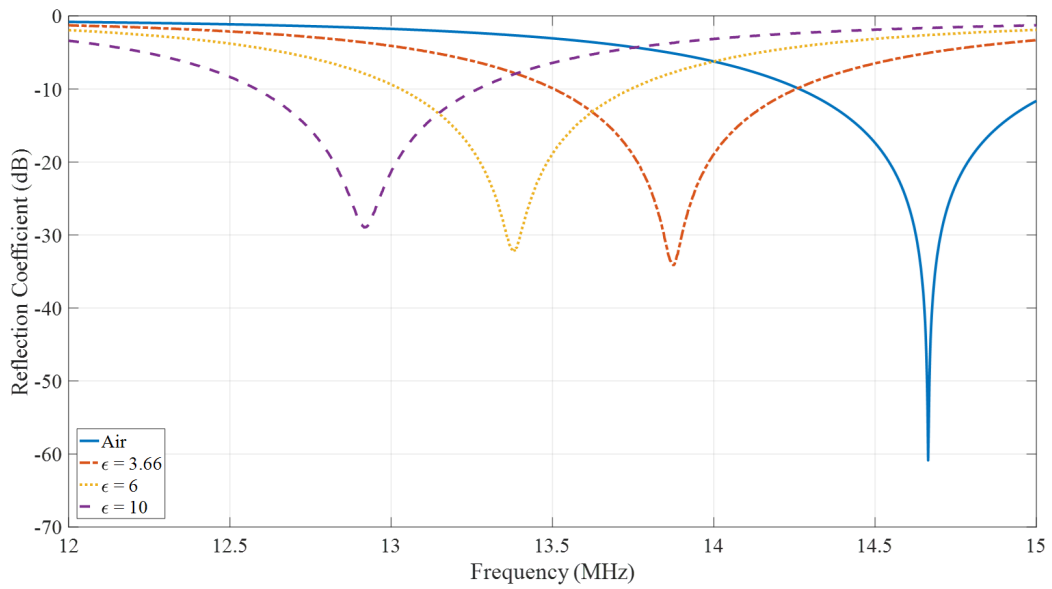


Figure 4.6: Measured reflection coefficient for Probe 1 (1 mm Plate separation)

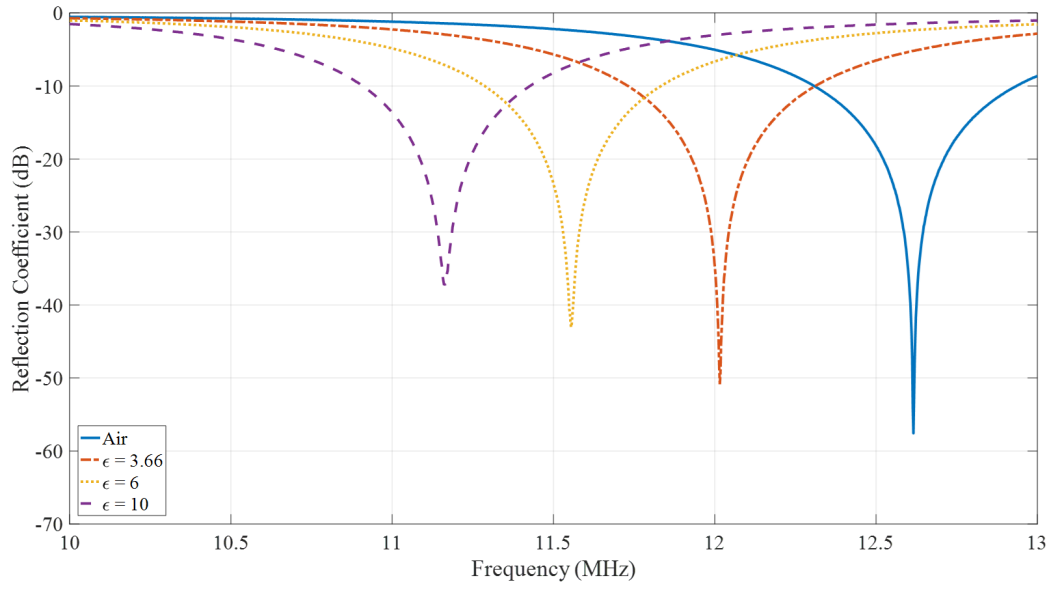


Figure 4.7: Measured reflection coefficient for Probe 3 (1.5 mm Plate separation)

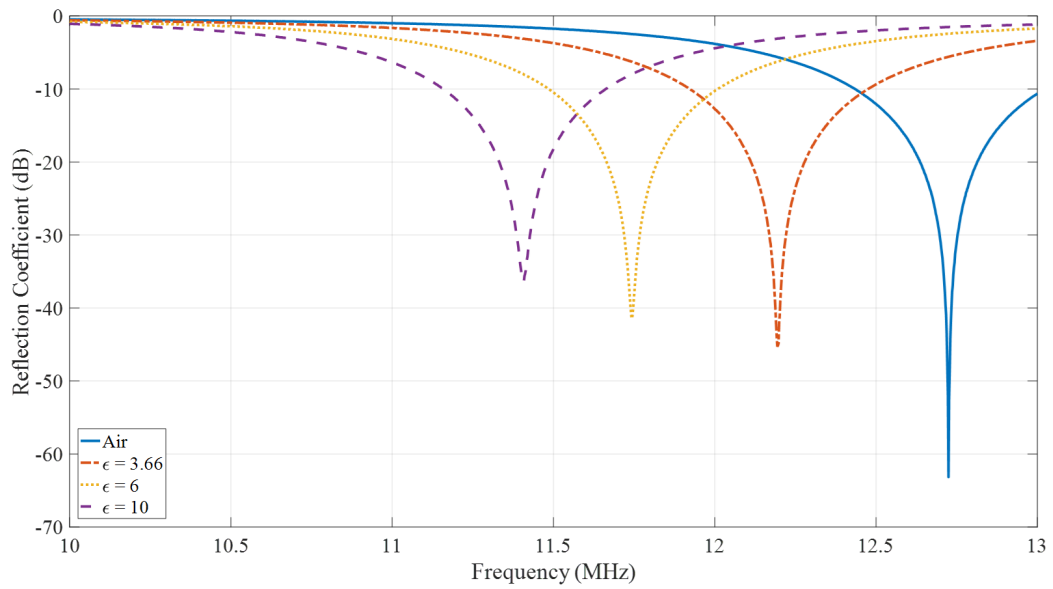


Figure 4.8: Measured reflection coefficient for Probe 5 (2 mm Plate separation)

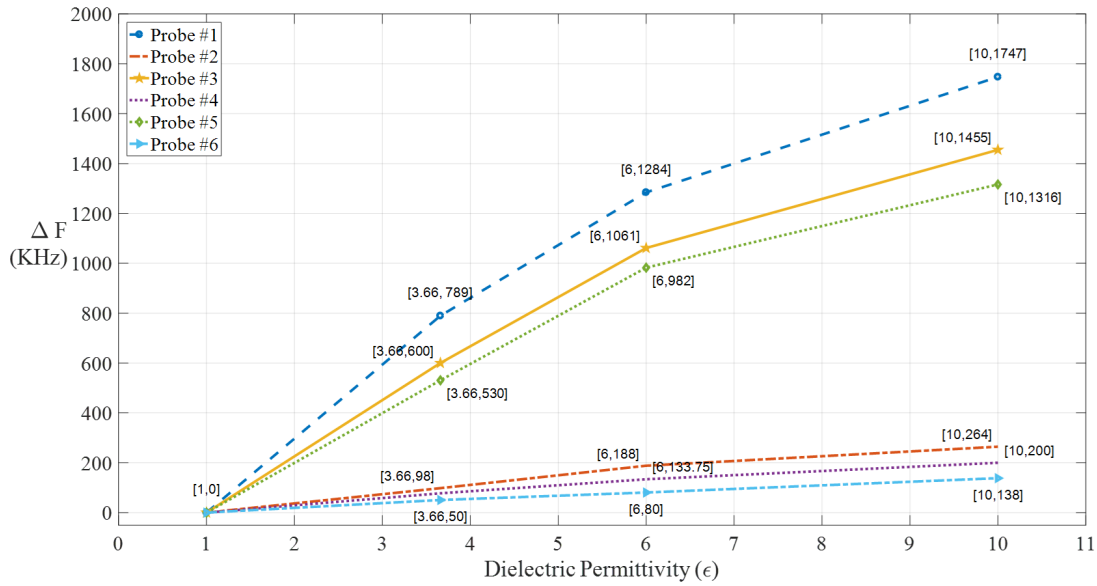


Figure 4.9: Frequency shift comparison between probes 1 through 6

Probe number	$\epsilon_r = 3.66$	$\epsilon_r = 6$	$\epsilon_r = 10$
1	789 KHz	1284 KHz	1787 KHz
2	50 KHz	80 KHz	138 KHz
3	600 KHz	1061 KHz	1455KHz
4	77 KHz	133 KHz	200 KHz
5	580 KHz	932 KHz	1316 KHz
6	98 KHz	188 KHz	264KHz

Table 4.2: Frequency Shift of probes, at varying permittivities

## 4.2 Importance of High Q

The quality factor of a probe is inherently related to its sensitivity. The frequency shift seen by the introduction of a dielectric directly correlates to a change in capacitance seen by the concentric circle capacitor plate, and the reflected power measured. The higher the quality factor, the smaller change in dielectric permittivity can be detected, correlating to a smaller change in capacitance. Knowing the relation between specific permittivities, the frequency shift, and the resultant reflected power can allow for characterization of detected defects based upon the response at a specific input frequency and power.

### 4.3 System Design and Characterization

The low frequency miniaturized system has been designed with the idea of replacing a table top signal generator, lock-in amplifier, and data acquisition system. The system utilizes the AD9958/59 evaluation board as a multi-channel frequency synthesizer; two channels are used, one for the probe excitation, and one for the I/Q demodulator local oscillator (LO). The demodulation is processed utilizing an AD8333 I/Q demodulator and phase shifter. A separate board has been designed utilizing Altium PCB software that allows for a single power connection to power both evaluation boards. The designed PCB also contains an amplifier for the LO signal, as the I/Q LO power has to be within an acceptable range, and the power level is extremely important in regards to the quality of the acquired signal that is to be demodulated. Low pass filters, in the form of an integrator, have also been designed and implemented within the power/amplifier PCB to allow for filtration of any higher frequency noise on the acquired signal, as the output value is read in a DC voltage. Without filtration, the acquired signal is extremely noisy and would require software to clearly see the results, thus the LPFs act as hardware noise reduction. The results acquired, shown further below in section 4.3, are figures composed of the raw acquired I or Q data, and the back-calculated phase or power, depending on graph axis. The full results have been simplified to allow for easy viewing, thus only one or the other is shown in detail.

A block diagram of the designed system can be seen below. Where the Micro-processing unit included will be a raspberry pi, and communicates with an low frequency RF source through an SPI Bus. The signal will run through a bi-directional coupler and the output will be amplified and run through another coupler so that the main input signal can be fed to the coil, while the reflected signal and base reference signal will be fed to an I/Q demodulator to parse the amplitude and phase of the recorded data. This will be run through a low pass filter to remove any higher order harmonic signals and noise, before running through an ADC and back to the micro-processing unit through an SPI bus for data acquisition and review of results. Tests run without the LPF proved to be difficult to reliably image any types of defects without software filtering. The hardware LPF was designed specifically for this application and has been included to alleviate computational strain

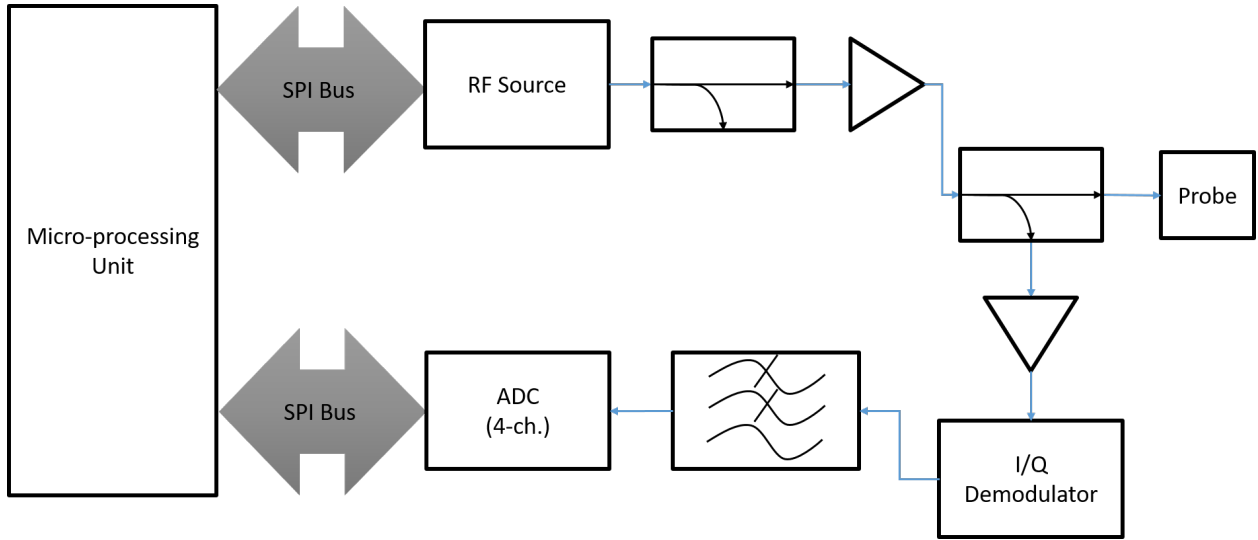


Figure 4.10: Block Diagram of Low Frequency system

placed on data manipulation utilizing the micro-processing unit. Increased noise can be attributed to the inclusion of the amplifiers, though they are necessary to acquire any usable data from usage of the system. The I/Q demodulator demodulates to the in-phase and quadrature phase sinusoidal signals that are 90deg out of phase from each other. The acquired in phase and quadrature phase signals are fed into an imaging code and processed into the reflected power and phase using

$$R = \sqrt{X^2 + Y^2} \quad (4.1a)$$

$$R_{dBm} = 10 * \log_{10}(R) \quad (4.1b)$$

$$\phi_{rad} = \tan^{-1}\left(\frac{Y}{X}\right) \quad (4.1c)$$

$$\phi_{deg} = \phi_{rad} * \frac{180}{\pi} \quad (4.1d)$$

where  $X$  is the in-phase component,  $Y$  is the quadrature phase component,  $R_{dBm}$  is the reflected power in  $dBm$ , and  $\phi_{deg}$  is the reflected phase in degrees.

#### 4.4 System Comparison, Lock-in and Mini

The results acquired are shown below. Scans were run utilizing parameters as identical as could be achieved, in regards to lift off distance, probe speed, and sampling rate. Samples include an aluminum sample, with square, triangle, and circle cut outs. The smallest feature size is the 0.5

*mm* radius circle. A polyethylene sample with sub-surface triangle cut outs was also scanned to test the probe penetration depth with both systems. A GFRP sample with surface impact damage was scanned to test the capability of dielectric evaluation utilizing the designed probe and system. Finally, with all aforementioned results, carbon fiber wrapped steel plate samples provided by Consolidated Edison were scanned. The defect maps provided are included before each plate sample result to show the system results in comparison to the apparent defects contained within the plate samples. The objective for this result comparison is to show that the designed mini system can perform at least as well, if not better, in relative comparison to results acquired using the table top lock-in system.

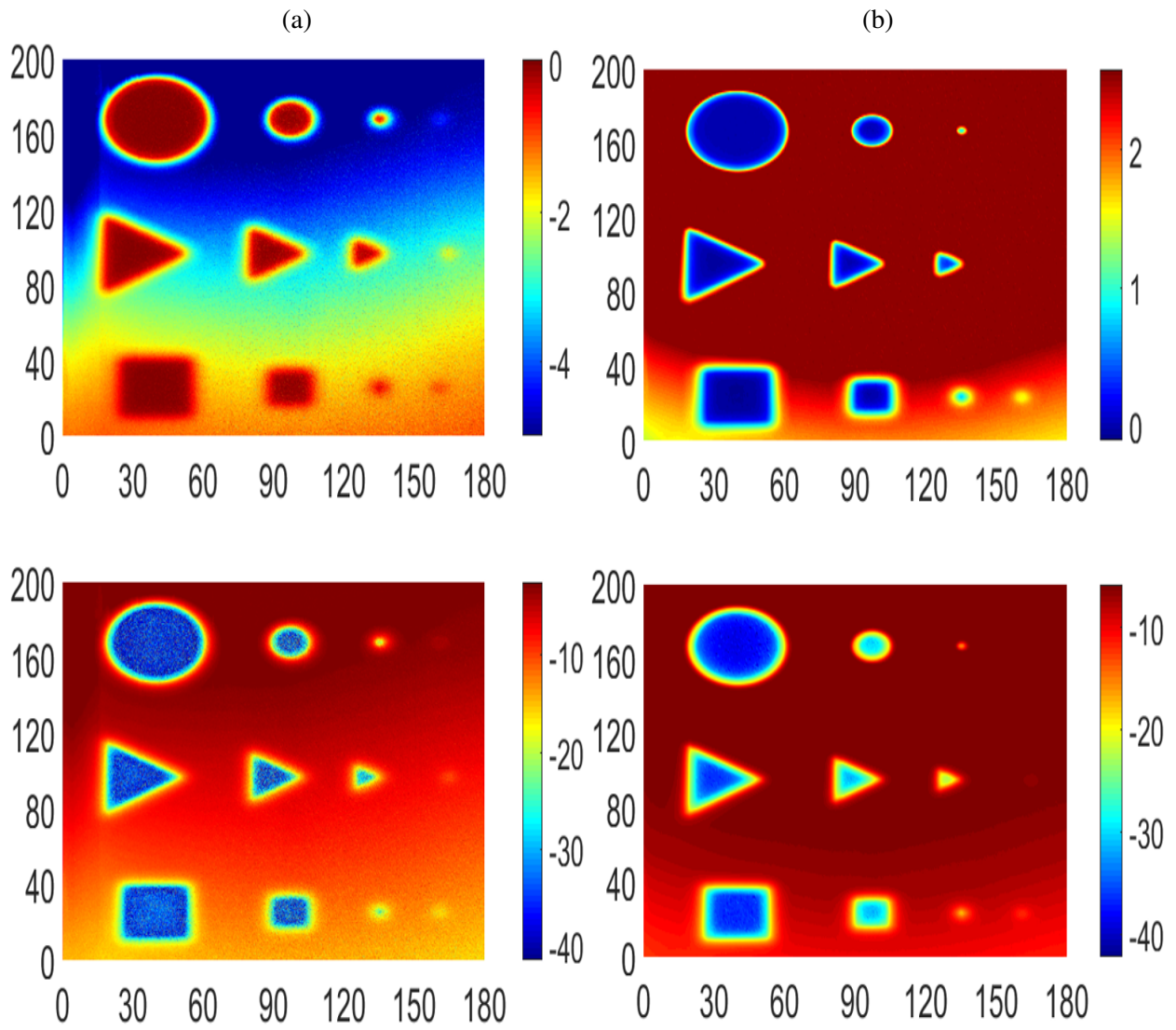


Figure 4.11: Aluminum calibration sample results comparison (a) table top system, (b) mini system

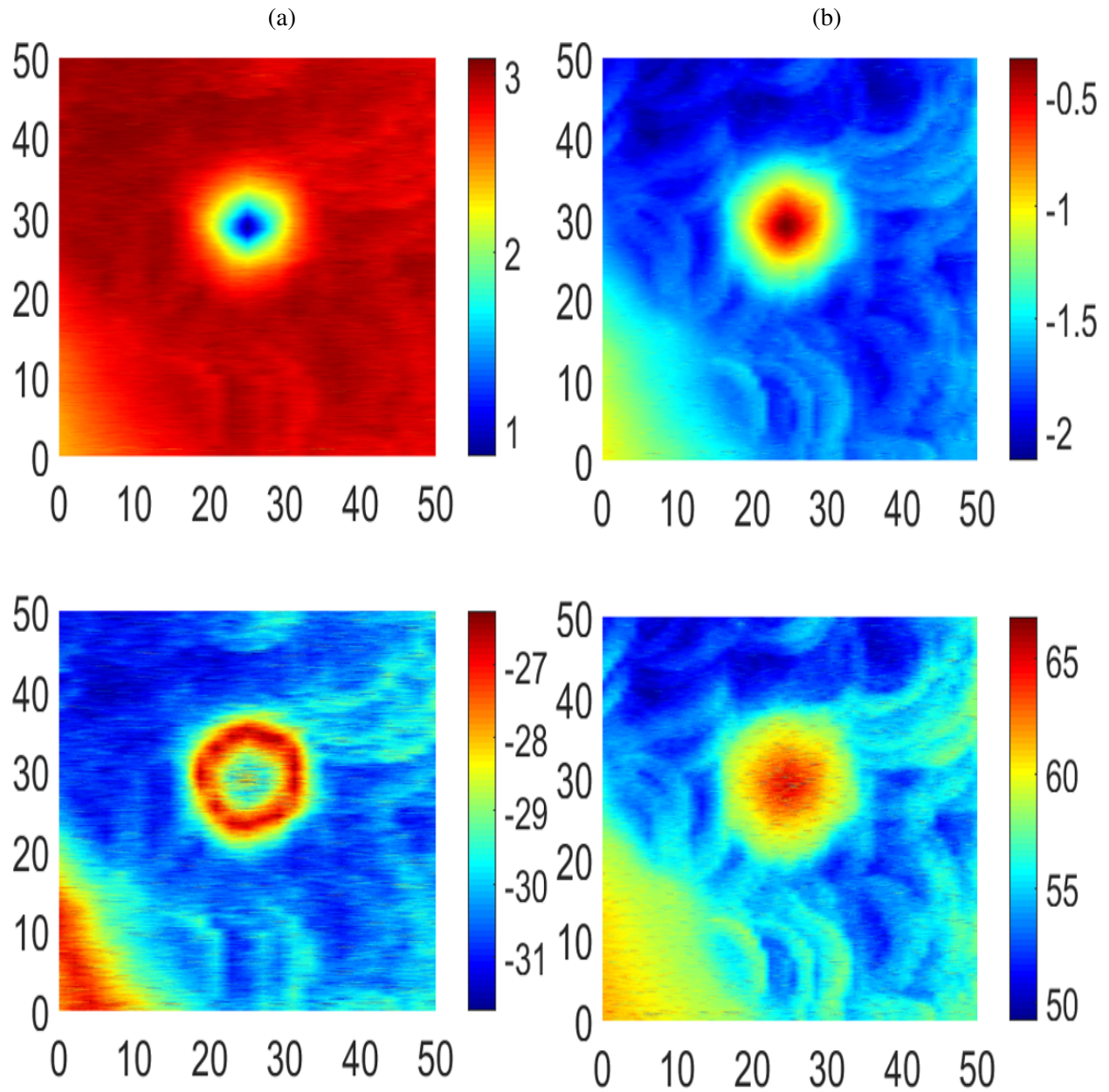


Figure 4.13: GFRP impact damage sample results comparison (a) table top system, (b) mini system

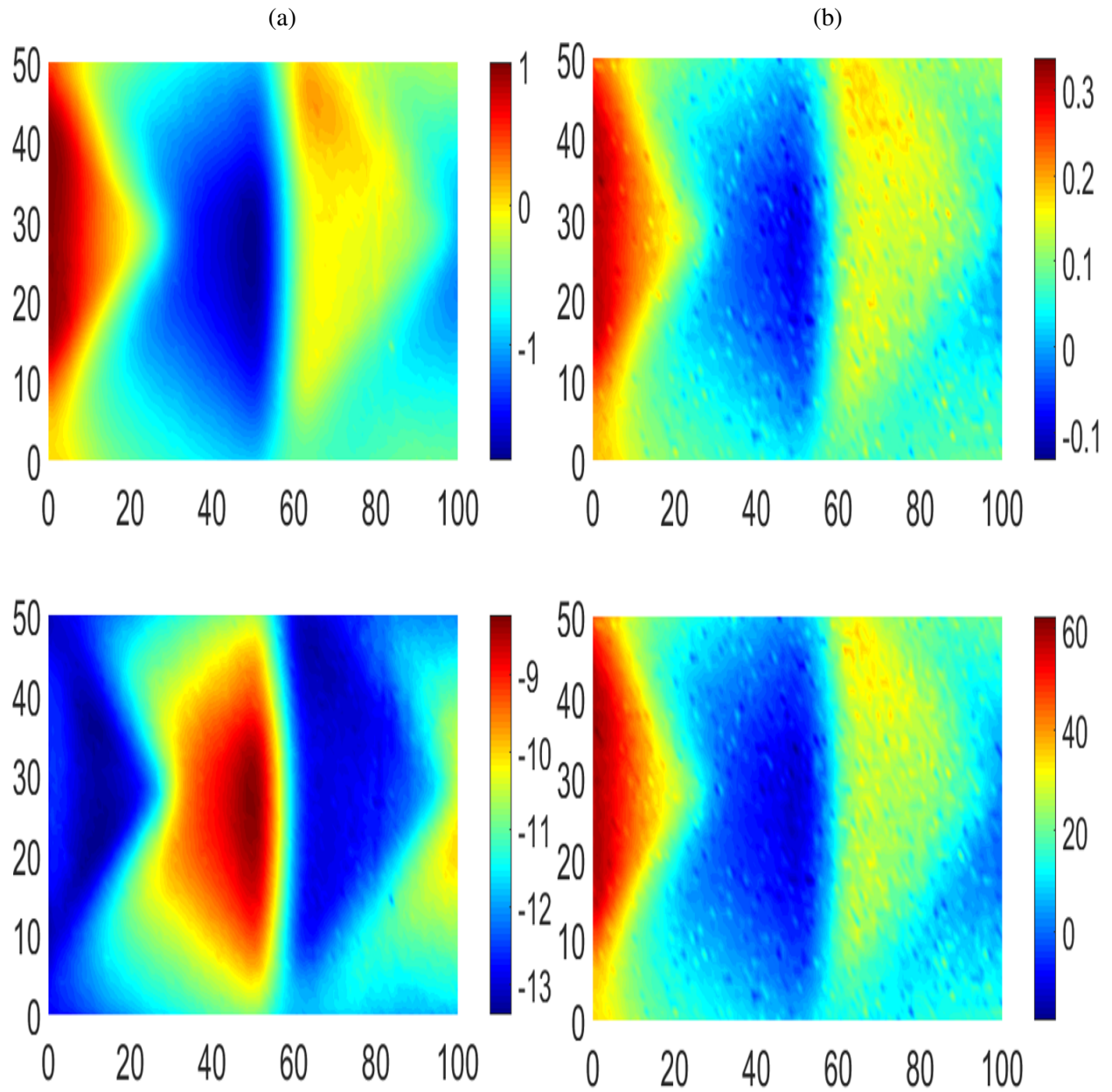


Figure 4.15: PE sample subsurface defect results comparison (a) table top system, (b) mini system

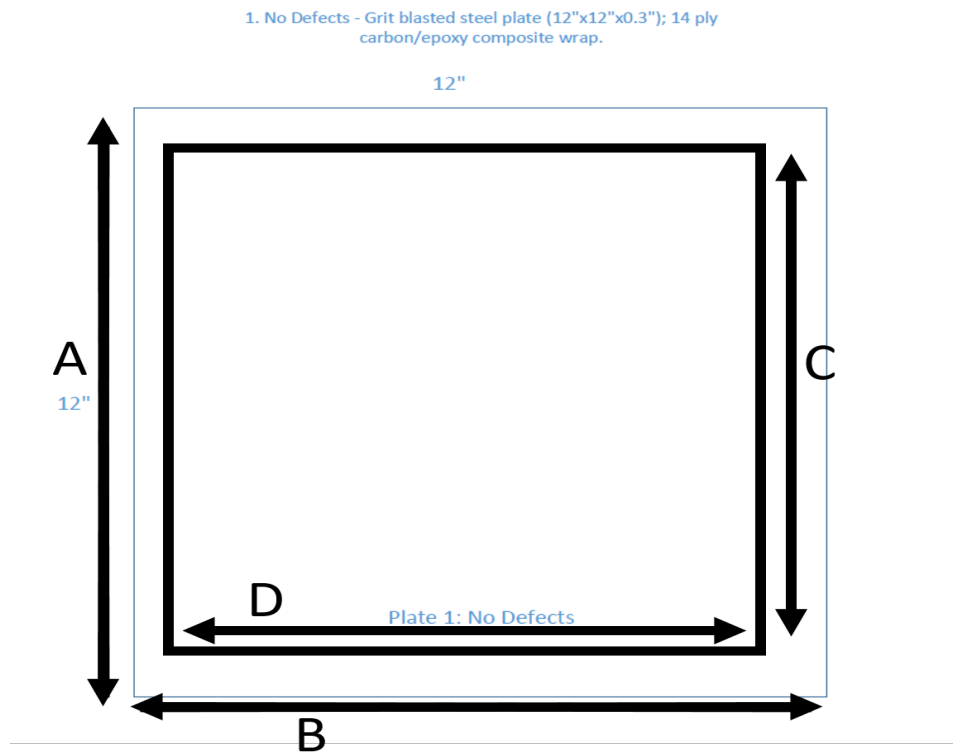


Figure 4.17: Plate 1 Defect Map

Parameter	dimension
A	300mm
B	300mm
C	240mm
D	240mm

Table 4.3: Plate 1 size and scan dimension table

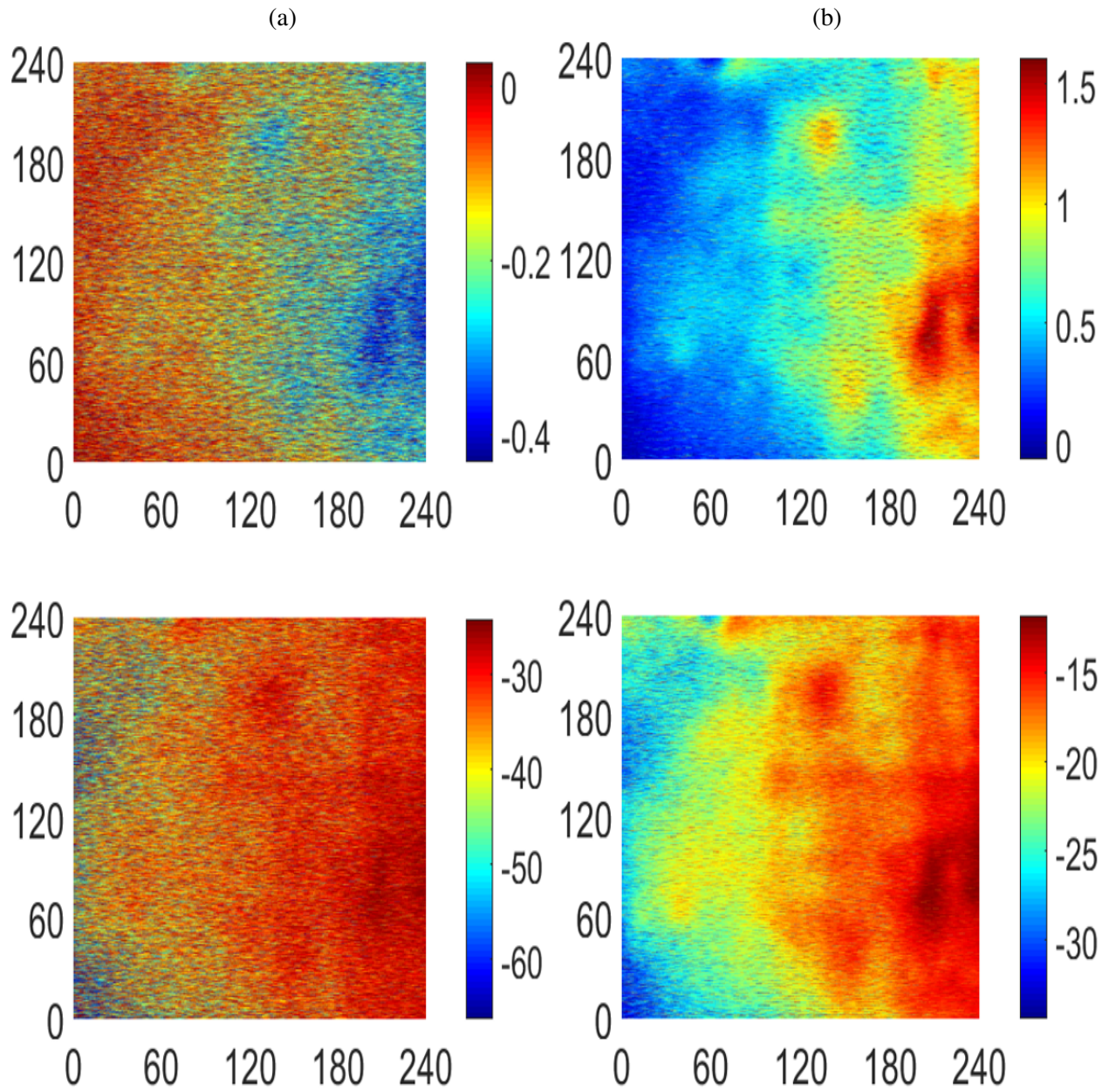


Figure 4.18: Plate 1 results comparison (a) table top system, (b) mini system

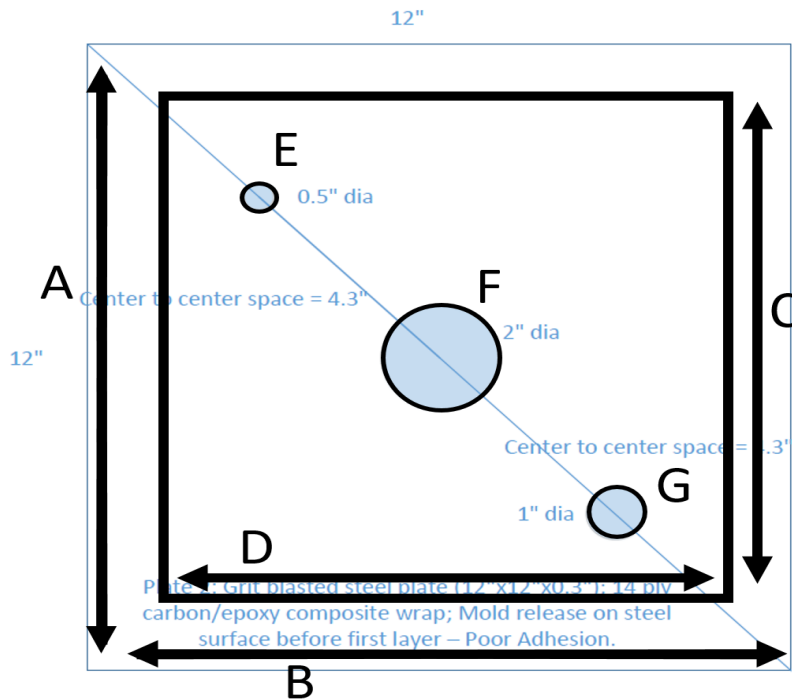


Figure 4.20: Plate 2 Defect Map

Parameter	Dimension	Defect	Detection
A	300mm		
B	300mm		
C	240mm		
D	240mm		
E	25mm dia	Mold	X
F	50mm dia	Mold	X
G	25mm dia	Mold	X

Table 4.4: Plate 2 size, scan, and defect dimension table

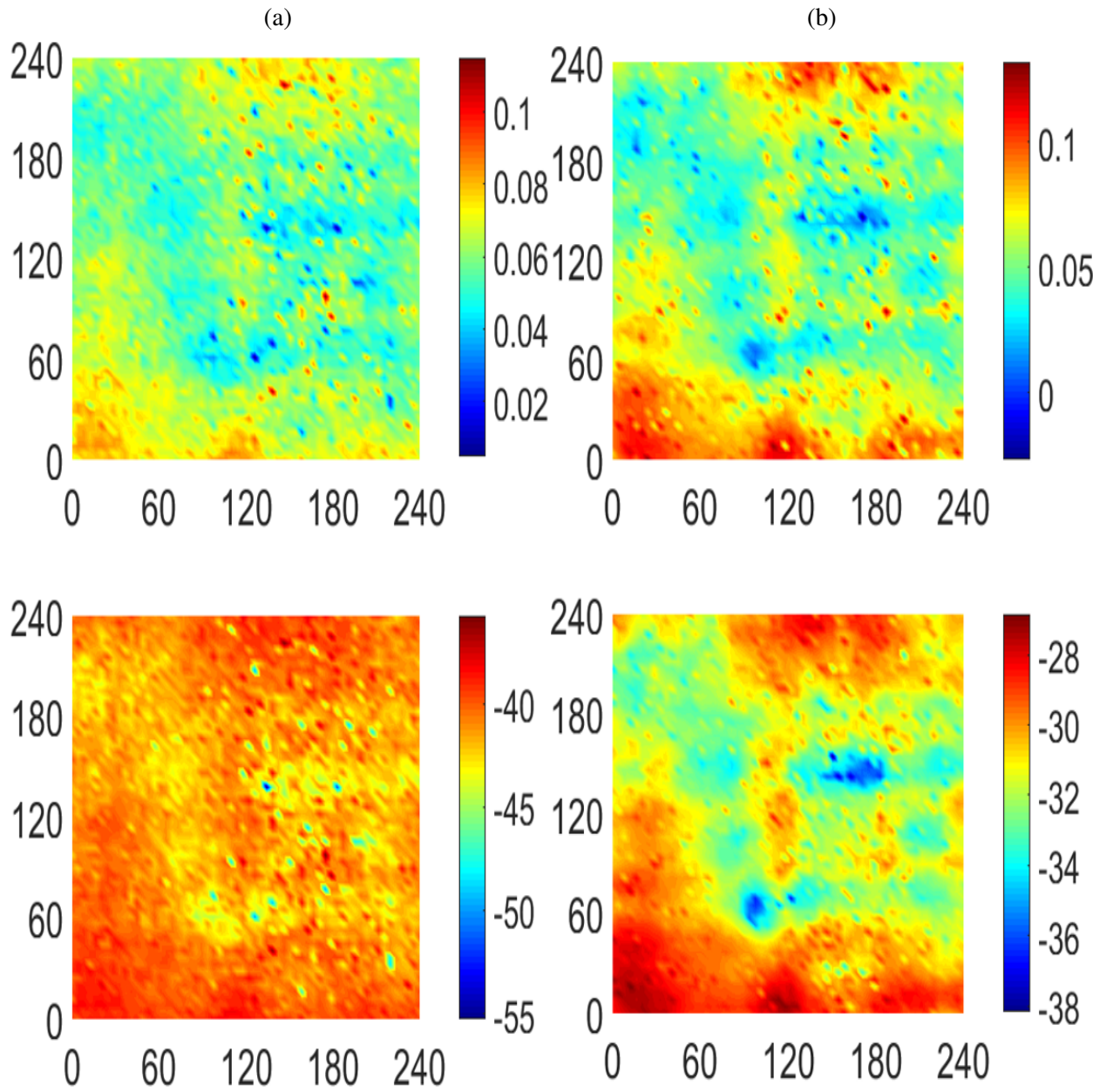


Figure 4.21: Plate 2 results comparison (a) table top system, (b) mini system

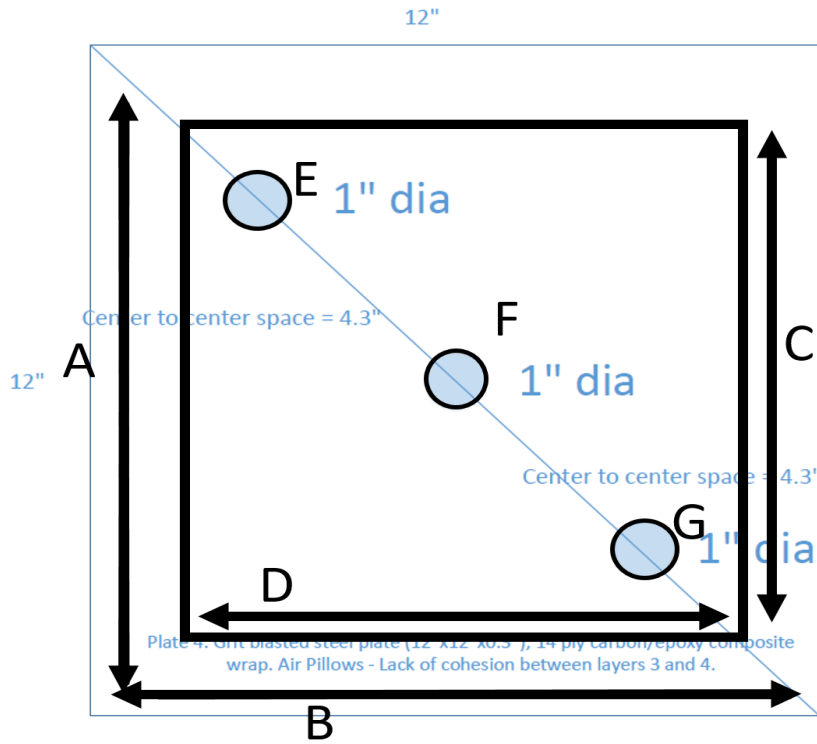


Figure 4.23: Plate 4 Defect Map

Parameter	Dimension	Defect	Detection
A	300mm		
B	300mm		
C	240mm		
D	240mm		
E	25mm dia	Air gap	✓
F	25mm dia	Air gap	✓
G	25mm dia	Air gap	✓

Table 4.5: Plate 4 size, scan, and defect dimension table

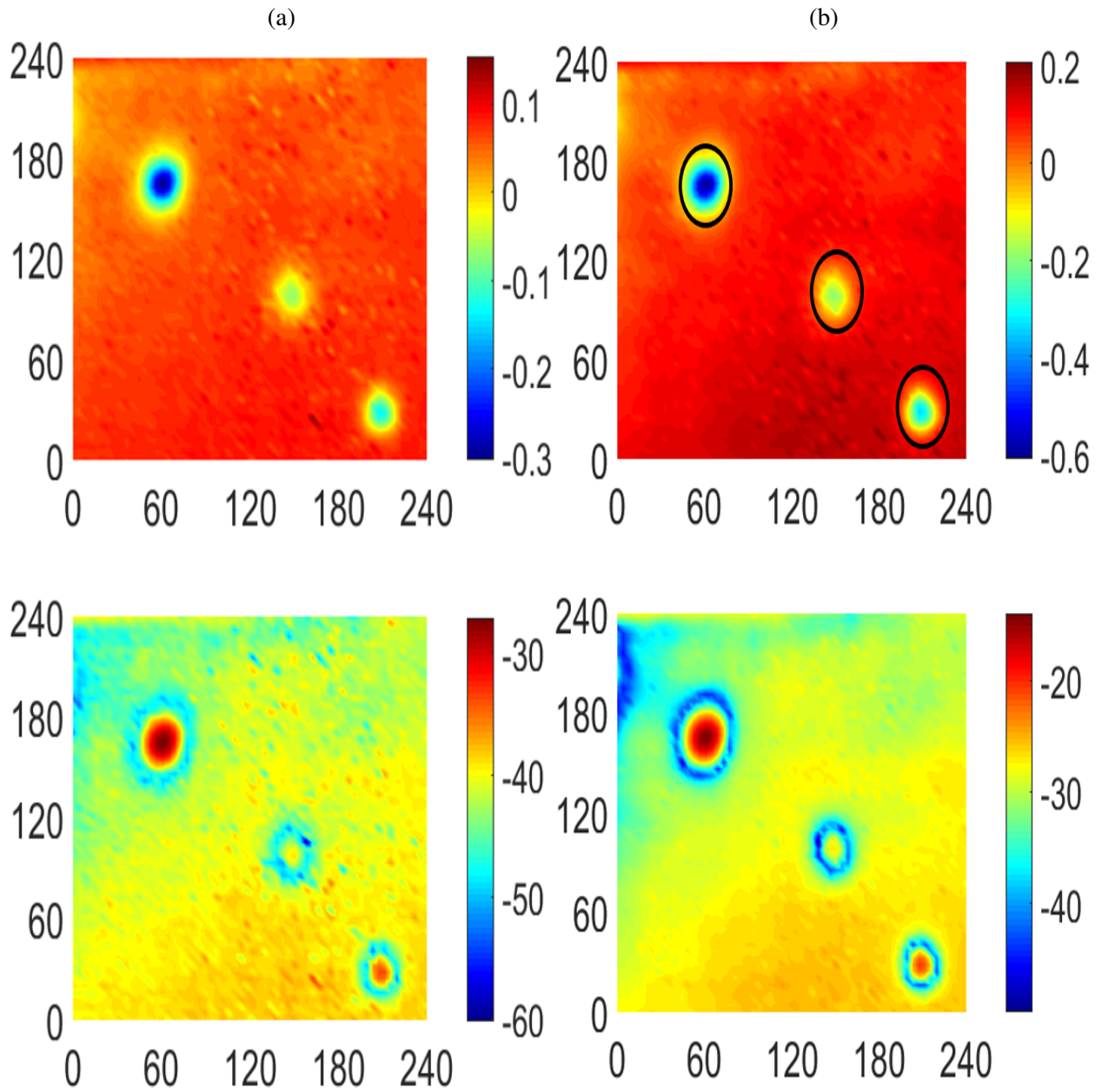


Figure 4.24: Plate 4 results comparison (a) table top system, (b) mini system

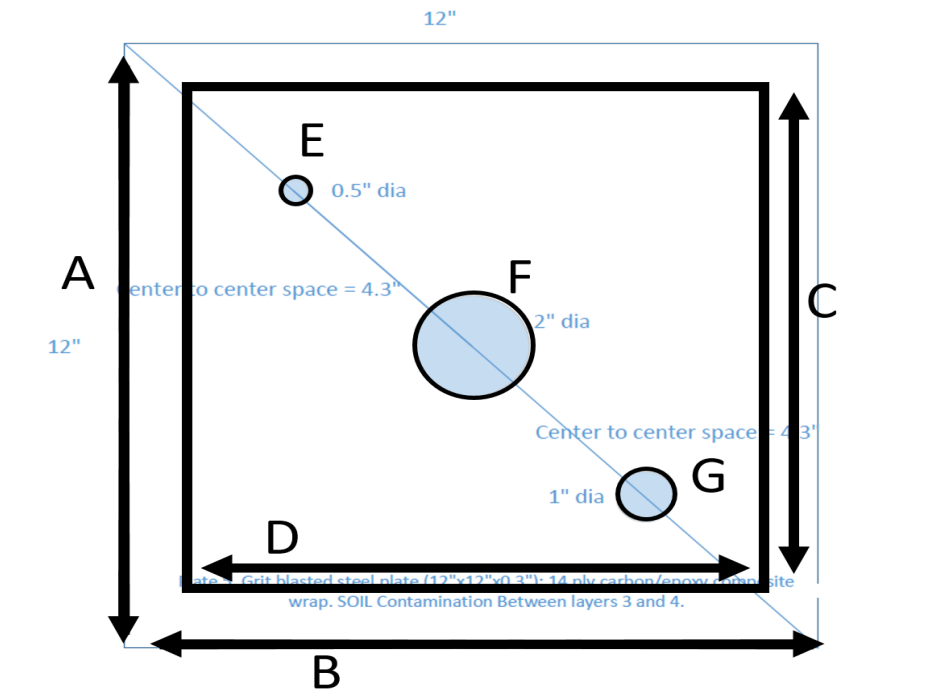


Figure 4.26: Plate 5 Defect Map

Parameter	Dimension	Defect	Detection
A	300mm		
B	300mm		
C	200mm		
D	240mm		
E	12.5mm dia	Soil contamination	✓
F	50mm dia	Soil contamination	✓
G	25mm dia	Soil contamination	✓

Table 4.6: Plate 5 size, scan, and defect dimension table

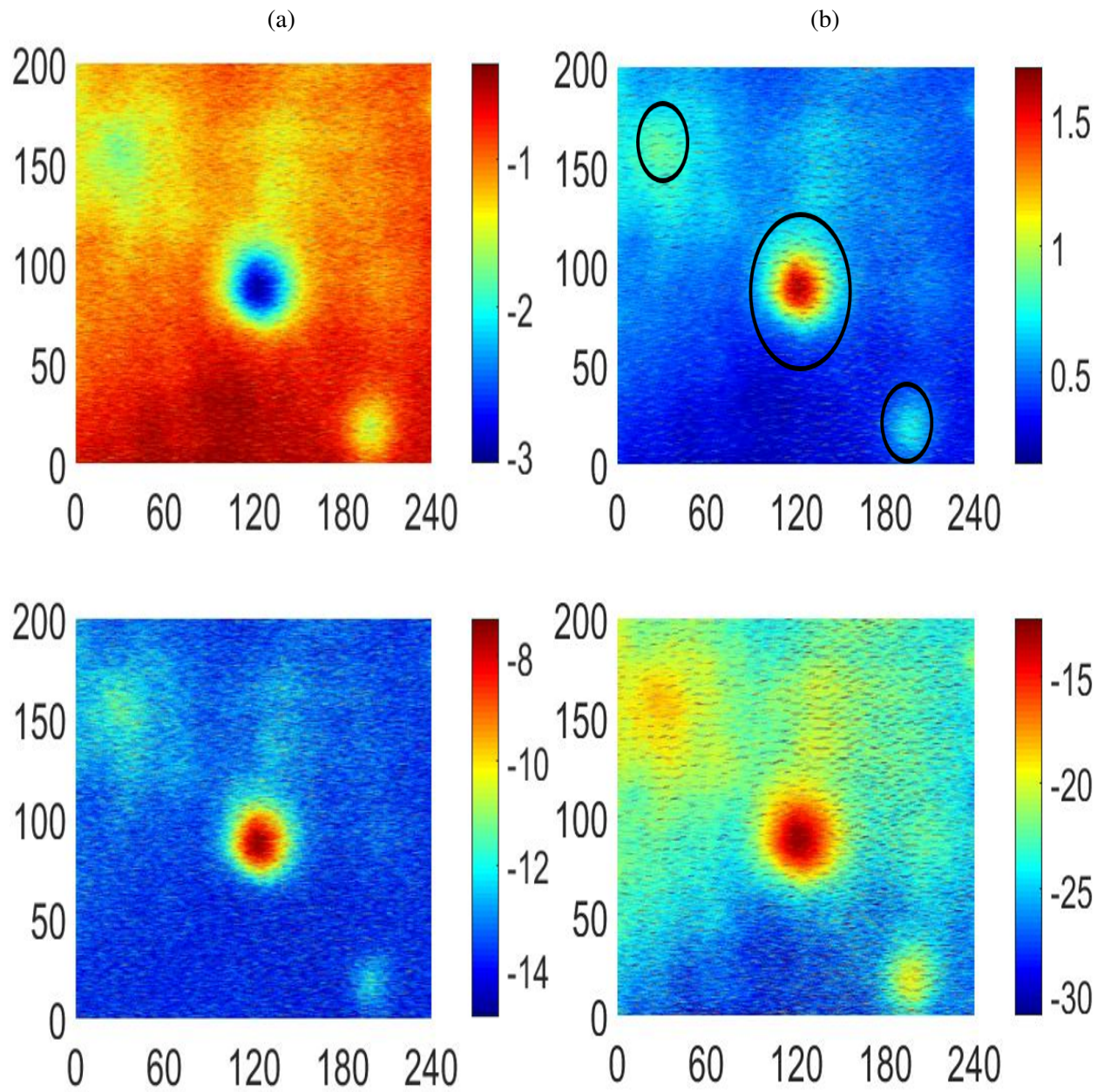


Figure 4.27: Plate 5 results comparison (a) table top system, (b) mini system

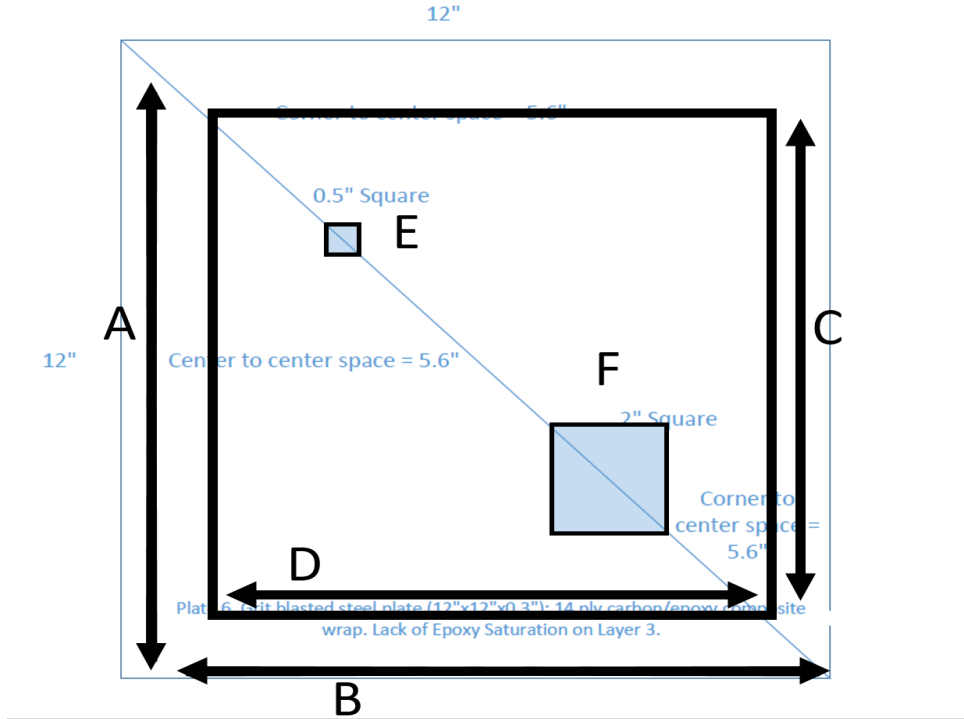


Figure 4.29: Plate 6 Defect Map

Parameter	Dimension	Defect	Detection
A	300mm		
B	300mm		
C	240mm		
D	240mm		
E	12.5mm square	Lack of Epoxy	partial
F	50mm square	Lack of Epoxy	✓

Table 4.7: Plate 6 size, scan, and defect dimension table

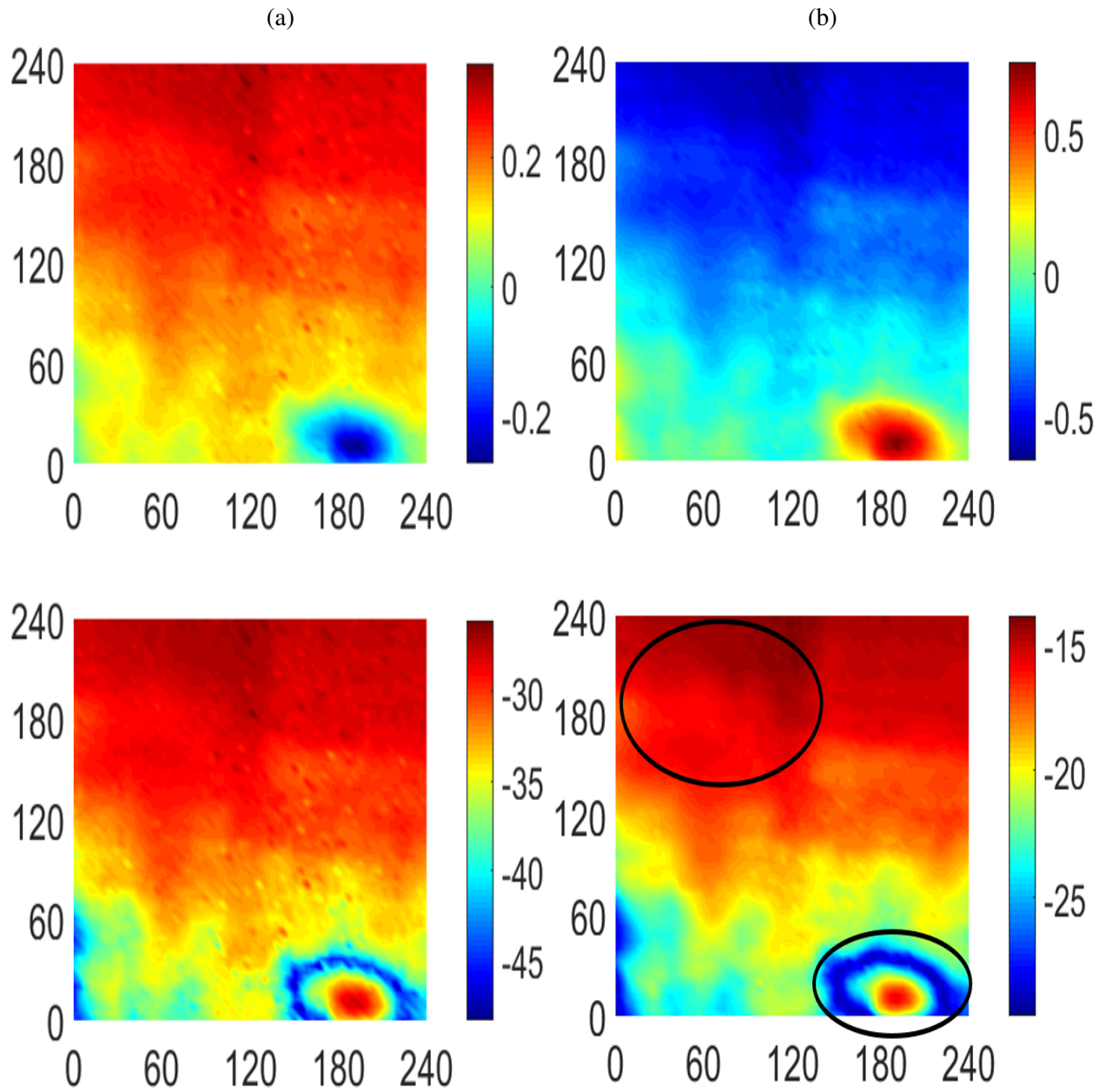


Figure 4.30: Plate 6 results comparison (a) table top system, (b) mini system

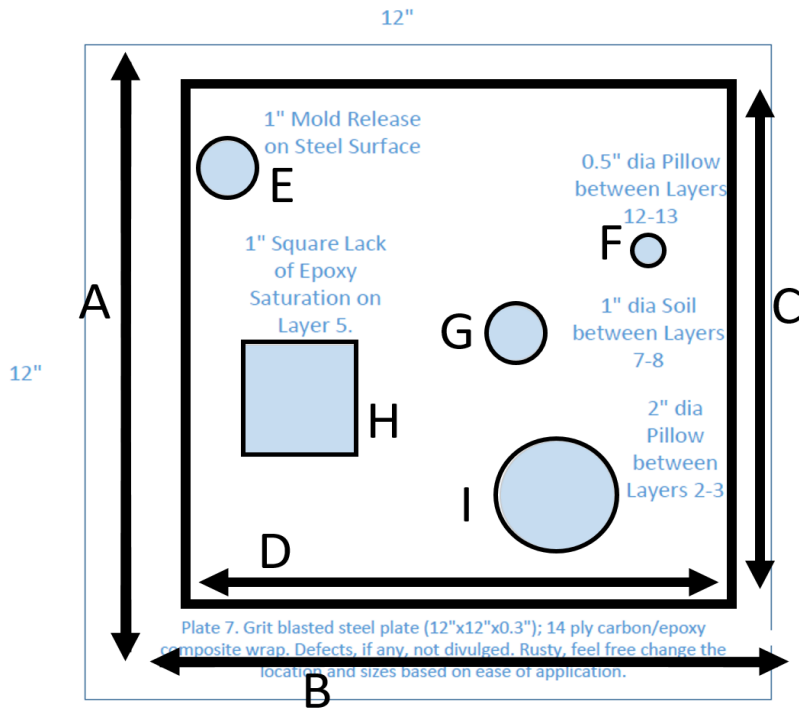


Figure 4.32: Plate 7 Defect Map

Parameter	Dimension	Defect	Detection
A	300mm		
B	300mm		
C	240mm		
D	240mm		
E	25mm dia	Mold	X
F	12.5mm dia	Air	✓
G	25mm dia	Soil contamination	✓
H	25mm square	Lack of epoxy	partial
I	50mm dia	Air	✓

Table 4.8: Plate 7 size, scan, and defect dimension table

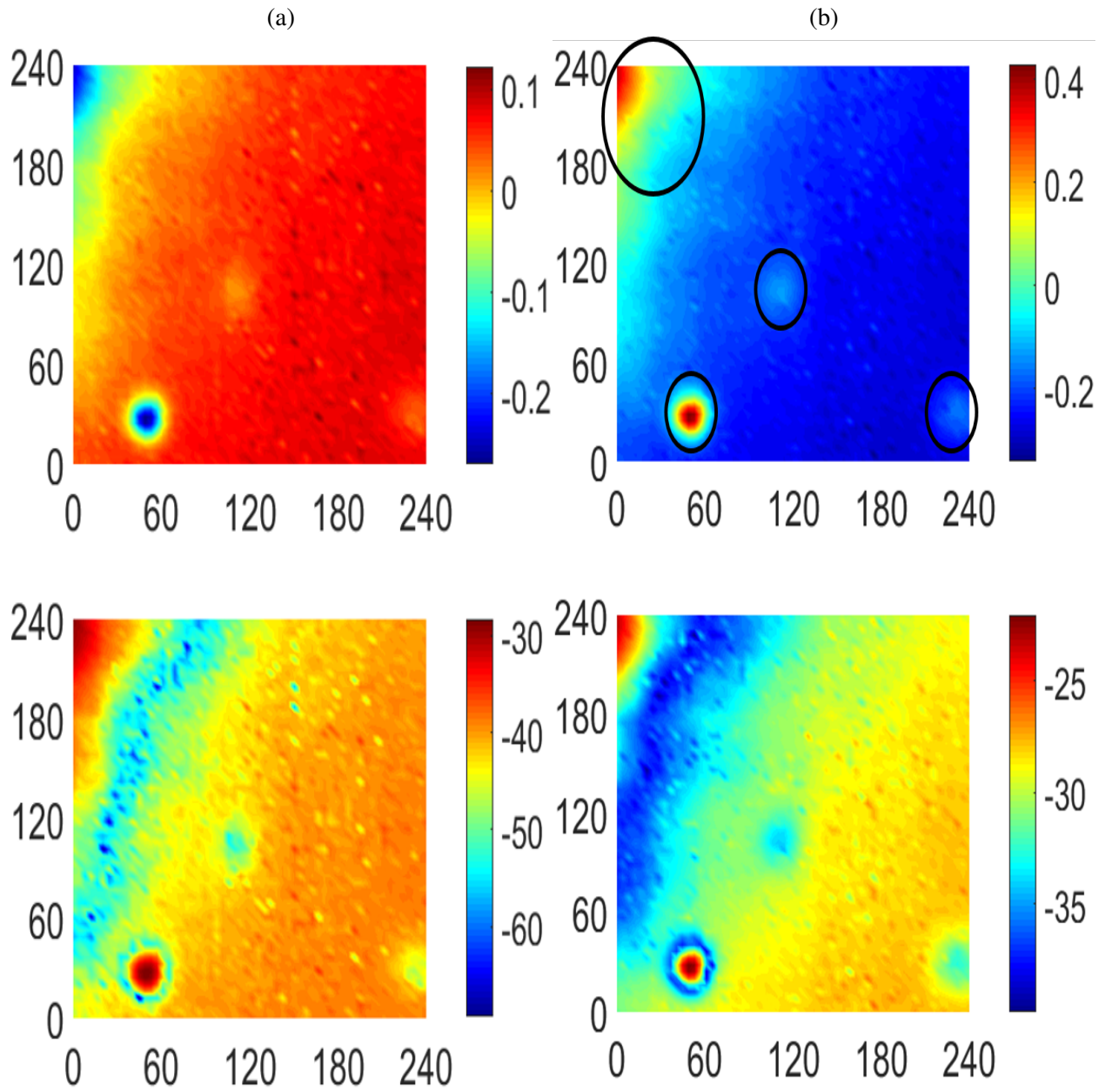


Figure 4.33: Plate 7 results comparison (a) table top system, (b) mini system

## 4.5 Conclusion

The compared results above show that the mini system preforms almost exactly the same as the table top system in all cases, except with slightly increased noise visible in the PE sample results. This could be due to the way that the specific scan was run, and the variation in flatness of the sample itself. The PE scan setup was somewhat unorthodox as can be seen below in figure 4.35.

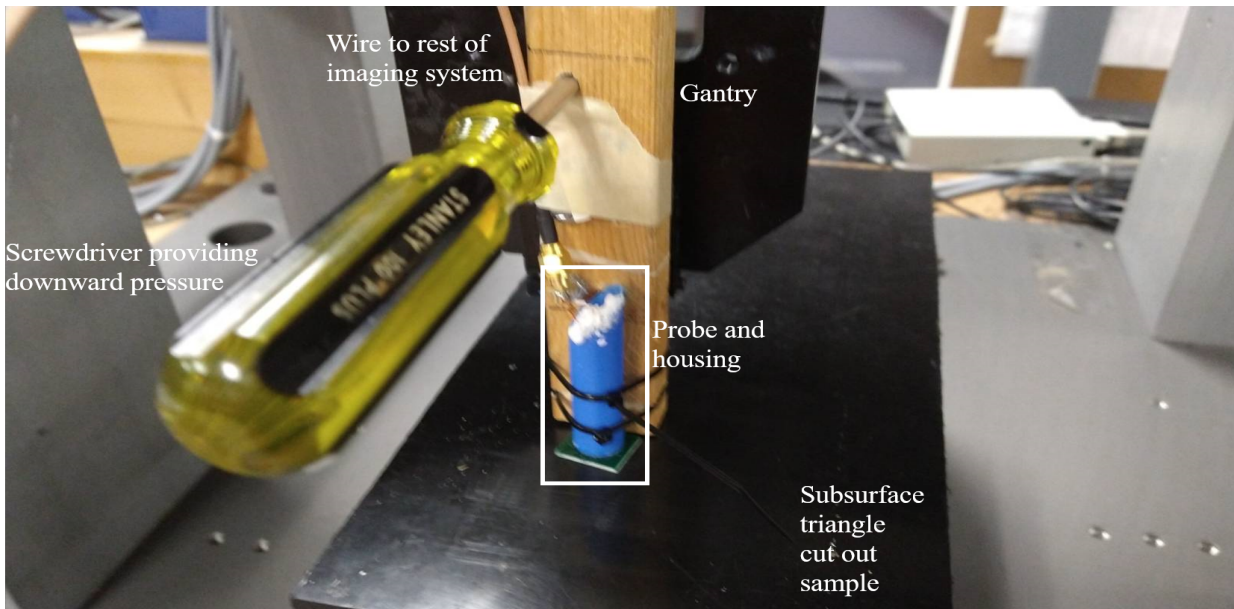
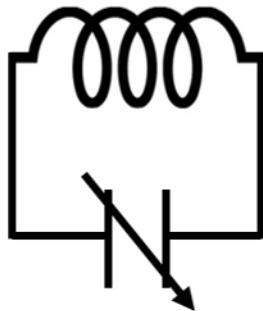
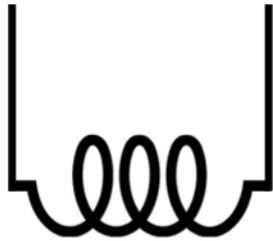


Figure 4.35: PE Sample Probe setup

The probe design itself is based on prior work done in [10] wherein a resonance probe is designed and implemented using LC tank architecture with the equivalent circuit drawing shown below in figure 4.36. The capacitive plate probes shown in figure 4.2 were soldered to an inductor connected across the plates using plated vias through the FR4 board, and a read coil was created by wrapping 20 AWG copper wire around a suitably sized cylinder (ie a pencil) to fit around the soldered inductors. The read coil was then glued to the soldered inductor when an appropriate configuration was found for a sharp resonance peak using a VNA to scan the desired frequency range. The wires connecting the read coil to the SMA connector were intentionally left long, due to the dielectric nature of glue. Manufacturers will claim that the effect of the glue is low or immaterial, but experimental results when fabricating the probes proved this to be wrong, as the

### Wire connections to SMA, (Long wires)



Capacitive plate  
Variable change  
from induced  $\epsilon$

Figure 4.36: Probe equivalent circuit

first edition probes with shorter wires lost a lot of Q after the glue dried. The next iteration of probe included longer wires that could be manipulated by reducing or increasing their separation after the glue was fully dried. This allowed for mitigation of any dielectric effects of the glue. The disadvantage was that the wires were no longer fixed, and various glues and epoxies had proven to be too dielectric for this job. After testing with various materials to fix the wires in place, a PE pipe was purchased and cut into segments, and glued to the FR4 board such that neither the pipe nor the glue had a noticeable effect on the response of the sensor, to protect the wires and provide a housing for them. Common household insulation foam was also purchased and used as a material to fill the housing as it was capable of securing the wires in place and had dielectric properties much closer

to air than the glue did. This allowed for the Q of the sensors to remain after introducing dielectric glue in between the soldered inductor and read coil. The probe setup shown in 4.35 is a result of the glue holding the housing to the FR4 board disbonding; the wires and coil were stationary, but the plate itself was not entirely fixed. A screw driver was placed to maintain downward pressure onto the capacitive plate. This allowed the plate to conform to the contours of the surface of the PE sample during the table top scan. Super glue was reapplied to the housing to ensure the probe did not break, as the entire resonance circuit fabrication process took anywhere from twelve to twenty four hours to finish completely. By the time the mini system was connected and scanning, the glue had dried fixing the probe and reducing the amount of conforming the probe did to the sample surface. As absurd as the improvised probe setup looks, the measured performance of the probes and acquired results validate the probe design and implementation. The results comparison also highly emphasizes the importance of signal filtration and validates the design and implementation of the low pass filtering circuit in the form of an integrator circuit.

## CHAPTER 5

### MINIATURIZED MICROWAVE IMAGING SYSTEM

#### 5.1 Probe and System Description

The probes used for microwave scanning include a cavity waveguide and a monopole antenna acting as a coaxial cable probe. The mini system aimed to replace the table top RF source, allowing for a portable microwave scanning system. A higher frequency I/Q demodulator was also utilized to allow for back calculation of power and phase from acquired data.

##### 5.1.1 Wave-guide

The X band rectangular waveguide used had several resonance points within the 7-12 GHz range but was utilized in the scans shown below at 7.8 GHz. The waveguide utilized had a lower sensitivity, but much better penetration depth for the resultant scans than the coaxial, which will be explained further on in chapter 6. This will also become very apparent when reviewing the results comparison.

##### 5.1.2 Coaxial probe

The probe used as a coaxial probe is actually a monopole antenna utilizing a rigid wire slotted through a drilled hole in a rogers board that had one side of copper peeled off. An SMA connector was used to connect the probe to the system with the rigid wire soldered to the signal pin of the connector, and the ground pins soldered to the copper backside of the rogers board. The "coaxial" probe was utilized at 4.3GHz, and demonstrated high sensitivity, but low penetration depth.

#### 5.2 System Comparison, Table top and Mini

Calibration scans were performed on the same aluminum sample mentioned in chapter 4, with a higher level of resolution achieved. The mini microwave system did not perform exactly as well as the table top system, due to the massively increased phase noise seen at higher frequencies.

The amount of random frequencies seen on the output of the I/Q demodulator and every single resonance frequency associated with the random frequencies caused scans run using the NI DAQ to appear entirely as noise. As a result, the same low pass filters utilized in the low frequency system were implemented to disastrous results. The importance of hardware noise filtering at higher frequencies is a clear take away from the implementation of the microwave mini system. Due to this filter miscalculation, two digital multi meters were utilized to record both the I and Q components of the acquired data. The increased phase noise at higher frequencies can be seen most clearly in figures 5.4 and 5.5. The first six calibrations samples were run using a single DMM to verify that the system was working correctly, the "coaxial" probe had high sensitivity to small resolution defects, and the waveguide had penetration depth. The figure form as seen in figures 5.4 and 5.5 is ultimately how the data acquired from two DMMS was graphed, with the top two sub-figures being in-phase and quadrature phase respectively, while the bottom two graphs are the back-calculated reflected power and phase. The microwave plate scans further down are minimized for visibility to just the I component and the back-calculated phase, as these two were the most clear results. The PE sample was re-run with the microwave system to verify the penetration depth of the waveguide on subsurface defects, and the results from the monopole scan is not included due to the results being entirely surface profiling.

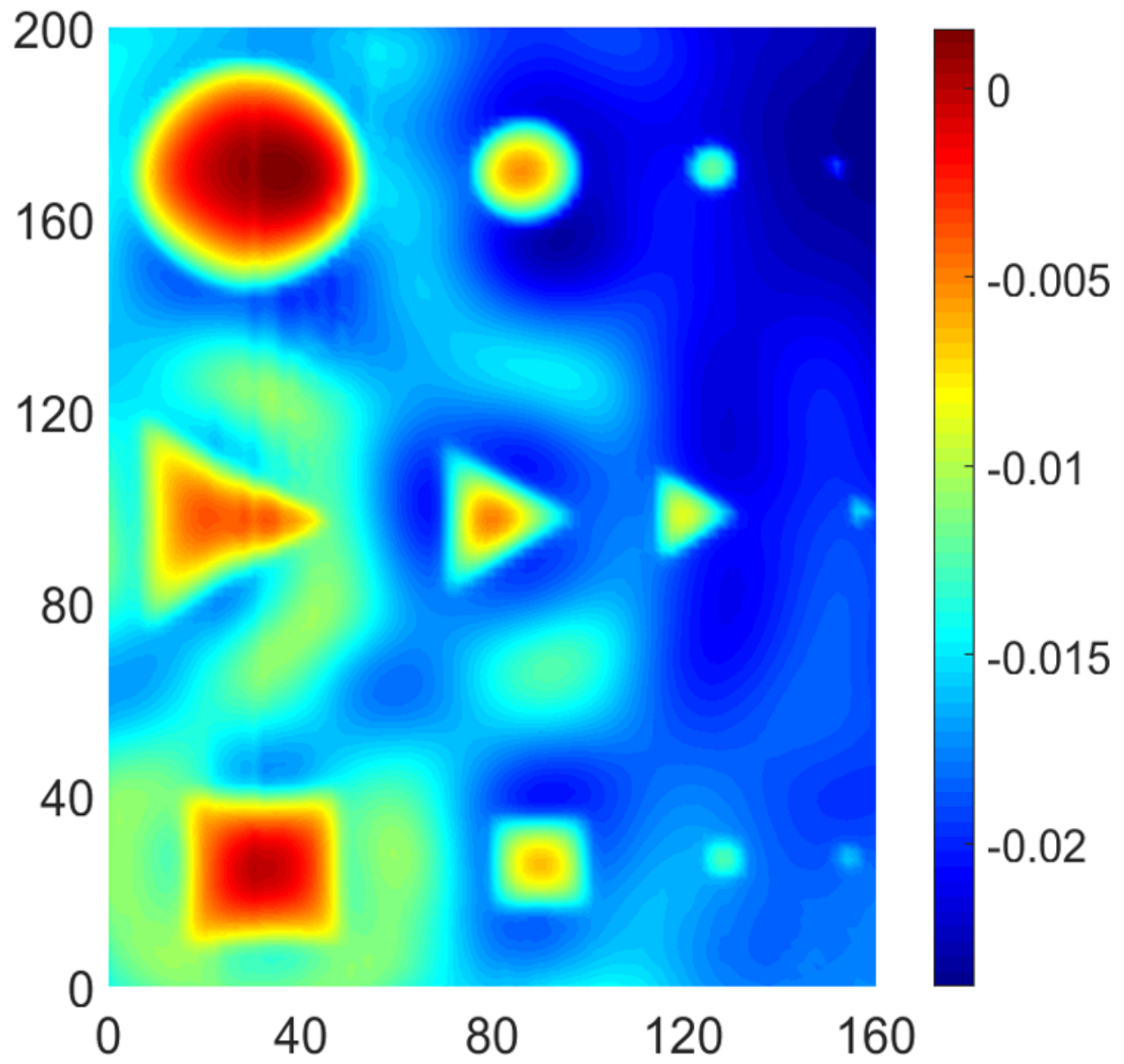


Figure 5.1: Aluminum Calibration sample, table top system (Coax)

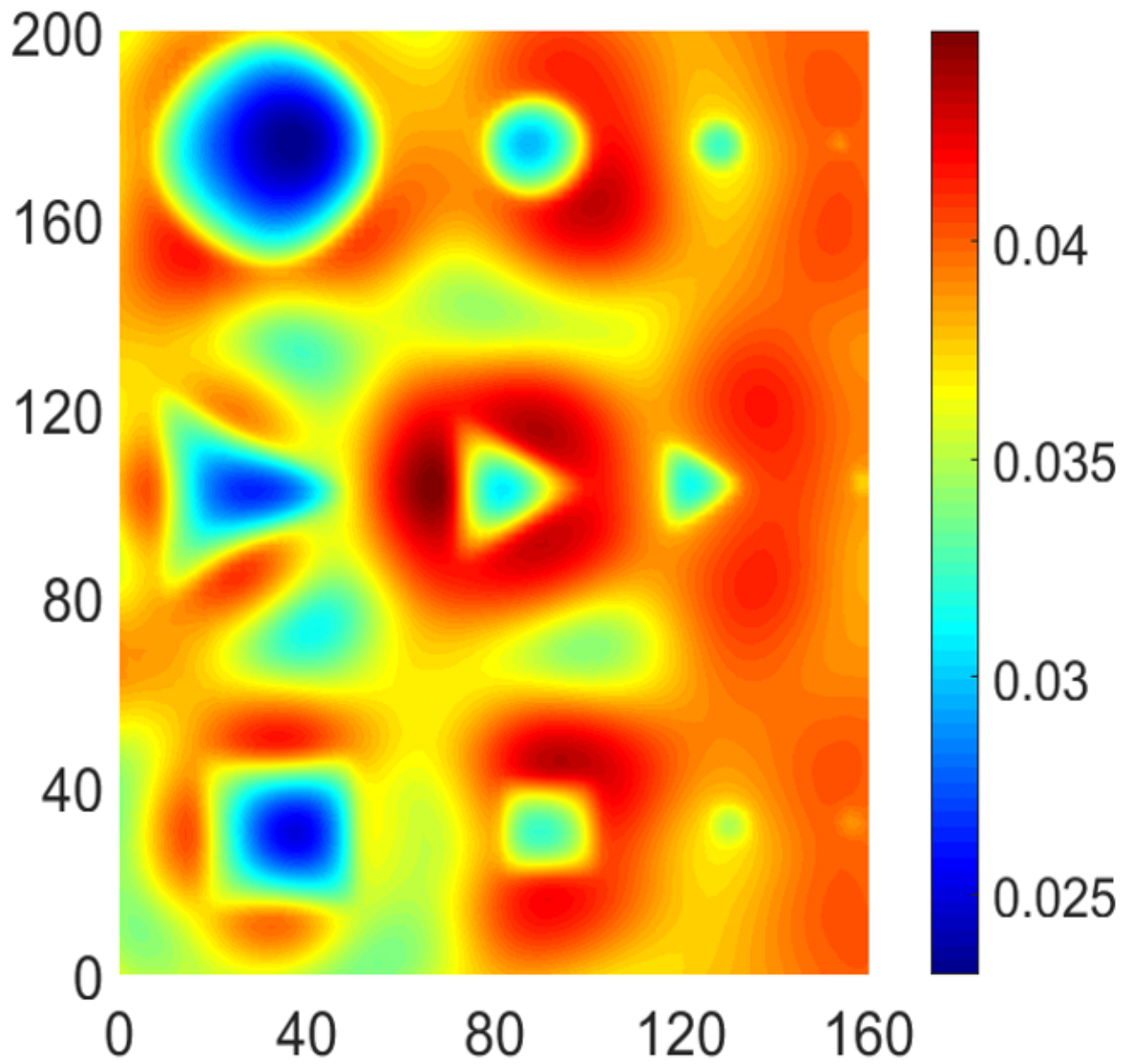


Figure 5.2: Aluminum Calibration sample, mini system scan (Coax)

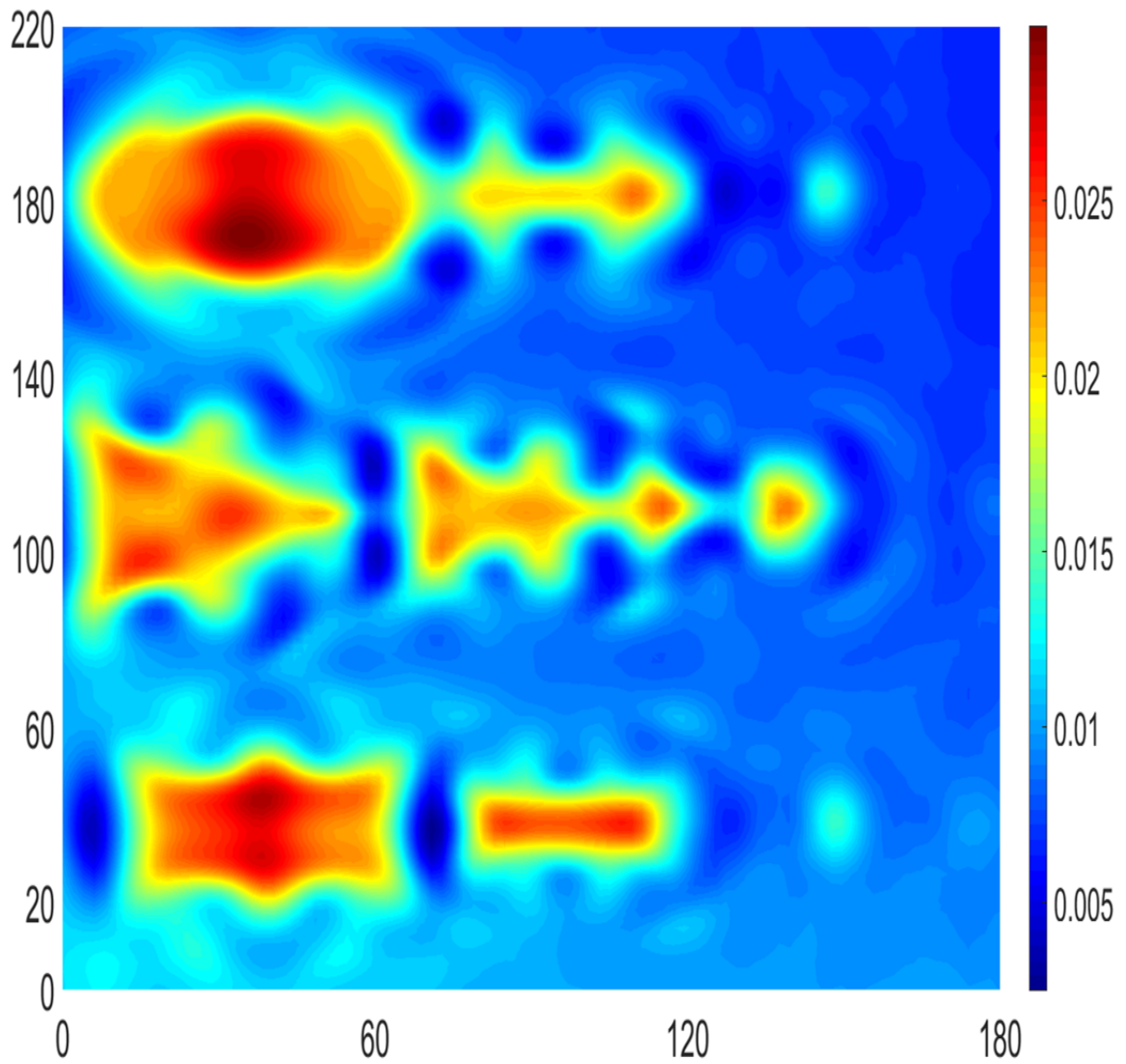


Figure 5.3: Aluminum Calibration sample, table top system (Wave-guide)

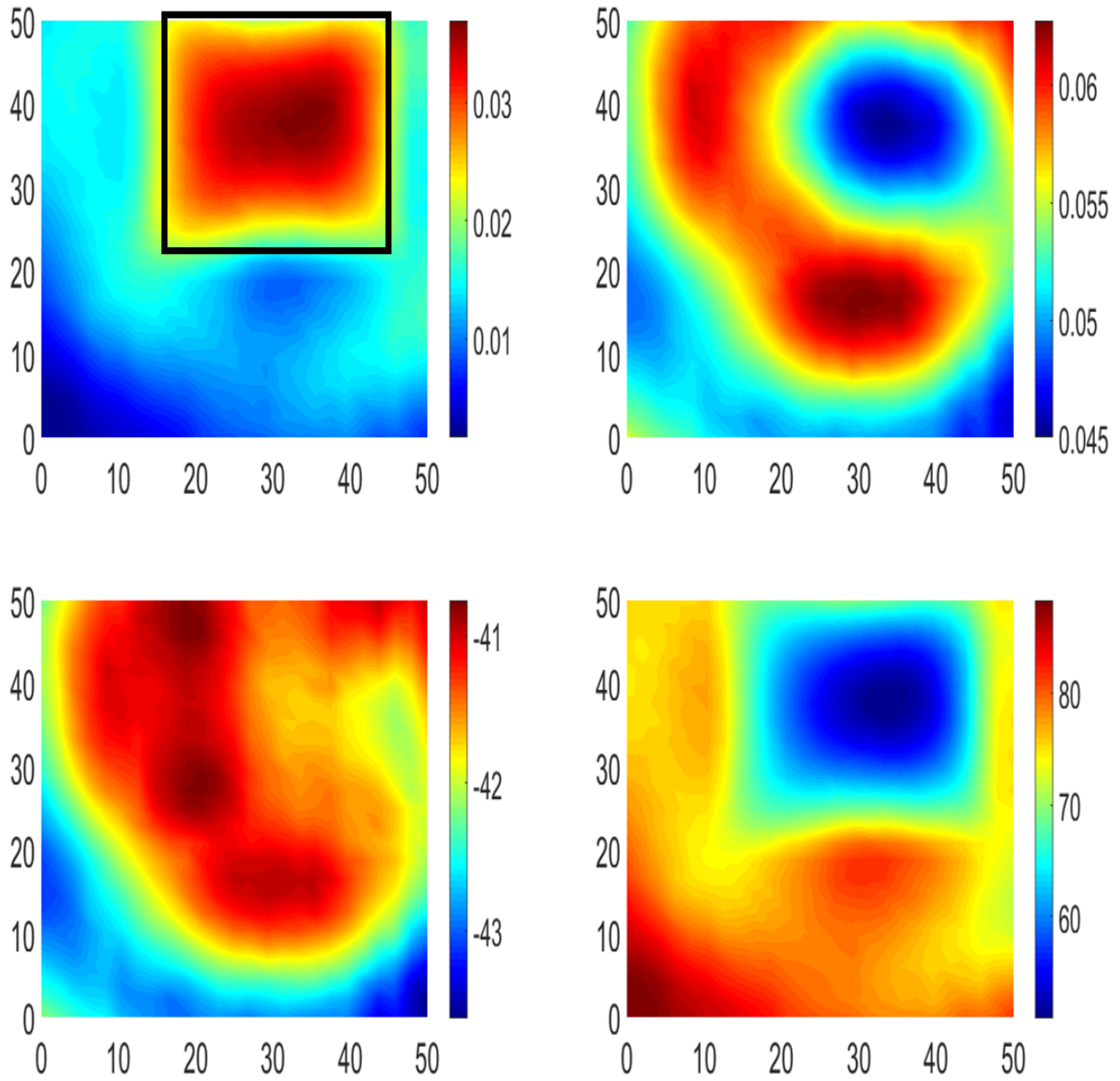


Figure 5.4: Aluminum Calibration sample, first square, mini system (Coax)

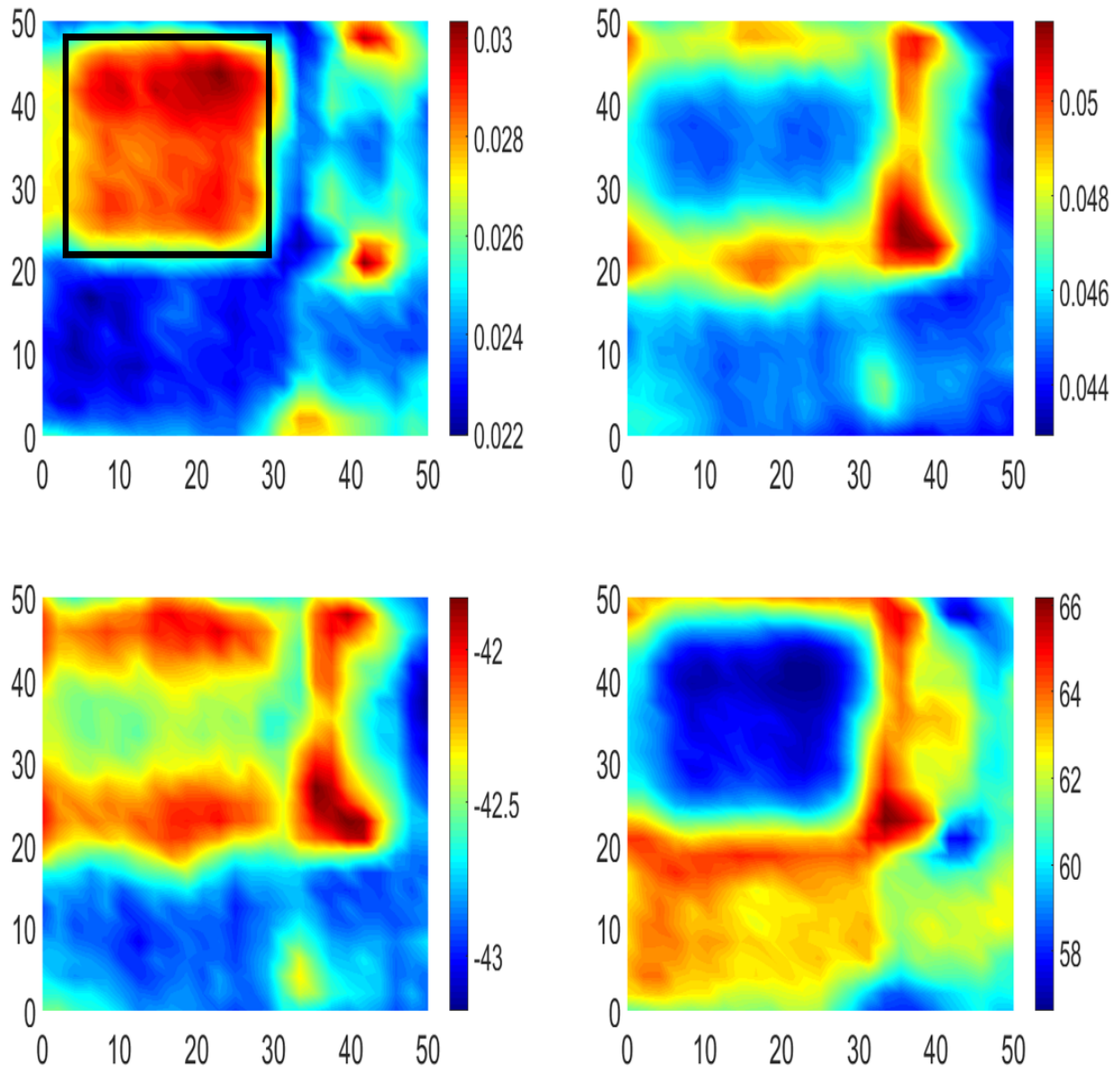


Figure 5.5: Aluminum Calibration sample, first square, mini system (Wave-guide)

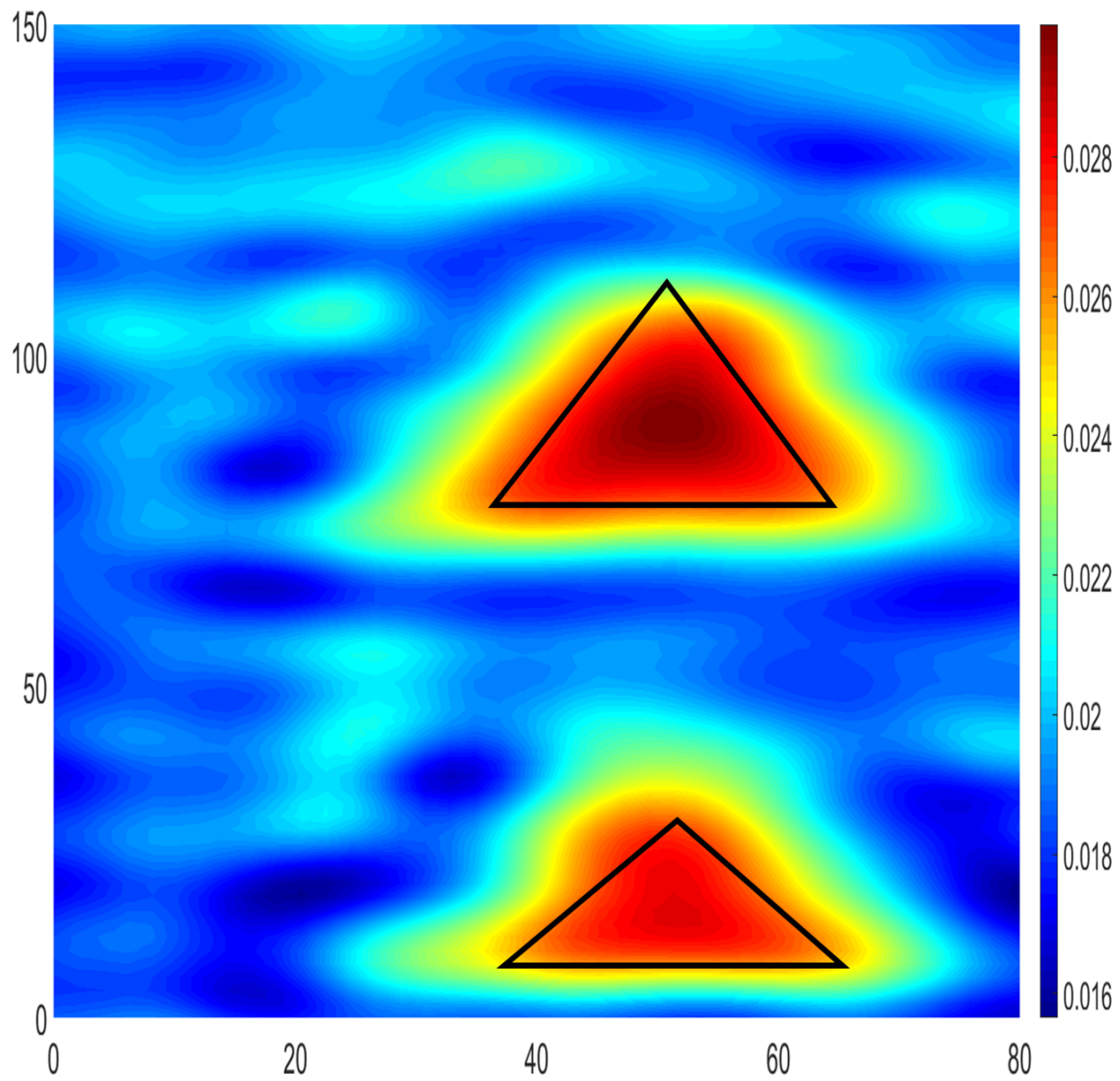


Figure 5.6: Polyethylene, table top system (Wave-guide)

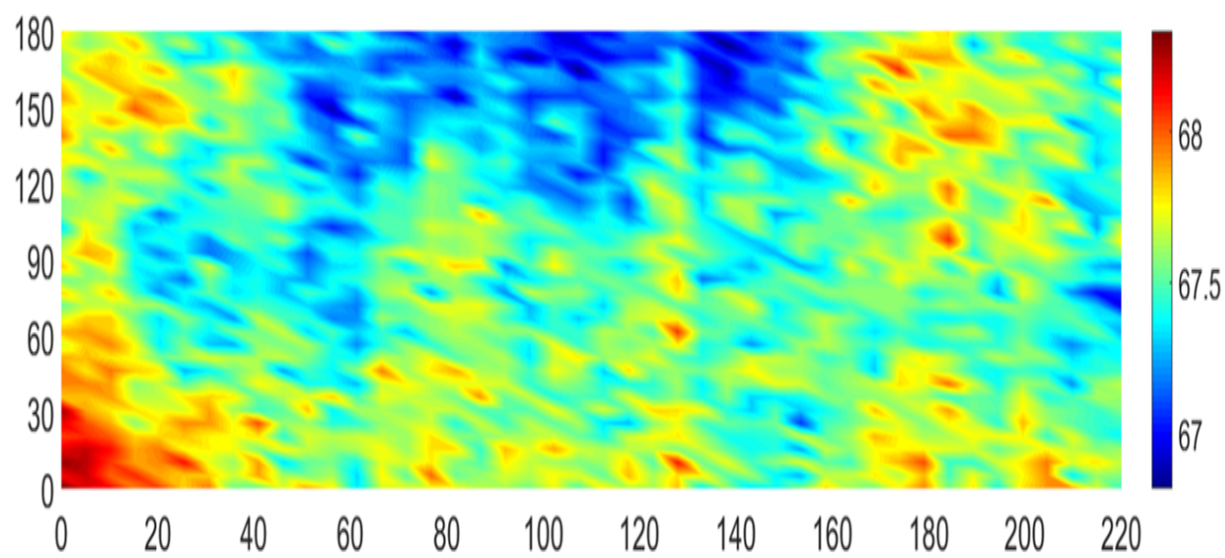
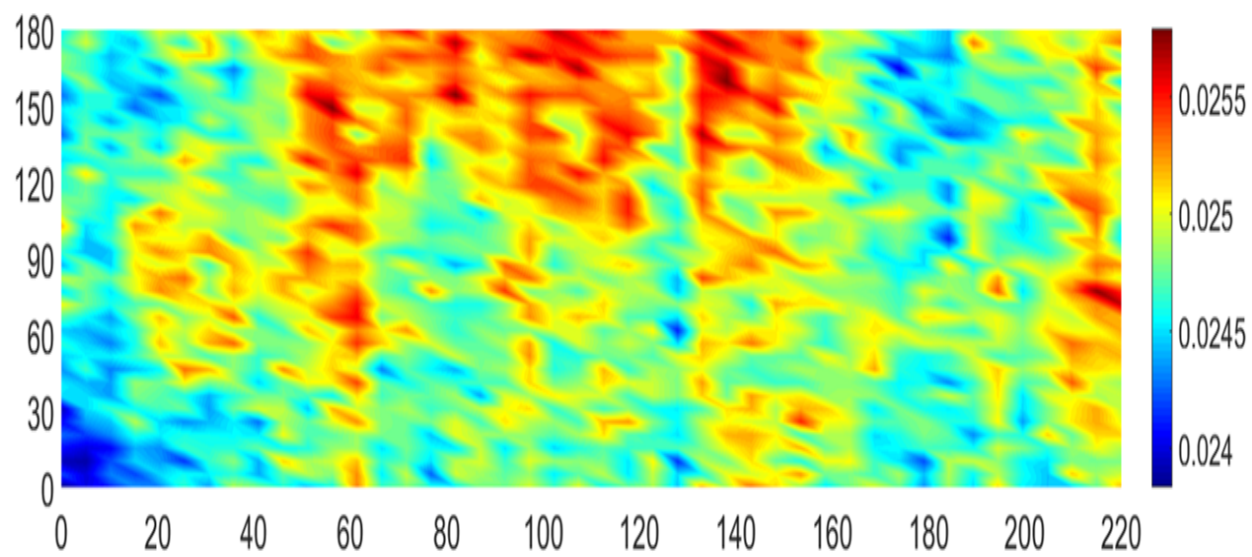


Figure 5.7: CFRP Plate 1, Wave-guide, mini system

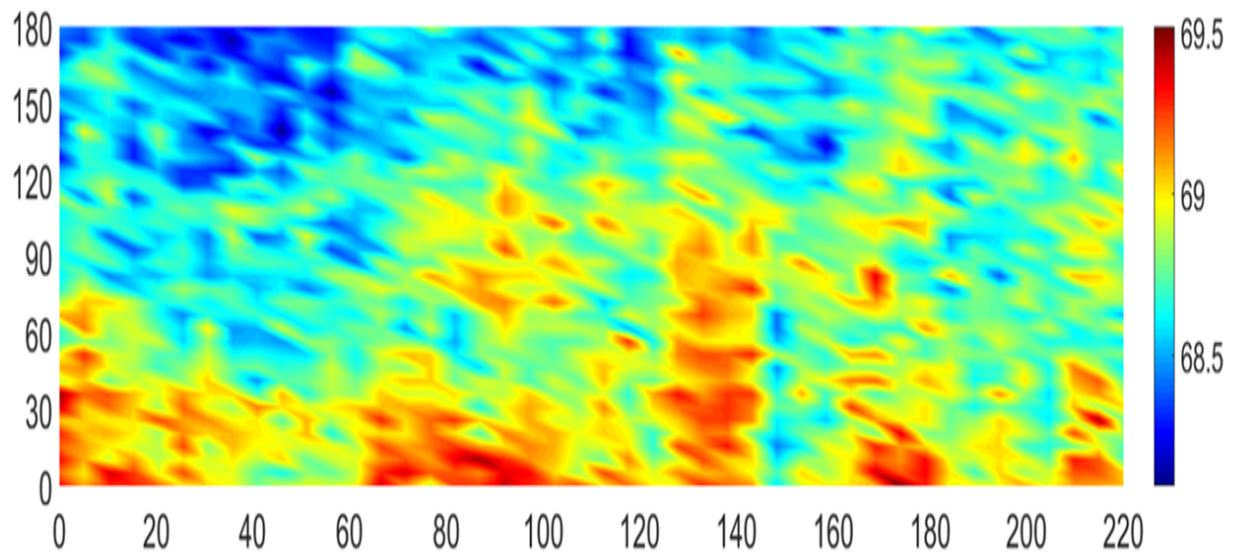
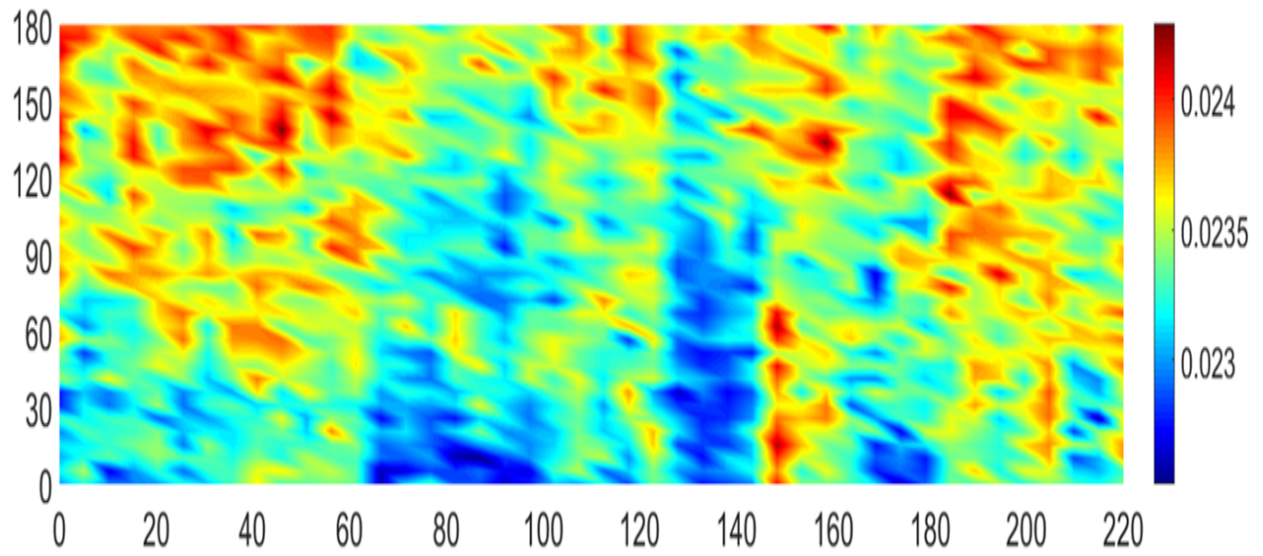


Figure 5.8: CFRP Plate 2, Wave-guide, mini system

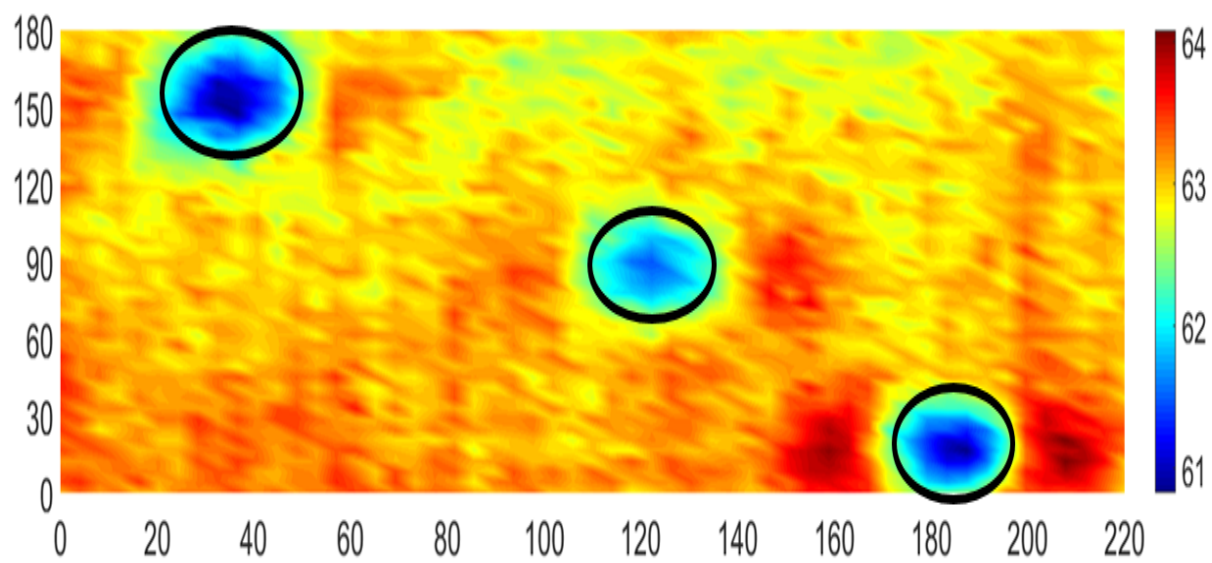
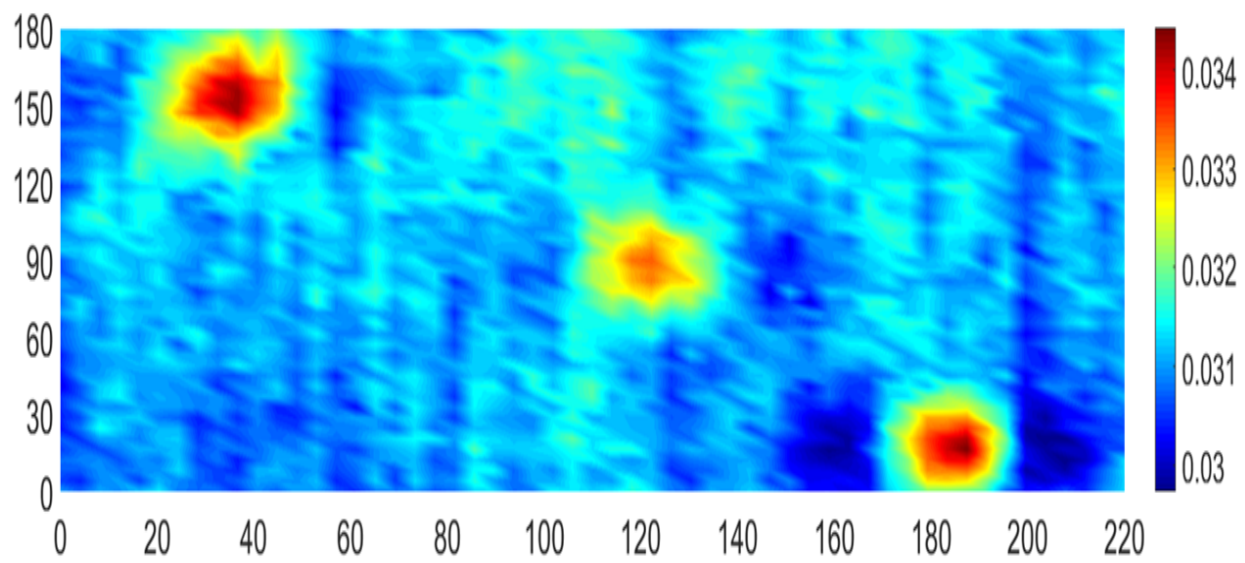


Figure 5.9: CFRP Plate 4, Wave-guide, mini system

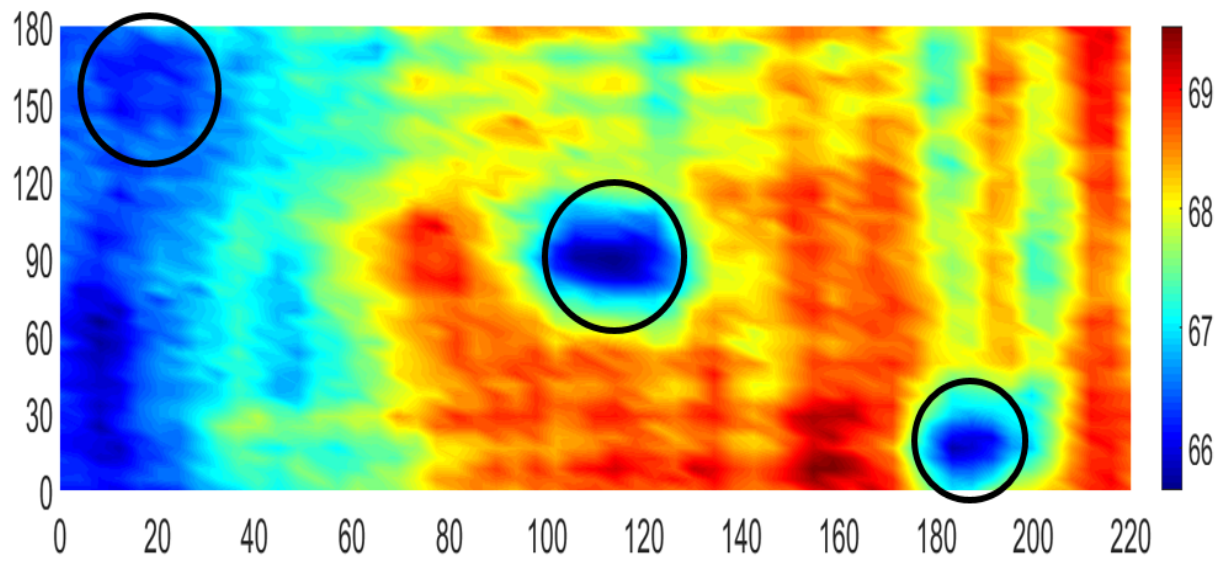
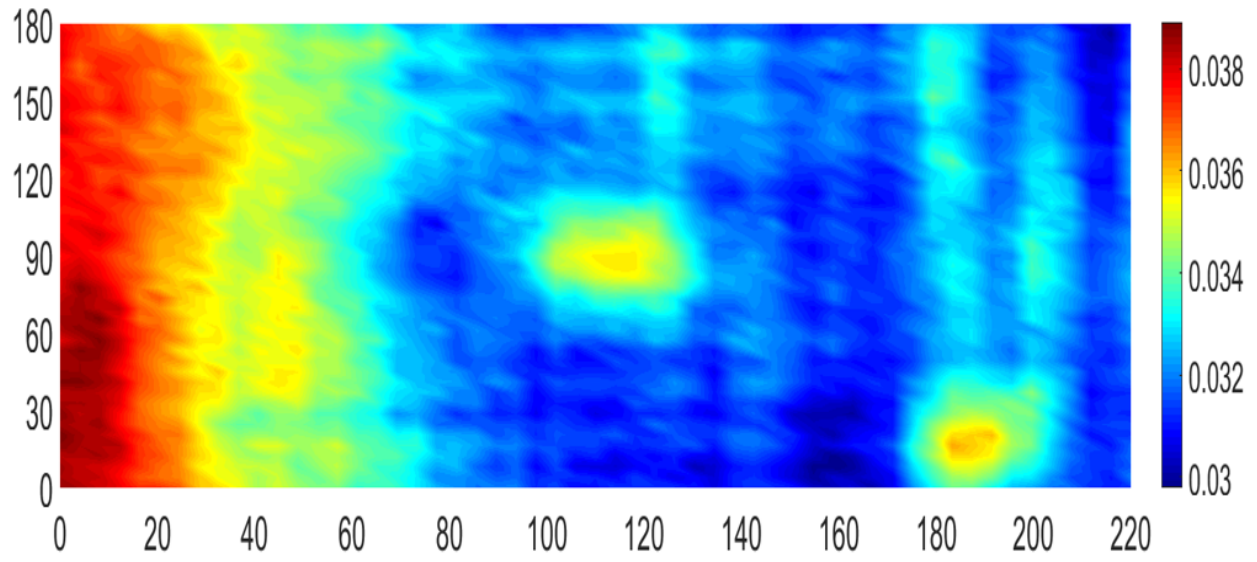


Figure 5.10: CFRP Plate 5, Wave-guide, mini system

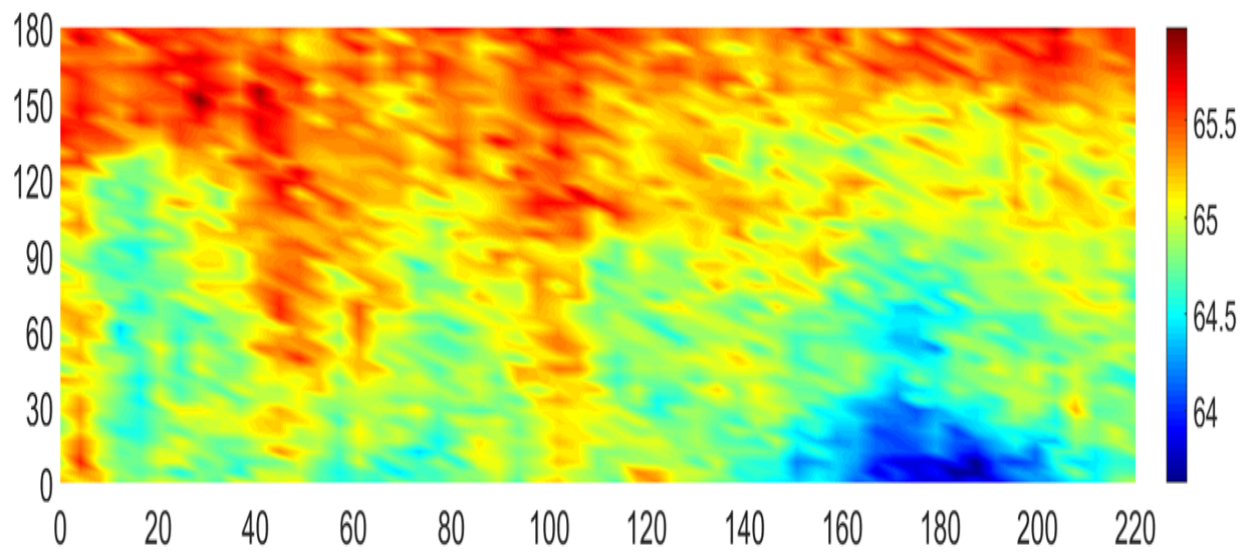
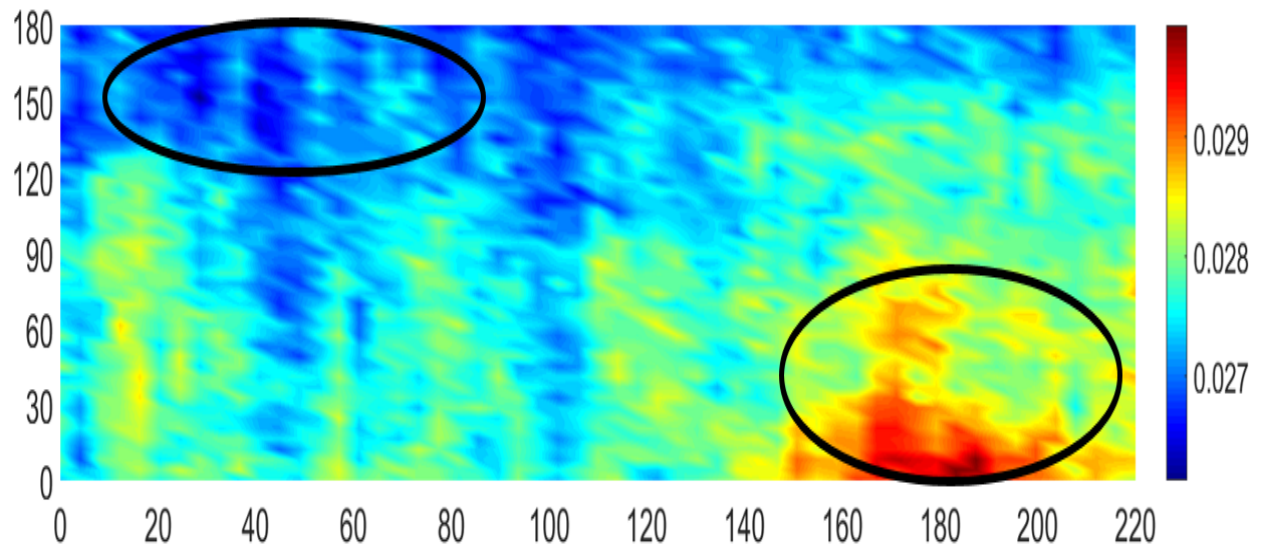


Figure 5.11: CFRP Plate 6, Wave-guide, mini system

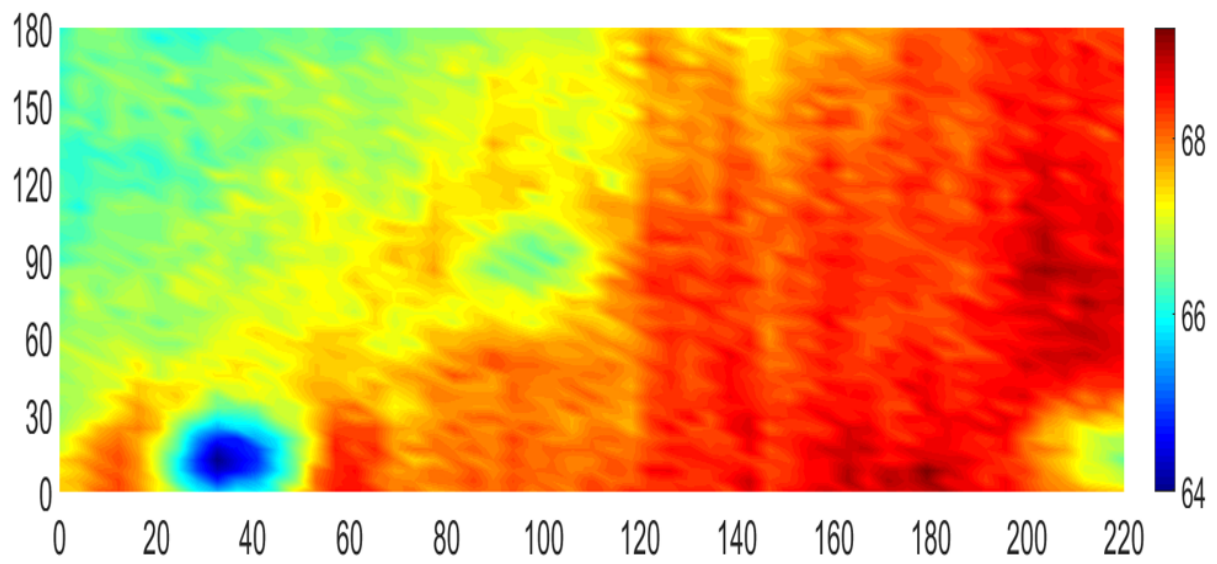
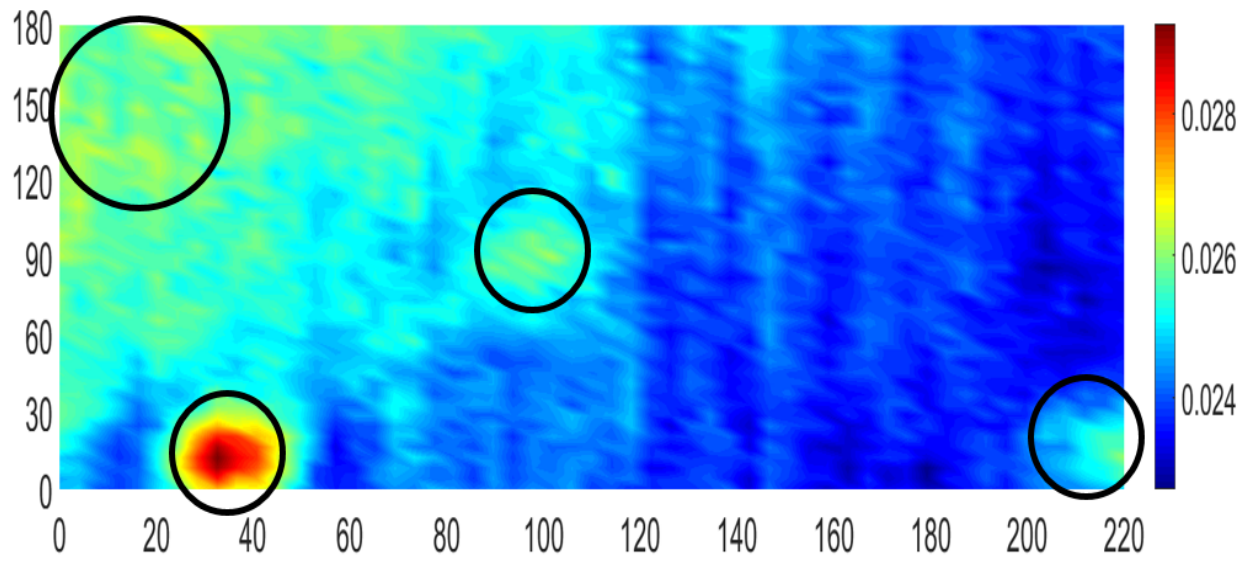


Figure 5.12: CFRP Plate 7, Wave-guide, mini system

### **5.3 Conclusion**

The results acquired using the mini microwave system, while noisy, still match the results acquired from the capacitive mini system with both systems only utilizing hardware noise filtration. Even with the waveguide calibration sample results as they are in figure 5.3, the results from the plate scans clearly match, with some defects, like those shown in plate 7 (figure 5.12) becoming more apparent. This consistency validates the results obtained in chapter 4, and demonstrates the need for multi system integration, as even though both systems rely inherently upon dielectric sensitivity, the penetration depth of the microwave scans makes up for its lack of resolution. This will be discussed more in the next chapter.

### **5.4 Importance of System Integration**

Each system has its own strengths and weaknesses. The capacitive imaging system penetration depth and signal filtration can be clearly seen from the table top and mini system comparisons, while it falls short a little in resolution size for smaller defects. The microwave system contrasts this perfectly, where the penetration depth for highly sensitive probes is nearly inconsequential, as the PE subsurface defect scan performed with the coax cable wasn't even worth including. The waveguide is a sort of middle ground that does both jobs poorly, but is at least helpful for validating the previous scans and verifying the consistency of both systems. The low frequency system's weakness is the high frequency system's strength, and vice versa. Integrating both systems with interchangeable probe types would allow efficient dielectric evaluation of composites. The systems complement each other, and thus the integration of them would create, overall, a much better system, while still retaining the qualities targeted by the multi modality system. Both systems when integrated would not only be relatively cheap, in comparison to the available methods, but carry the capability of field deployment, all while staying compact. Due to the nature of the boards used within both systems, the entire integrated system could be fixed into a box with output ports for their respective probes, and input ports for power and connection to a processing unit allowing for imaging of dielectric materials with both low frequency capacitive, and high frequency microwave

methods.

#### **5.4.1 Edge detection vs penetration**

The coaxial probe is the top choice for high resolution surface scans, while the waveguide loses the edge detection and resolution, it has increased penetration depth, though even then the clarity of some of the defects that were clearly imaged using capacitive imaging was unparalleled. The low frequency resonance probes have not only the penetration depth, but very good edge detection for any surface defects larger than sub-mm. This can be improved upon in the future by optimizing the low pass filters in the capacitive system more, or by re-fabricating the capacitive resonance probes with smaller feature sizes.

### **5.5 Low and High frequency system comparisons**

The most notable comparison between the low and high frequency system results is the difference between the resolution in the aluminum calibration sample, with the capacitive results shown in figures 4.12b and 4.12a with the smallest defect size being barely visible or unable to be seen entirely. When the smallest defect is detected, the shape is impossible to make out, the only conclusion without knowing the defect is actually there is that there is a good chance that it is a defect and not just noise. This is in sharp contrast to the resolution demonstrated by the coaxial probe shown in figure 5.1 with all three defects in the final row easily visible and the distinct shape of a triangle clearly shown. The wave guide edge detection is unsurprisingly poor, as can be seen in figure 5.3. The problem with the sensitivity in higher frequency imaging probes is that the signal penetration depth is much less than lower frequencies. The resolution of surface detection, however is much greater.

## CHAPTER 6

### CONCLUSIONS AND FUTURE WORK

#### 6.1 Importance of System Integration

Each system has its own strengths and weaknesses. The capacitive imaging system penetration depth and signal filtration can be clearly seen from the table top and mini system comparisons, while it falls short a little in resolution size for smaller defects. The microwave system contrasts this perfectly, where the penetration depth for highly sensitive probes is nearly inconsequential, as the PE subsurface defect scan performed with the coax cable wasn't even worth including. The waveguide is a sort of middle ground that does both jobs poorly, but is at least helpful for validating the previous scans and verifying the consistency of both systems. The low frequency system's weakness is the high frequency system's strength, and vice versa. Integrating both systems with interchangeable probe types would allow efficient dielectric evaluation of composites. The systems complement each other, and thus the integration of them would create, overall, a much better system, while still retaining the qualities targeted by the multi modality system. Both systems when integrated would not only be relatively cheap, in comparison to the available methods, but carry the capability of field deployment, all while staying compact. Due to the nature of the PCB and components used within both systems, all could be stacked to reduce the space they take up, and the entire integrated system could be fixed into a box with output ports for their respective probes, and input ports for power and connection to a processing unit allowing for imaging of dielectric materials with both low frequency capacitive, and high frequency microwave methods.

##### 6.1.1 Edge detection vs penetration

The coaxial probe is the top choice for high resolution surface scans, while the waveguide loses the edge detection and resolution, it has increased penetration depth, though even then the clarity of some of the defects that were clearly imaged using capacitive imaging was unparalleled. The low

frequency resonance probes have not only the penetration depth, but very good edge detection for any surface defects larger than sub-mm. This can be improved upon in the future by optimizing the low pass filters in the capacitive system more, or by re-fabricating the capacitive resonance probes with smaller feature sizes.

### **6.1.2 Low and High frequency system comparisons**

The most notable comparison between the low and high frequency system results is the difference between the resolution in the aluminum calibration sample, with the capacitive results shown in figures 4.12b and 4.12a with the smallest defect size being barely visible or unable to be seen entirely. When the smallest defect is detected, the shape is impossible to make out, the only conclusion without knowing the defect is actually there is that there is a good chance that it is a defect and not just noise. This is in sharp contrast to the resolution demonstrated by the coaxial probe shown in figure 5.1 with all three defects in the final row easily visible and the distinct shape of a triangle clearly shown. The wave guide edge detection is unsurprisingly poor, as can be seen in figure 5.3. The problem with the sensitivity in higher frequency imaging probes is that the signal penetration depth is much less than lower frequencies. The resolution of surface detection, however is much greater.

## **6.2 Conclusions**

In this paper, several methods of defect classification and characterization are discussed from an NDE perspective. A gap in the frequency band was identified and capitalized on, allowing for efficient dielectric evaluation of composite materials utilizing high Q LC tank resonance probes created for use with the system. The governing theory for both low frequency capacitive scanning and high frequency microwave scanning has been thoroughly detailed to explain the design and implementation process of the creation of the system. The miniaturized system has been shown to produce equivalent results to bulky, expensive, table top equipment, while maintaining a low cost, compact size, and the capability for field deployment.

### **6.3 Future work**

Improvements can be made to the system by utilizing the specific integrated circuits from the evaluation boards for the low and high frequency sources, as well as their associated I/Q demodulator source boards. This would further miniaturize the system and ultimately lower the overall cost. The low pass filter integrators can be improved so that the cut-off frequency is even lower, filtering as much higher frequency phase noise and harmonics as possible, allowing microwave data acquisition with the NI DAQ or with the ADC, which would decrease the microwave scan time substantially and allow for both amplitude and phase to be acquired simultaneously. Modifications can be made to the system housing allowing for a more robust field deployment in the future.

## **APPENDICES**

## **APPENDIX A**

### **DIELECTRIC LENS**

The high gain antenna requirement for imaging and communication application has historically evolved the antenna design. Today, the commonly known high gain antennas are vivaldi, yagi-uda, horn, and wave-guides, all of which have an excellent gain performance but with the trade-off of having a high profile [39,40]. The only design with a relatively higher gain and a low profile is the patch antenna. In this paper, the authors have explored a way to increase the gain of patch antenna using a dielectric RF lens, while keeping a lower profile than any available high gain antenna.

Lenses are classical tools that have been used for centuries in the field of optics. The lenses are well known for their focusing, collimating, and diffraction properties. The same principle have been applied for lower frequency waves, in order to decrease the beamwidth and increased gain. A number of designs operating at range of frequencies with different shapes and applications have been previously published in the literature. The primary focus of most of the papers are characteristics for high gain, low profile, and beam steering capabilities, allowing for improvement in imaging and communication systems [41–44].

While dielectric lenses are a great tool, in the past they were often difficult to implement due to the response being dictated by how precisely the geometry could be manufactured to fit the design specifications. Besides that, before quite recently, high fidelity simulation softwares for high frequency applications did not exist, making the design of dielectric lenses very difficult, due to the inability to account for changes in the system due to manufacturing errors.

Because of recent breakthroughs in simulation software, and more importantly, manufacturing techniques like 3D printing, the design, fabrication, and implementation of RF components has become much more economical, and easier, allowing for planar antenna excitation in the C-band.

This paper shows a design of dielectric lens and patch antenna in ANSYS High Frequency Structure Simulator (HFSS), fabrication of the lens using additive manufacturing technique, and measurement of the patch antenna gain with and without the dielectric lens.

Dielectric lenses affect electromagnetic waves similarly to how optical lenses affect light, and are known for their uses as an electromagnetic beam collimator, as they allow for focusing of the waves propagated from a source, in this case an antenna. [41] This effect is illustrated in Fig.A.1,

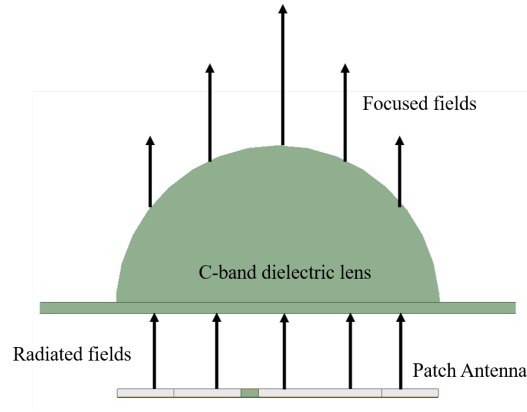


Figure A.1: Focusing of RF waves radiated from patch antenna using dielectric lens

[42] shows that a lens can be a hemispherical due to the wave symmetry.

The VeroWhite material with a dielectric permittivity of 2.8 is used to design the lens in ANSYS HFSS. In order to mount the lens over a patch antenna operating in C band (5.3 GHz) with the ground plane of size 50 mm x 50 mm, the lens's diameter is selected to be 60 mm. The designed lens and patch antenna with dimensions is shown in Fig.A.2.

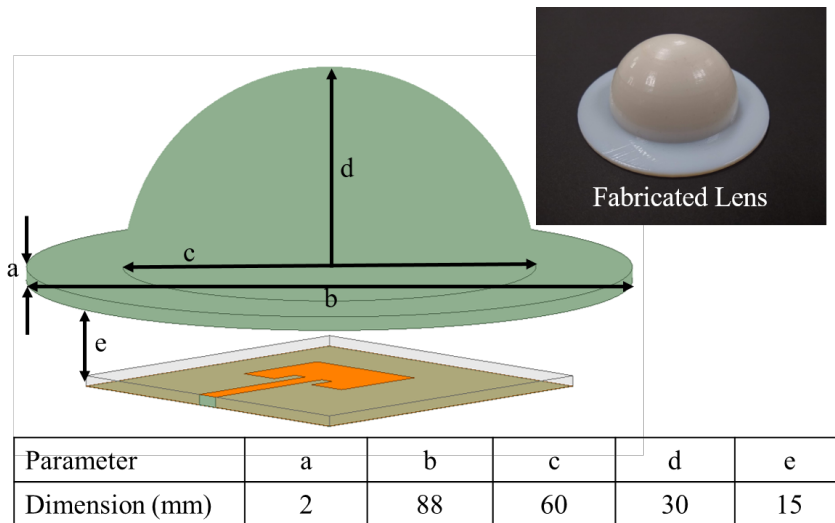


Figure A.2: Designed and fabricated lens with the dimensions

The Stratasys's CONNEX3 OBJET350 3D printer is used to fabricate the lens and CNC milling machine is used to fabricate the patch antenna on Rogers's 4350 substrate (thickness = 1.52 mm, dielectric = 3.66, loss tangent = 0.003).

The designed patch antenna at 5.3 GHz is fabricated, and its gain is measured using Satimo's antenna measurement system. The simulated and measured gain are shown in Fig.A.3. The measured gain pattern matches the simulated gain pattern, and the highest measured gain in normal direction is 5.9 dBi. The measured 3 dB beamwidth for the patch is 76°.

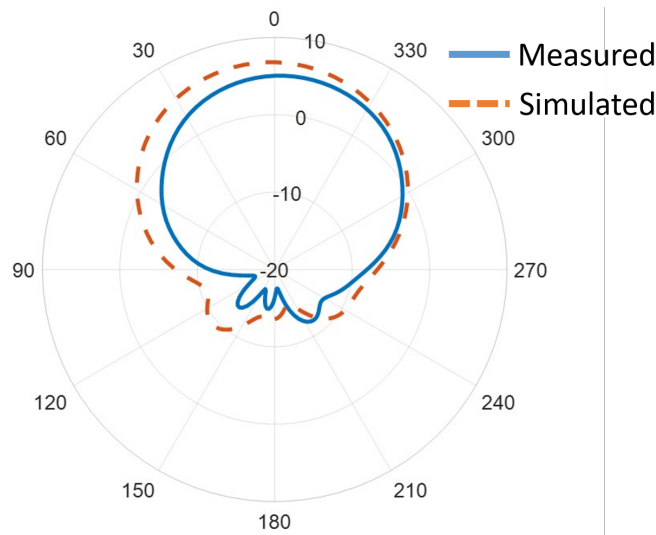


Figure A.3: Simulated and Measured gain of the patch antenna at 5.3 GHz without lens

Next, a lens is mounted on top of the patch antenna. A 15 mm separation is given in between lens and antenna to eliminate the direct dielectric loading issues. The patch gain is measured again with the dielectric lens and the measured results are shown in Fig.A.4.

The shown simulated and measured results match closely. The highest measured gain in the normal direction is 9.4 dBi, which has enhanced the normal patch antenna gain by 3.5 dBi. The 3 dB beamwidth for the patch is reduced from 76° to 43°.

Additionally, the dielectric lens is simulated from 4 GHz to 10 GHz in ANSYS HFSS, where it performs similarly at all frequencies, ideal for C-band operations. This dielectric lens could be used in tandem with the microwave probe designed for this project allowing for greater detection capabilities.

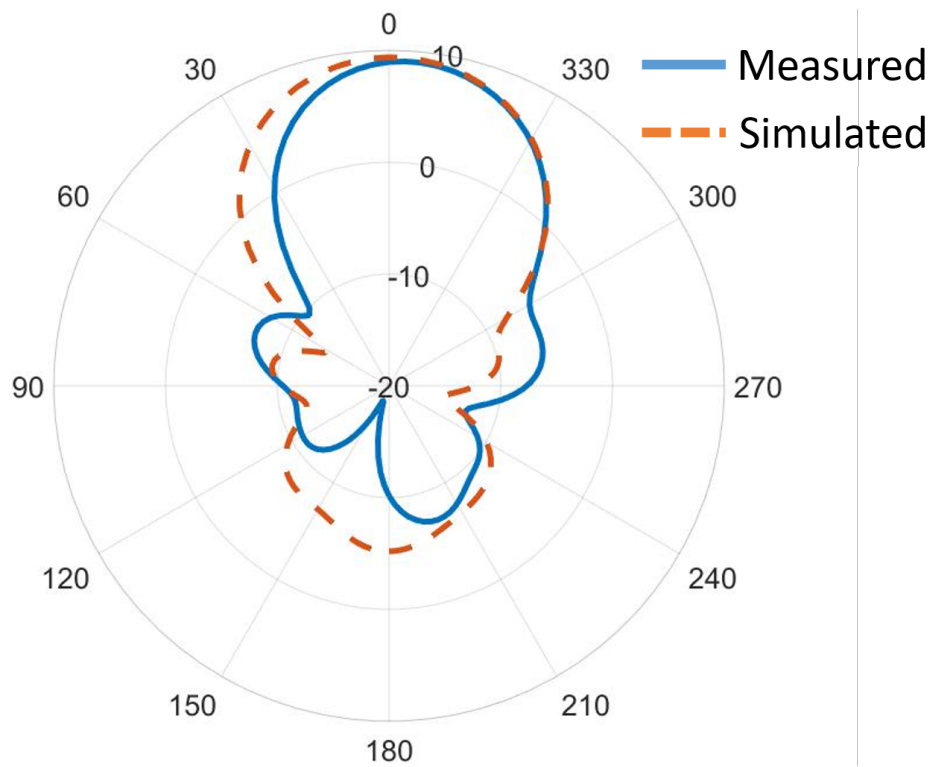


Figure A.4: Simulated and Measured gain of the patch antenna at 5.3 GHz with lens

## APPENDIX B

### MICROWAVE NETWORK ANALYSIS

When designing Microwave probes, the Helmholtz equation, Sommerfield radiation condition, and vector Green's theorem must be considered thoroughly to understand the radiation conditions of the designed probe. This section will serve as background for the derivation of the conditions that need to be solved when simulating and fabricating microwave probes. The vector Green's theorem is classified as

$$\oint_S \hat{n} \cdot (\vec{A} \times \nabla \times \vec{B} - \vec{B} \times \nabla \times \vec{A}) dS = \int_V (\vec{B} \cdot \nabla \times \nabla \times \vec{A} - \vec{A} \cdot \nabla \times \nabla \times \vec{B}) dV \quad (\text{B.1})$$

where  $\vec{A} = \vec{H}$  and  $\vec{B} = \vec{C}G = \vec{C} \frac{e^{-jkR}}{4\pi R}$  and as a notation from the notes let  $\vec{C}G = \vec{G}_1$  Green's function must satisfy the Helmholtz equation,

$$\nabla^2 G + k^2 G = 0 \quad (\text{B.2})$$

using Maxwell's equations

$$\nabla \times \vec{E} = -\vec{J}_m - j\omega\mu\vec{H} \quad (\text{B.3})$$

and

$$\nabla \times \vec{H} = \vec{J} + j\omega\epsilon\vec{E} \quad (\text{B.4})$$

To solve for terms used on the right hand side of the vector Green's theorem resulting in

$$\nabla \times \nabla \times \vec{H} = \nabla \times \vec{J} + j\omega\epsilon \nabla \times \vec{E} = \nabla \times \vec{J} - j\omega\epsilon \vec{J}_m + k^2 \vec{H} \quad (\text{B.5})$$

Solving for the other terms on the RHS of the vector Green's theorem,

$$\nabla \times \nabla \times \vec{G}_1 = \nabla(\nabla \cdot \vec{G}_1) + k^2 \vec{G}_1 \quad (\text{B.6})$$

Plugging these into the volume integral in the vector Green's theorem,

$$\begin{aligned} RHS &= \int_V [G\vec{C} \cdot (\nabla \times \vec{J} - j\omega\epsilon \vec{J}_m + k^2 \vec{H}) - \vec{H} \cdot (\nabla(\nabla \cdot \vec{G}_1) + k^2 \vec{G}_1)] dV \\ &= \int_V [G\vec{C} \cdot (\nabla \times \vec{J} - j\omega\epsilon \vec{J}_m) - \vec{H} \cdot \nabla(\nabla \cdot \vec{G}_1)] dV \end{aligned} \quad (\text{B.7})$$

where the terms

$$\nabla \cdot (\vec{H} \nabla \vec{G}_1) = (\nabla \cdot \vec{G}_1)(\nabla \cdot \vec{H}) + \vec{H} \cdot \nabla(\nabla \cdot \vec{G}_1) \quad (\text{B.8})$$

where

$$\nabla \cdot \vec{H} = \frac{\rho_m}{\mu}$$

and the term

$$\nabla \cdot \vec{G}_1 = \nabla \cdot (\vec{C}G) = G\nabla \vec{C} + \vec{C} \cdot \nabla G \quad (\text{B.9})$$

So

$$\vec{C}(\nabla^2 G + k^2 G = \nabla^2 \vec{C}G + k^2 \vec{C}G = 0) \quad (\text{B.10})$$

where  $\vec{C}$  is a constant vector meaning so the equation becomes

$$\nabla \cdot \vec{G}_1 = \nabla \cdot (\vec{C}G) = \vec{C} \cdot \nabla G \quad (\text{B.11})$$

plugging back into the earlier equation,

$$RHS = \int_V [G\vec{C} \cdot (\nabla \times \vec{J} - j\omega\epsilon\vec{J}_m) + \vec{C} \cdot \nabla G \frac{\rho_m}{\mu} - \nabla \cdot \vec{H}\vec{C} \cdot \nabla G] dV \quad (\text{B.12})$$

separating the positive and negative terms in the integral into their own respective integrals, and using the substitution of  $\int_V \nabla \cdot x dV = \oint x \cdot \hat{n} dS$  the RHS of the vector Green's theorem becomes

$$RHS = \int_V [G\vec{C} \cdot (\nabla \times \vec{J} - j\omega\epsilon\vec{J}_m) + \vec{C} \cdot \nabla G \frac{\rho_m}{\mu}] dV - \oint [(\vec{H}\vec{C} \cdot \nabla G) \cdot \hat{n}] dS \quad (\text{B.13})$$

and then moving the surface integral to the LHS of the Green's theorem to combine like terms, the LHS becomes now (after plugging in the variables defined earlier)

$$\oint_S \hat{n} \cdot (\vec{H} \times \nabla \times \vec{G}_1 - \vec{G}_1 \times \nabla \times \vec{H} + \vec{H}\vec{C} \cdot \nabla G) dS \quad (\text{B.14})$$

using B.5 and

$$\nabla \times \vec{G}_1 = \nabla \times \vec{C}G = G\nabla \times \vec{C} - \vec{C} \times \nabla G$$

where

$$G\nabla \times \vec{C} = 0$$

the LHS can be simplified to

$$\oint_S \hat{n} \cdot [\vec{H}\vec{C} \cdot \nabla G - (\vec{H} \times \vec{C} \times \nabla G) - \vec{C}G \times (\vec{J} + j\omega\epsilon\vec{E})]dS \quad (\text{B.15})$$

to simplify the LHS further by distributing the  $\hat{n}$  the following relations must be used

$$\hat{n} \cdot [\vec{H} \times \vec{C} \nabla G] = [\hat{n} \times \vec{H}] \cdot \vec{C} \times \nabla G = \vec{C} \cdot [\nabla G \times (\hat{n} \times \vec{H})]$$

and

$$\hat{n} \cdot [\vec{C} \times \vec{J} + j\omega\epsilon\vec{E}] = \vec{C} \cdot [\hat{n} \times (\vec{J} + j\omega\epsilon\vec{E})]$$

Pulling out  $\vec{C}$  so that the entire vector Green's theorem can be rewritten as

$$\begin{aligned} \vec{C} \cdot \oint_S (\hat{n} \times \vec{H}) \times \nabla G + \hat{n} \times \vec{J}G + j\omega\epsilon\hat{n} \times \vec{E}G + \nabla G \hat{n} \cdot hv]dS = \vec{C} \\ \cdot \int_V [G(\nabla \times \vec{J} - j\omega\epsilon\vec{J}_m) + \nabla G \frac{\rho_m}{\mu}]dV \end{aligned} \quad (\text{B.16})$$

Thus, the constant vector  $\vec{C}$  can be divided from both sides removing it from the equation entirely.

$$\oint_S [\nabla G \times (\hat{n} \times \vec{H}) + j\omega\epsilon\hat{n} \times \vec{H}G + \nabla G(\hat{n} \cdot \vec{H})]dS = \int_V [\vec{J} \times \nabla G - j\omega\epsilon\vec{J}_mG + \frac{\rho_m}{\mu}\nabla G]dV \quad (\text{B.17})$$

A surface can be characterized by  $S = S_0 \cup S_\epsilon + S_\infty$  on  $S_\epsilon$  where

$$G \cong \frac{1}{4\pi R}$$

and

$$\nabla G \cong -\frac{\hat{R}}{4\pi R^2}$$

Taking the limit of the surface integral in the function as  $\epsilon \rightarrow 0$  and plugging in the above functions,

where  $\hat{n} = \hat{R}$  in this case when applied using spherical coordinates,

$$\begin{aligned} \lim_{\epsilon \rightarrow 0} \oint_{S_\epsilon} [-(\hat{R} \times \vec{H}) \times \frac{\hat{R}}{4\pi\epsilon^2} + j\omega\epsilon\hat{R} \times \vec{E} \frac{1}{4\pi\epsilon} - (\hat{R} \cdot \vec{H}) \frac{\hat{R}}{4\pi\epsilon^2}] \epsilon^2 \sin\theta d\theta d\phi \\ = \lim_{\epsilon \rightarrow 0} \oint_{S_\epsilon} [(\hat{R} \cdot \vec{H}) \frac{\hat{R}}{4\pi} - \vec{H}(\hat{R} \cdot \hat{R}) \frac{1}{4\pi} - (\hat{R} \cdot \vec{H}) \frac{\hat{R}}{r\pi}] \sin\theta d\theta d\phi \\ = -\vec{H}(\vec{r}') \end{aligned} \quad (\text{B.18})$$

taking the limit on the surface as it goes towards  $\infty$ , the relations for  $G$  now become

$$G \cong \frac{e^{-jkr}}{4\pi r}$$

and

$$\nabla G \cong -jk\hat{r}\frac{e^{-jkr}}{4\pi r}$$

which can be applied as

$$\begin{aligned} & \lim_{r \rightarrow \infty} \oint_{S_\infty} [(\hat{n} \times \vec{H}) \times \nabla G + j\omega\epsilon\hat{n} \times \vec{E}G + (\hat{n} \cdot h\nu)\nabla G]dS \\ &= \lim_{r \rightarrow \infty} \oint_{S_\infty} [-jk(-\hat{r} \times \vec{H}) \times \hat{r}\frac{e^{-jkr}}{4\pi r} - j\omega\epsilon\hat{r} \times \vec{E}\frac{e^{-jkr}}{4\pi r} + jk\hat{r} \cdot \vec{H}\frac{e^{-jkr}}{r}]r^2 \sin\theta d\theta d\phi \quad (\text{B.19}) \\ &= \lim_{r \rightarrow \infty} \oint_{S_\infty} [-jk(\hat{r} \cdot \vec{H}) + jk(\hat{r} \cdot \hat{r})\vec{H} - j\omega\epsilon\hat{r} \times \vec{E} + jk\hat{r} \cdot \vec{E}]re^{-jkr} \sin\theta d\theta d\phi \\ &= 0 \end{aligned}$$

if  $r(jk\vec{H} - j\omega\epsilon\hat{r} \times \vec{E}) \rightarrow 0$  as  $r \rightarrow \infty$  which when restated becomes the Sommerfeld radiation while stating that  $r\vec{H}$  must be finite, and that  $\vec{H} = \frac{\hat{r} \times \vec{E}}{\eta}$  so, the answer can be written as

$$\vec{H}(\vec{r}') = \int_V [\vec{J} \times \nabla G + \frac{\rho_m}{\mu} \nabla G - j\omega\epsilon\vec{J}_m G]dV + \oint_{S_0} [(\hat{n} \times \vec{H}) \times \nabla G + (\hat{n} \cdot \vec{H})\nabla G + j\omega\epsilon(\hat{n} \times \vec{E})G]dS \quad (\text{B.20})$$

## B.1 Propagation

The propagation constant of a voltage wave on a transmission line can be described as:

$$\gamma = \sqrt{(R + j\omega L)(G + j\omega C)} = \alpha + j\beta \quad (\text{B.21})$$

Where  $\alpha$  and  $\beta$  can be defined in the following equations below:

$$\alpha = \omega\sqrt{LC}\sqrt{1 - rg}\sqrt{\frac{1}{2}[-1 + \sqrt{1 + (\frac{r+g}{1-rg})^2}]} \quad (\text{B.22})$$

$$\beta = \omega\sqrt{LC}\sqrt{1 - rg}\sqrt{\frac{1}{2}[+1 + \sqrt{1 + (\frac{r+g}{1-rg})^2}]} \quad (\text{B.23})$$

Where:

$$r = \frac{R}{\omega L}$$

$$g = \frac{G}{\omega C}$$

First, rearranging equations B.1 and B.1 to solve for R and G:

$$R = r\omega L$$

$$G = g\omega C$$

Replacing R and G within the original Eqn. B.21 to simplify the problem:

$$\gamma = \sqrt{(r\omega L + j\omega L)(g\omega C + j\omega C)}$$

$$\gamma = \omega\sqrt{LC}\sqrt{(r + j)(g + j)}$$

$$\gamma = \omega\sqrt{LC}\sqrt{(rg - 1) + j(r + g)}$$

After simplifying the propagation constant formula, it is possible to obtain two equations for the two unknowns,  $\alpha$  and  $\beta$ , by squaring both sides of the propagation constant formula then comparing the real and imaginary components.

$$\gamma = \omega\sqrt{LC}\sqrt{(rg - 1) + j(r + g)} = \alpha + j\beta$$

$$\gamma^2 = [\omega\sqrt{LC}\sqrt{(rg - 1) + j(r + g)}]^2 = [\alpha + j\beta]^2$$

$$\gamma^2 = \omega^2 LC[(rg - 1) + j(r + g)] = (\alpha^2 - \beta^2) + j(2\alpha\beta)$$

Therefore, the real and imaginary components can be compared as:

$$RE[\gamma^2] = \omega^2 LC(rg - 1) = \alpha^2 - \beta^2 \quad (\text{B.24})$$

$$IM[\gamma^2] = \omega^2 LC(r + g) = 2\alpha\beta \quad (\text{B.25})$$

From Eqn. B.25,  $\alpha$  can be solved with respect to  $\beta$ :

$$2\alpha\beta = \omega^2 LC(r + g)$$

$$\alpha = \omega^2 LC(r + g) \frac{1}{2\beta} \quad (\text{B.26})$$

This  $\alpha$  equation can be placed into the imaginary component equations from Eqn. B.24:

$$\alpha^2 - \beta^2 = \omega^2 LC(rg - 1)$$

$$\left(\omega^2 LC(r + g) \frac{1}{2\beta}\right)^2 - \beta^2 = \omega^2 LC(rg - 1)$$

$$(\omega^2 LC)^2 (r + g)^2 \frac{1}{4\beta^2} - \beta^2 = \omega^2 LC(rg - 1)$$

$\beta^2$  can be distributed across the equations:

$$(\omega^2 LC)^2 (r + g)^2 \frac{1}{4} - (\beta^2)^2 = \beta^2 \omega^2 LC(rg - 1)$$

Rearranging:

$$(\beta^2)^2 + \beta^2 \omega^2 LC(rg - 1) - (\omega^2 LC)^2 (r + g)^2 \frac{1}{4} = 0$$

The quadratic equation can be used:

$$x = \frac{-b \pm \sqrt{b^2 - 4ac}}{2a}$$

Where  $x = \beta^2$ ,  $a = 1$ ,  $b = \omega^2 LC(rg - 1)$ , and  
 $c = (\omega^2 LC)^2(r + g)^2 \frac{1}{4}$

$$\beta^2 = \frac{-\omega^2 LC(rg - 1) \pm \sqrt{[\omega^2 LC(rg - 1)]^2 - 4(\omega^2 LC)^2(r + g)^2 \frac{1}{4}}}{2} \quad (\text{B.27})$$

Simplifying:

$$\beta^2 = -\frac{1}{2}[\omega^2 LC(rg - 1) \pm \sqrt{(\omega^2 LC)^2(rg - 1)^2 + (\omega^2 LC)^2(r + g)^2}]$$

$$\beta^2 = -\frac{1}{2}[\omega^2 LC(rg - 1) \pm (\omega^2 LC)\sqrt{(rg - 1)^2 + (r + g)^2}]$$

$$\beta^2 = -\omega^2 LC \frac{1}{2}[(rg - 1) \pm \sqrt{(rg - 1)^2 + (r + g)^2}]$$

It is also helpful to pull out a  $(1 - rg)$ . Consider that in this case  $rg - 1 = -(1 - rg)$  and  $(rg - 1)^2 = (1 - rg)^2$ .

$$\beta^2 = -\omega^2 LC \frac{1}{2}[-(1 - rg) \pm \sqrt{(1 - rg)^2 + (r + g)^2}]$$

$$\beta^2 = -\omega^2 LC \frac{1}{2}[-(1 - rg) \pm (1 - rg)\sqrt{\frac{(1 - rg)^2 + (r + g)^2}{(1 - rg)^2}}] \quad (\text{B.28})$$

$$\beta^2 = \omega^2 LC(1 - rg) \frac{1}{2}[1 \mp \sqrt{1 + (\frac{r + g}{1 - rg})^2}]$$

From this point,  $\beta$  can be written as:

$$\beta = \sqrt{\omega^2 LC(1 - rg) \frac{1}{2}[1 \mp \sqrt{1 + (\frac{r + g}{1 - rg})^2}]}$$

$$\beta = \omega \sqrt{LC} \sqrt{1 - rg} \sqrt{\frac{1}{2}[1 \mp \sqrt{1 + (\frac{r + g}{1 - rg})^2}]}$$

This equation is similar to Eqn. B.23, but has a sign issue that needs to be resolved. The choice for this sign is dependent on the answer selected for  $\alpha$ .  $\alpha$  can be resolved in the same way  $\beta$  was resolved, starting with the imaginary equivalence equation from Eqn. B.25 to solve  $\beta$  with respect to  $\alpha$ :

$$2\alpha\beta = \omega^2 LC(r + g)$$

$$\beta = \omega^2 LC(r + g) \frac{1}{2\alpha}$$

From the real equivalence equation from Eqn. B.24:

$$\alpha^2 - \beta^2 = \omega^2 LC(rg - 1)$$

$$\alpha^2 - \left[ \omega^2 LC(r + g) \frac{1}{2\alpha} \right]^2 = \omega^2 LC(rg - 1)$$

$$(\alpha^2)^2 - \left[ \omega^2 LC(r + g) \right]^2 \frac{1}{4\alpha^2} = \omega^2 LC(rg - 1)$$

$$(\alpha^2)^2 - \omega^2 LC(rg - 1) - \left[ \omega^2 LC(r + g) \right]^2 \frac{1}{4\alpha^2} = 0$$

The quadratic equation can be used, where Where  $x = \alpha^2$ ,  $a = 1$ ,  $b = -\omega^2 LC(rg - 1)$ , and  $c = (\omega^2 LC)^2 (r + g)^2 \frac{1}{4}$

$$\alpha^2 = \frac{\omega^2 LC(rg - 1) \pm \sqrt{[\omega^2 LC(rg - 1)]^2 - 4[(\omega^2 LC)^2 (r + g)^2 \frac{1}{4}]}}{2}$$

From this point, it is recognizable that there is only one difference between the quadratic equations when solving for  $\alpha$  and  $\beta$ , from the above equation and Eqn. B.27. The only different is that the b component in the  $\alpha$  case is negative while it is possible in the  $\beta$  case. Skipping several

similar simplification steps explained while solving for  $\beta$ , similar to Eqn. B.28:

$$\alpha^2 = -\omega^2 LC \frac{1}{2} [(1 - rg) \pm (1 - rg) \sqrt{(1 + (\frac{r+g}{1-rg})^2)}]$$

$$\alpha^2 = -\omega^2 LC (1 - rg) \frac{1}{2} [1 \pm \sqrt{(1 + (\frac{r+g}{1-rg})^2)}]$$

Negating inside the parenthesis:

$$\alpha^2 = \omega^2 LC (1 - rg) \frac{1}{2} [-1 \mp \sqrt{(1 + (\frac{r+g}{1-rg})^2)}]$$

Solving for  $\alpha$ :

$$\alpha = \omega \sqrt{LC} \sqrt{1 - rg} \sqrt{\frac{1}{2} [-1 \mp \sqrt{(1 + (\frac{r+g}{1-rg})^2)}]}$$

Again, this is very close to the form provided in Eqn. B.22, but the minus plus symbol must be resolved. The final step will be to resolve the symbol by assuming that the plus is selected instead of the minus, and proving it by chugging the equations into Eqn. B.25. Therefore we assume the following:

$$\alpha = \omega \sqrt{LC} \sqrt{1 - rg} \sqrt{\frac{1}{2} [-1 + \sqrt{(1 + (\frac{r+g}{1-rg})^2)}]}$$

$$\beta = \omega \sqrt{LC} \sqrt{1 - rg} \sqrt{\frac{1}{2} [+1 + \sqrt{(1 + (\frac{r+g}{1-rg})^2)}]}$$

Place these into the imaginary equivalence equation:

$$\omega^2 LC (r + g) = 2\alpha\beta$$

$$\omega^2 LC (r + g) = 2\omega^2 LC (1 - rg) \sqrt{A} \sqrt{B}$$

Where  $A = \frac{1}{2} [-1 + \sqrt{(1 + (\frac{r+g}{1-rg})^2)}]$  and  $B = \frac{1}{2} [+1 + \sqrt{(1 + (\frac{r+g}{1-rg})^2)}]$ . Solving the product of the square roots of A and B:

$$\sqrt{A} \sqrt{B} = \sqrt{AB}$$

$$\sqrt{A}\sqrt{B} = \sqrt{\frac{1}{4}[-1 + \sqrt{(1 + (\frac{r+g}{1-rg})^2)}][+1 + \sqrt{1 + (\frac{r+g}{1-rg})^2}]}$$

Consider  $(X - 1)(X + 1) = X^2 - 1$ , where  $X = \sqrt{1 + (\frac{r+g}{1-rg})^2}$ . In other choices for plus or minus configurations, this will be different and, as proven soon, will be incorrect. Therefore:

$$\sqrt{A}\sqrt{B} = \sqrt{\frac{1}{4}\sqrt{[\sqrt{1 + (\frac{r+g}{1-rg})^2}]^2 - 1}}$$

$$\sqrt{A}\sqrt{B} = \sqrt{\frac{1}{4}\sqrt{1 + (\frac{r+g}{1-rg})^2 - 1}}$$

$$\sqrt{A}\sqrt{B} = \frac{1}{2}\sqrt{(\frac{r+g}{1-rg})^2}$$

$$\sqrt{A}\sqrt{B} = \frac{1}{2}(\frac{r+g}{1-rg})$$

Placing this equation back and solving both sides:

$$\omega^2 LC(r+g) = 2\omega^2 LC(1-rg)\sqrt{A}\sqrt{B}$$

$$\omega^2 LC(r+g) = 2\omega^2 LC(1-rg)\frac{1}{2}(\frac{r+g}{1-rg})$$

$$\omega^2 LC(r+g) = \omega^2 LC(r+g)$$

Therefore, the configurations of both  $\pm$  symbols in order to obtain the final solutions which are equivalent to equations B.22 and B.23 respectively:

$$\alpha = \omega\sqrt{LC}\sqrt{1-rg}\sqrt{\frac{1}{2}[-1 + \sqrt{(1 + (\frac{r+g}{1-rg})^2)}]}$$

$$\beta = \omega\sqrt{LC}\sqrt{1-rg}\sqrt{\frac{1}{2}[+1 + \sqrt{1 + (\frac{r+g}{1-rg})^2}]}$$

### B.1.1 Transmission Lines

Transmission lines are vital for simulating and analyzing the response of a microwave system due to the very important characteristics of attenuation and phase constant. The attenuation constant predicts how quickly the wave amplitude will dissipate within the system, while the phase constant predicts the change in phase per length along the path of the wave. The amplitude and phase are key in detection of location and composition of defects. For low loss lines, it can be assumed that  $r \ll 1$  and  $g \ll 1$ . That is, the following approximations must be true:

$$\alpha \approx \frac{1}{2} \left[ \frac{R}{\sqrt{L/C}} + G\sqrt{L/C} \right] \quad (\text{B.29})$$

$$\beta \approx \omega\sqrt{LC} \quad (\text{B.30})$$

### B.1.2 Solving for $\alpha$

$$\alpha = \omega\sqrt{LC}\sqrt{1 - rg} \sqrt{\frac{1}{2} \left[ -1 + \sqrt{1 + \left( \frac{r+g}{1-rg} \right)^2} \right]}$$

Consider that if  $r \ll 1$  and  $g \ll 1$ , then  $rg \ll 1$ . If  $rg \ll 1$ , then  $1 - rg \approx 1$ . Rewriting:

$$\alpha \approx \omega\sqrt{LC} \sqrt{\frac{1}{2} \left[ -1 + \sqrt{1 + (r+g)^2} \right]}$$

Consider when  $(r+g)^2 = r^2 + g^2 + rg$ . Because  $r \ll 1$  and  $g \ll 1$ , the effects of  $r^2$ ,  $g^2$ , and  $rg$  are amplified to be all very less than one. Therefore,  $(r+g)^2 \ll 1$ . Because of this, the approximation  $\sqrt{1 + \frac{X}{2}} \approx 1$  can be used, where  $X = (r+g)^2$ .

$$\alpha \approx \omega\sqrt{LC} \sqrt{\frac{1}{2} \left[ -1 + 1 + \frac{(r+g)^2}{2} \right]} \quad (\text{B.31})$$

$$\alpha \approx \omega\sqrt{LC} \sqrt{\frac{1}{4}(r+g)^2}$$

$$\alpha \approx \frac{1}{2} \omega\sqrt{LC}(r+g)$$

Substituting r and g from equations B.1 and B.1:

$$\alpha \approx \frac{1}{2}\omega\sqrt{LC}\left(\frac{R}{\omega L} + \frac{G}{\omega C}\right)$$

$$\alpha \approx \frac{1}{2}\sqrt{LC}\left(\frac{RC}{LC} + \frac{GL}{LC}\right)$$

$$\alpha \approx \frac{1}{2}\left(\frac{RC}{\sqrt{LC}} + \frac{GL}{\sqrt{LC}}\right)$$

$$\alpha \approx \frac{1}{2}\left(\frac{R}{\sqrt{LC}/(\sqrt{C})^2} + \frac{G(\sqrt{L})^2/\sqrt{L}}{\sqrt{C}}\right)$$

$$\alpha \approx \frac{1}{2}\left[\frac{R}{\sqrt{L/C}} + G\sqrt{L/C}\right]$$

This equation is the same as Eqn. B.29 and thus concludes the proof of the approximation.

### B.1.3 Solving for $\beta$

$$\beta = \omega\sqrt{LC}\sqrt{1 - rg}\sqrt{\frac{1}{2}\left[+1 + \sqrt{1 + \left(\frac{r + g}{1 - rg}\right)^2}\right]}$$

In a similar process to  $\alpha$ ,  $\beta$  can be simplified to Eqn. B.31:

$$\beta \approx \omega\sqrt{LC}\sqrt{\frac{1}{2}\left[+1 + 1 + \frac{(r + g)^2}{2}\right]}$$

$$\beta \approx \omega\sqrt{LC}\sqrt{1 + \frac{(r + g)^2}{4}}$$

$$\beta \approx \omega\sqrt{LC}\sqrt{\frac{4 + (r + g)^2}{4}}$$

As solved before,  $(r + g)^2 \ll 1$ . This means  $(r + g)^2 \ll 4$ , which is scaled four times more than the previous assumption. Therefore,  $4 + (r + g)^2 \approx 4$  is a reasonable assumption.

$$\beta \approx \omega\sqrt{LC}\sqrt{\frac{4}{4}}$$

$$\beta \approx \omega\sqrt{LC}$$

This is equivalent towards Eqn. B.30.

## B.2 Split Ring Resonator

The previous section's equations were utilized by ANSYS HFSS to simulate the response for a split ring resonator around 8 GHz, though the fabrication would have been difficult due to the small feature size of the split ring resonator. The simulated resonator, dimensions, and results are included below.

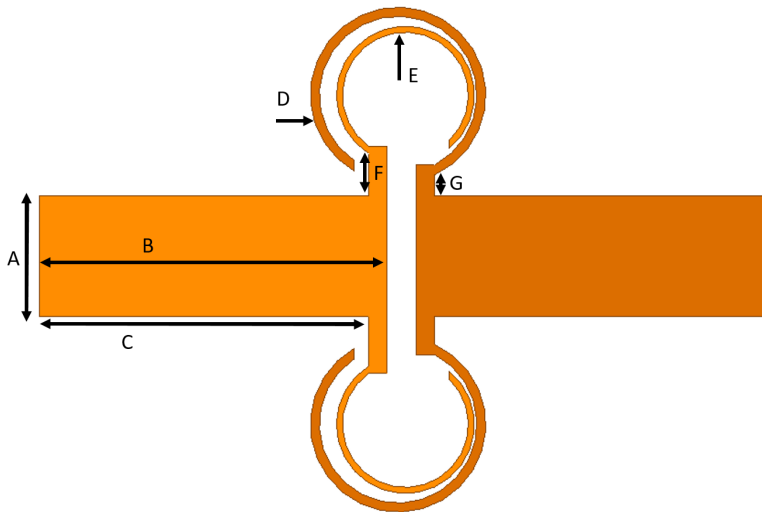


Figure B.1: Simulated split ring resonator with dimension parameters

Parameter	Dimension
A	3.3 mm
B	9.5 mm
C	9.15 mm
D	0.29 mm
E	0.22 mm
F	1.15 mm
G	0.57 mm
Minimum ring separation	0.07 mm
Maximum ring separation	0.4 mm

Table B.1: Split ring resonator dimension table

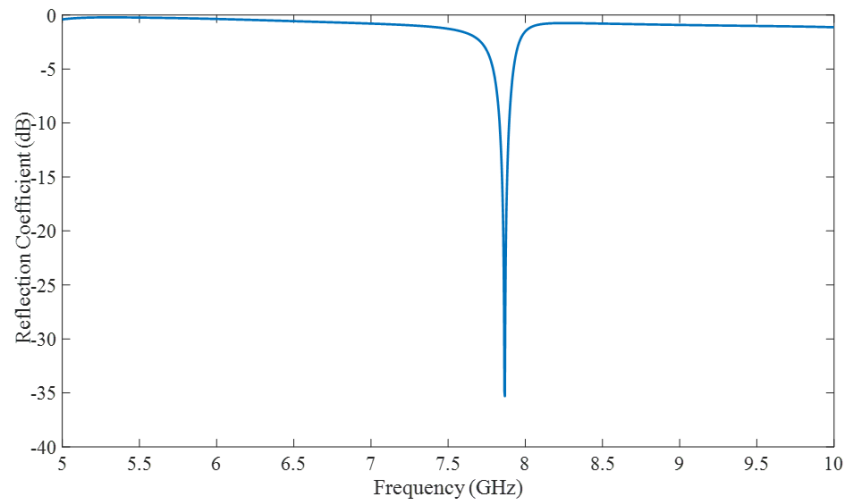


Figure B.2: Simulated split ring resonator response

## **BIBLIOGRAPHY**

## BIBLIOGRAPHY

- [1] V. T. Rathod, G. Raiu, L. Udpa, S. Udpa, and Y. Deng, “Embedded Thin Film Sensors Based Multi-Mode Guided Wave Filter,” *Proceedings of IEEE Sensors*, vol. 2018-October, pp. 0–3, 2018.
- [2] K. Gopalakrishnan, Y. Deng, and S. Chakrapani, “Studying the effect of primer coatings and surface activations on adhesion in adhesively bonded plastic plates using ultrasonic testing,” *Review of Progress in Quantitative Nondestructive Evaluation*, 2019.
- [3] D. Shoukroun, L. Massimi, M. Endrizzi, D. Bate, A. Olivo, and P. Fromme, “Composites impact damage detection and characterization using ultrasound and x-ray NDE techniques,” in *Health Monitoring of Structural and Biological Systems XIV* (P. Fromme and Z. Su, eds.), vol. 11381, pp. 27 – 33, International Society for Optics and Photonics, SPIE, 2020.
- [4] D. Berger, T. Will, H. C. Töpfer, G. Lanza, D. Koster, and H. G. Herrmann, “Characterisation and Optimization of in-process Eddy Current Sensor Arrays Using Computed Tomography,” *Procedia CIRP*, vol. 66, pp. 243–248, 2017.
- [5] R. Zoughi, “Microwave and millimeter wave nondestructive testing: A succinct introduction,” *Research in Nondestructive Evaluation*, vol. 7, no. 2-3, pp. 71–74, 1995.
- [6] G. G. Diamond and D. A. Hutchins, “A New Capacitive Imaging Technique for NDT,” *ECNDT 2006 - Poster 229*, pp. 1–8, 2006.
- [7] H. Heuer, M. Schulze, M. Pooch, S. Gäbler, A. Nocke, G. Bardl, C. Cherif, M. Klein, R. Kupke, R. Vetter, F. Lenz, M. Kliem, C. Bülow, J. Goyvaerts, T. Mayer, and S. Petrenz, “Review on quality assurance along the CFRP value chain - Non-destructive testing of fabrics, preforms and CFRP by HF radio wave techniques,” *Composites Part B: Engineering*, vol. 77, pp. 494–501, 2015.
- [8] M. Morozov, W. Jackson, and S. G. Pierce, “Capacitive imaging of impact damage in composite material,” *Composites Part B: Engineering*, vol. 113, pp. 65–71, 2017.
- [9] D. Kumar and Y. Deng, “An efficient multisensing system for shm of oil and gas pipelines,” *Review of Progress in Quantitative Nondestructive Evaluation*, 2019.
- [10] D. Kumar, S. Karuppuswami, Y. Deng, and P. Chahal, “A wireless shortwave near-field probe for monitoring structural integrity of dielectric composites and polymers,” *NDT and E International*, vol. 96, no. February, pp. 9–17, 2018.
- [11] R. Jacobs, M. Alzuhiri, M. Golkowski, and Y. Deng, “Low-power microwave induced thermoacoustic imaging: Experimental study and hybrid FEM Modeling,” *Progress In Electromagnetics Research C*, vol. 91, no. March, pp. 265–277, 2019.

- [12] S. Karuppuswami, M. I. Mohd Ghazali, S. Mondal, D. Kumar, A. Kaur, and P. Chahal, "A 3D printed UHF passive RFID tag for plastic components," *2019 IEEE International Symposium on Antennas and Propagation and USNC-URSI Radio Science Meeting, APSURSI 2019 - Proceedings*, pp. 597–598, 2019.
- [13] R. M. Narayanan, "Microwave Nondestructive Testing of Galvanic Corrosion and Impact Damage in Carbon Fiber Reinforced Polymer Composites," *International Journal of Microwaves Applications*, vol. 7, no. 1, pp. 1–15, 2018.
- [14] B. Salski, W. Gwarek, P. Kopyt, P. Theodorakeas, I. Hatzioannidis, M. Kouli, A. Y. Chong, S. M. Tan, V. Kappatos, C. Selcuk, and T. H. Gan, "Portable Automated Radio-Frequency Scanner for Non-destructive Testing of Carbon-Fibre-Reinforced Polymer Composites," *Journal of Nondestructive Evaluation*, vol. 35, no. 2, pp. 1–8, 2016.
- [15] Q. Wu, M. Li, Y. Gu, S. Wang, and Z. Zhang, "Imaging the interphase of carbon fiber composites using transmission electron microscopy: Preparations by focused ion beam, ion beam etching, and ultramicrotomy," *Chinese Journal of Aeronautics*, vol. 28, no. 5, pp. 1529–1538, 2015.
- [16] L. Ma and M. Soleimani, "Hidden defect identification in carbon fibre reinforced polymer plates using magnetic induction tomography," *Measurement Science and Technology*, vol. 25, no. 5, 2014.
- [17] D. Vavrik, J. Jakubek, I. Kumpova, and M. Pichotka, "Dual energy CT inspection of a carbon fibre reinforced plastic composite combined with metal components," *Case Studies in Nondestructive Testing and Evaluation*, vol. 6, pp. 47–55, 2016.
- [18] J. Dong, B. Kim, A. Locquet, P. McKeon, N. Declercq, and D. S. Citrin, "Nondestructive evaluation of forced delamination in glass fiber-reinforced composites by terahertz and ultrasonic waves," *Composites Part B: Engineering*, vol. 79, pp. 667–675, 2015.
- [19] C. Mattei and P. Marty, "Imaging of fatigue damage in cfrp composite laminates using nonlinear harmonic generation," *AIP Conference Proceedings*, vol. 657, no. 1, pp. 989–995, 2003.
- [20] O. Büyüköztürk and T. Y. Yu, "Far-field radar NDT technique for detecting GFRP debonding from concrete," *Construction and Building Materials*, vol. 23, no. 4, pp. 1678–1689, 2009.
- [21] S. Karuppuswami, S. Mondal, D. Kumar, and P. Chahal, "RFID Coupled Passive Digital Ammonia Sensor for Quality Control of Packaged Food," *IEEE Sensors Journal*, vol. 20, no. 9, pp. 4679–4687, 2020.
- [22] S. Mondal, K. P. Wijewardena, S. Karuppuswami, N. Kriti, D. Kumar, and P. Chahal, "Blockchain inspired RFID-based information architecture for food supply chain," *IEEE Internet of Things Journal*, vol. 6, no. 3, pp. 5803–5813, 2019.
- [23] S. Mondal, D. Kumar, S. Karuppuswami, M. I. Mohd Ghazali, A. Kaur, and P. Chahal, "A PSK modulation scheme for sensor integrated RFIDs," *2019 IEEE International Symposium*

*on Antennas and Propagation and USNC-URSI Radio Science Meeting, APSURSI 2019 - Proceedings*, pp. 635–636, 2019.

- [24] S. Mondal, D. Kumar, S. Karuppuswami, and P. Chahal, “A Harmonic RF Phase-Shifter Based Wireless pH Sensor,” *Proceedings - Electronic Components and Technology Conference*, vol. 2018-May, pp. 796–801, 2018.
- [25] S. S. Hubbard, J. E. Peterson, E. L. Majer, P. T. Zawislanski, K. H. Williams, J. Roberts, and F. Wobber, “Estimation of permeable pathways and water content using tomographic radar data,” *The Leading Edge*, vol. 16, pp. 1623–1628, 11 1997.
- [26] “Table of dielectric constants.” [http://www.ydic.co.jp/english/technology/table\\_E.html#Anchor\\_s](http://www.ydic.co.jp/english/technology/table_E.html#Anchor_s), 2007. Accessed: 2021-04-23.
- [27] S. A. Yoon, S. H. Cha, S. W. Jun, S. J. Park, J.-Y. Park, S. Lee, H. S. Kim, and Y. H. Ahn, “Identifying different types of microorganisms with terahertz spectroscopy,” *Biomedical Optics Express*, vol. 11, no. 1, p. 406, 2020.
- [28] S. Gupta and K. J. Loh, “A planar array capacitive imaging system for detecting damage in composite structures: a numerical study,” *Sensors and Smart Structures Technologies for Civil, Mechanical, and Aerospace Systems 2018*, vol. 10598, p. 105980H, 2018.
- [29] S. Kalinin and A. Gruverman, *Scanning Probe Microscopy Electrical and Electromechanical Phenomena at the Nanoscale*, vol. II. 2007.
- [30] J. Zhang, G. Y. Tian, and A. B. Zhao, “Passive RFID sensor systems for crack detection & characterization,” *NDT and E International*, vol. 86, no. December 2015, pp. 89–99, 2017.
- [31] H. G. Schantz, A. H. Unden, M. Nikravan, and D.-H. Kwon, “Simple formulas for near-field transmission gain and fields,” in *37th Antenna Applications Symposium, Allerton, IL*, 2013.
- [32] D. M. Pozar, *Microwave engineering*. John wiley & sons, 2011.
- [33] Z. Li, L. Zhou, H. Lei, and Y. Pei, “Microwave near-field and far-field imaging of composite plate with hat stiffeners,” *Composites Part B: Engineering*, vol. 161, no. May 2018, pp. 87–95, 2019.
- [34] A. Gokul, Srinivas, Radhika, and Dhanasekaran, “Inspection of Gfrp Composites by Microwave NDE,” *International Journal of Microwave Engineering*, vol. 5, no. 1, pp. 1–11, 2020.
- [35] S. Mukherjee, X. Shi, S. Datta, Y. Deng, S. Udpa, and L. Udpa, “Enhancement of microwave time reversal imaging using metallic reflectors,” *NDT and E International*, vol. 110, no. May 2019, p. 102192, 2020.
- [36] S. Mondal, D. Kumar, and P. Chahal, “A wireless passive ph sensor with clutter rejection scheme,” *IEEE Sensors Journal*, vol. 19, no. 9, pp. 3399–3407, 2019.

- [37] X. Shi, V. T. Rathod, S. Mukherjee, L. Udpa, and Y. Deng, "Multi-modality strain estimation using a rapid near-field microwave imaging system for dielectric materials," *Measurement: Journal of the International Measurement Confederation*, vol. 151, p. 107243, 2020.
- [38] Z. Li and Z. Meng, "A review of the radio frequency non-destructive testing for carbon-fibre composites," *Measurement Science Review*, vol. 16, no. 2, pp. 68–76, 2016.
- [39] M. Moosazadeh and S. Kharkovsky, "A compact high-gain and front-to-back ratio elliptically tapered antipodal vivaldi antenna with trapezoid-shaped dielectric lens," *IEEE Antennas and Wireless Propagation Letters*, vol. 15, pp. 552–555, 2016.
- [40] W. Che, B. Fu, P. Yao, and Y. L. Chow, "Substrate integrated waveguide horn antenna with dielectric lens," *Microwave and Optical Technology Letters*, vol. 49, no. 1, pp. 168–170, 2007.
- [41] H. Zhuang, F. Kong, K. Li, J. Zhao, and S. Sheng, "Analysis of graphene-based half maxwell fish-eye lens using effective index method," *Optical Engineering*, vol. 53, p. 127109, 12 2014.
- [42] Z. N. Chen, D. Liu, H. Nakano, X. Qing, and T. Zwick, *Handbook of antenna technologies*, vol. 1-4. 2016.
- [43] H.-X. Xu, G.-M. Wang, Z. Tao, and T. Cai, "An octave-bandwidth half maxwell fish-eye lens antenna using three-dimensional gradient-index fractal metamaterials," *IEEE Transactions on Antennas and Propagation*, vol. 62, no. 9, pp. 4823–4828, 2014.
- [44] O. Quevedo-Teruel, J. Miao, M. Mattsson, A. Algaba-Brazalez, M. Johansson, and L. Manholm, "Glide-symmetric fully metallic luneburg lens for 5g communications at ka-band," *IEEE Antennas and Wireless Propagation Letters*, vol. 17, no. 9, pp. 1588–1592, 2018.